UPC - Universitat Politècnica de Catalunya

Doctoral Thesis

QUANTUM FREQUENCY CONVERSION FOR HYBRID QUANTUM NETWORKS

Author:
Nicolas MARING

Supervisor:
Prof. Dr. Hugues DE RIEDMATTEN

*A thesis submitted in fulfilment of the requirements
for the degree of Doctor of Philosophy*

in the

QPSA - Quantum Photonics with Solids and Atoms *group,*
ICFO - The Institute of Photonic Sciences

July 2018

UNIVERSITAT POLITÈCNICA DE CATALUNYA
BARCELONATECH

ICFO
Institut de Ciències Fotòniques

Abstract

The ability to control the optical frequency of quantum state carriers (i.e. photons) is an important functionality for future quantum networks. It allows all matter quantum systems - nodes of the network - to be compatible with the telecommunication C-band, therefore enabling long distance fiber quantum communication between them. It also allows dissimilar nodes to be connected with each other, thus resulting in heterogeneous networks that can take advantage of the different capabilities offered by the diversity of its constituents. Quantum memories are one of the building blocks of a quantum network, enabling the storage of quantum states of light and the entanglement distribution over long distances. In our group, two different types of memories are investigated: a cold atomic ensemble and an ion-doped crystal. In this thesis I investigate the quantum frequency conversion of narrow-band photons, emitted or absorbed by optical quantum memories, with two different objectives: the first one is to connect quantum memories emitting or absorbing visible single photons with the telecommunication wavelengths, where fiber transmission loss is minimum. The second and main goal is to study the compatibility between disparate quantum nodes, emitting or absorbing photons at different wavelengths. More precisely the objective is to achieve a quantum connection between the two optical memories studied using quantum frequency conversion techniques.

The main core of this work is the quantum frequency conversion interface that bridges the gap between the cold ensemble of Rubidium atoms, emitting photons at $780\,\mathrm{nm}$, and the Praseodymium ion doped crystal, absorbing photons at $606\,\mathrm{nm}$. This interface is composed of two different frequency conversion devices, where a cascaded conversions takes place: the first one converts $780\,\mathrm{nm}$ photons to the telecommunication C-band, and the second one converts them back to visible, at $606\,\mathrm{nm}$. This comes with several challenges such as conversion efficiency, phase stability and parasitic noise reduction, which are important considerations to show the conservation of quantum behaviors through the conversion process.

This work can be divided in three parts. In a first one, we built a quantum frequency conversion interface between 606 nm and the C-band wavelength, capable of both up and down-conversion of single photon level light. We also characterized the noise processes involved in this specific conversion. In the down-conversion case we showed that memory compatible heralded single photons emitted from a photon pair source preserve their non-classical properties through the conversion process. In the up-conversion case, we showed the storage of converted telecom photons in the praseodymium doped crystal, and their retrieval with high signal to noise ratio.

The second part of the work was devoted to the conversion of photons from an emissive Rubidium atomic quantum memory to the telecom C band. In this work we converted the heralding photons from the atomic ensemble and measured non-classical correlations between a stored excitation and a C-band photon, necessary for quantum repeater applications.

In the last part of the thesis, we setup the full frequency conversion interface and showed that heralded photons emitted by the atomic ensemble are converted, stored in the solid state memory and retrieved with high signal to noise ratio. We demonstrated that a single collective excitation stored in the atomic ensemble is transfered to the crystal by mean of a single photon at telecom wavelength. We also showed time-bin qubit transfer between the two quantum memories. This work represents the first proof of principle of a photonic quantum connection between disparate quantum memory nodes.

The results presented in this thesis pave the way towards the realization of modular and hybrid quantum networks.

Resum

La capacitat de controlar la freqüència òptica dels portadors d'estats quàntics (és a dir, els fotons) és una funcionalitat important per a les futures xarxes quàntiques. Permet que tots els sistemes quàntics de matèria (nodes de la xarxa) siguin compatibles amb la banda C de telecomunicacions, permetent així la comunicació quàntica de llarga distancia amb fibres entre ells. També permet connectar nodes diferents, de manera que es generen xarxes heterogènies que poden aprofitar les diferents capacitats que ofereix la diversitat dels seus components. Les memòries quàntiques són un dels blocs bàsics d'una xarxa quàntica, que permeten l'emmagatzematge dels estats quàntics de llum i la distribució d'entrellaçament a llargues distàncies. En el nostre grup, s'investiguen dos tipus de memòries diferents: un conjunt d'àtoms freds i un cristall dopat amb ions. En aquesta tesi investigo la conversió de freqüències quàntiques de fotons amb ample de banda estret emesos o absorbits per memòries quàntiques òptiques amb dos objectius diferents: el primer és connectar memòries quàntiques que emeten o absorbeixen fotons individuals visibles amb longituds d'ona de telecomunicacions, on les pèrdues en fibra són mínimes. El segon objectiu principal és estudiar la compatibilitat entre nodes quàntics diferents, emetent o absorbint fotons a diferents longituds d'ona. Més precisament, l'objectiu és aconseguir una connexió quàntica entre les dues memòries òptiques estudiades mitjançant tècniques de conversió quàntica de freqüències.

La part principal d'aquest treball és el desenvolupament de la interfície de conversió quàntica de freqüències que fa de pont entre el núvol d'àtoms freds de Rubidi, emetent fotons a 780 nm, i el cristall dopat amb ions de Praseodimi, que absorbeix els fotons a 606 nm . Aquesta interfície es compon de dos dispositius diferents de conversió de freqüència, on es produeixen conversions en cascada: el primer converteix fotons de 780 nm a la banda C de telecomunicacions, i el segon els converteix a 606 nm. Això comporta diversos desafiaments com ara l'eficiència de la conversió,

l'estabilitat de la fase i la reducció del soroll paràsit, que són consideracions importants per mostrar la conservació dels comportaments quàntics a través del procés de conversió.

Aquest treball es pot dividir en tres parts. En una primera, hem construït una interfície de conversió quàntica de freqüències entre 606 nm i la longitud d'ona de la banda C, capaç tant de conversió cap amunt i avall de la llum al nivell de fotó individual. També hem caracteritzat els processos de soroll implicats en aquesta conversió específica. En el cas de conversió cap avall, vam mostrar que fotons individuals anunciats compatibles amb les memòries quàntiques i emès a partir d'una font de parells de fotons preserven les seves propietats no clàssiques durant el procés de conversió. En el cas de conversió cap amunt, vam mostrar l'emmagatzematge de fotons de telecomunicacions convertits en el cristall dopat de praseodimi i la seva recuperació amb una alta relació senyal / soroll.

La segona part del treball es va dedicar a la conversió de fotons a partir d'una memòria quàntica atòmica de Rubidium emissiva a la banda de telecomunicacions C. En aquest treball es van convertir els fotons anunciats del núvol atòmic i es van mesurar correlacions no clàssiques entre una excitació emmagatzemada i un fotó de banda C, necessàries per a les aplicacions de repetidor quàntic.

En l'última part de la tesi, vam configurar la interfície de conversió de freqüència completa i vam mostrar que els fotons anunciats emesos pel conjunt atòmic es converteixen, s'emmagatzemen en la memòria d'estat sòlid i es recuperen amb una alta relació senyal / soroll. Hem demostrat que una sola excitació col·lectiva emmagatzemada al conjunt atòmic es transfereix al cristall mitjançant un fotó individual a la longitud d'ona de telecomunicacions. També vam mostrar la transferència de qubit codificat en temps entre les dues memòries quàntiques. Aquest treball representa la primera prova de principi d'una connexió quàntica fotònica entre nodes de memòria quàntica diferents. Els resultats presentats en aquesta tesi obren el camí cap a la realització de xarxes quàntiques modulars i híbrides.

Acknowledgements

First of all, I would like to thank my thesis advisor, Hugues de Riedmatten, for giving me the chance to be part of his group and research project. In particular I appreciated your guidance and availability throughout the thesis.

I thank the lively QPSA group and all its members from the past and the present. I would like to especially thank Margherita who was here since the beginning, for her professional support and her friendship. I thank Georg with whom I spent the greatest, hardest and most exciting moments in the lab. I thank my fiber companions Pau, Kutlu and Dario, without whom this thesis would obviously not be the same. It was easy to connect with you guys but also fun moments inside and outside the lab. Dr. Kutlu, you should never forget the 3 most important things in life. I will for sure not forget Matteo, Patrick, Boris the quantum shaman, Must-ache, Ema, Ale el poeta, Auxi, Bernardo and Chetan. Akheysh.

I also thank Thierry Chanelière for his introduction to the world of quantum memories and for his helpful advices.

I have also been lucky to meet many people in the last 5 years.
I thank Gabi, for her full support, her incredible patience and kindness. I thank Antoine, Kevin and Simon for the awesome times outside ICFO, mainly involving sports, beers and flashing lights. I also thank Achim, Eric, Mathieu, James, Jianbo, Fra, Fabien and Carlotta, and the Barcelona friends Alex, Barbara, Kiki and Thomas.

Ces dernières années n'auraient sûrement pas été si faciles sans mes soutiens de toujours. Je remercie grandement mes parents et grands-parents pour leur amour et l'éducation reçue. Merci à ma petite soeur Natacha, mes tantes, mon oncle et mes cousins pour leur soutien, les visites et les raclettes.

List of publications

1. Nicolas Maring, Dario Lago-Rivera, Andreas Lenhard, Georg Heinze and Hugues de Riedmatten, *Quantum frequency conversion of memory compatible single photons from 606 nm to the telecom C-band*, Optica, **5**,(5) 507-513 (2018) (Chapter 3).

2. Nicolas Maring, Kutlu Kutluer, Joachim Cohen, Matteo Cristiani, Margherita Mazzera, Patrick M Ledingham and Hugues de Riedmatten, *Storage of up-converted telecom photons in a doped crystal*, New J. Phys. **16**, 113021 (2014) (Chapter 3).

3. Pau Farrera*, Nicolas Maring*, Boris Albrecht, Georg Heinze and Hugues de Riedmatten,(*co-first authors) *Non-classical correlations between a C-band telecom photon and a stored spin-wave*, Optica, **3**,(9) 1019-1024 (2016) (Chapter 4).

4. Nicolas Maring, Pau Farrera, Kutlu Kutluer, Georg Heinze, Margherita Mazzera and Hugues de Riedmatten, *Photonic quantum state transfer between a cold atomic gas and a crystal*, Nature **551,** 485-488 (2017) (Chapter 5).

Table of Contents

Chapter 1

Introduction

Efficient communication between distant places has always been a challenge and a strategic technology. Different solutions to the problem have been found throughout the history. In the late 18th century, Claude Chappe (1763-1805) developed a novel optical semaphore system, permitting to convey information by means of visual signals between two towers separated by 10 to 20 km. On top of each tower, the system had two arms connected by a cross-arm (Fig. 1.1(a)). Each arm had seven positions, and the cross-arm had four more permitting a 196-combination code. This encoding technique appeared to be much faster and more efficient than the traditional post riders in the long distance. In 1794, a first test between the cities of Paris and Lille, separated by 193 km, was successful. A single "bit" of information could travel along the 15 relay towers with an equivalent speed of 1200 km/h. The system was then developed across Europe to become the first functional data network (Fig. 1.1(b)) and was extensively used for political and military purposes. In 1845 the first electric telegraph line was created and the optical semaphore was rapidly abandoned.

The modern Internet was developed in the late 20th century, together with fast and efficient computers. This on-going revolution deeply impacts our society, reshaping the way we consume, communicate and socialize. It also
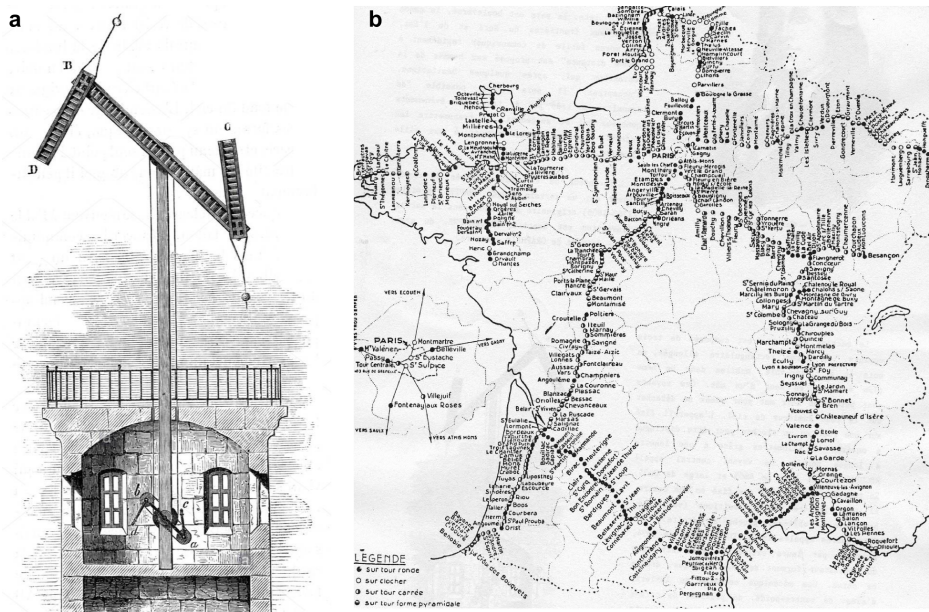
FIGURE 1.1: Chappe's Semaphore system. (a) Relay tower with mechanical arms. (b) 1844 map of France, with 534 towers covering a distance of 5000 km.

gives access to close to infinite knowledge, although to a limited number of people. The binary encoding of information on bits of 0s and 1s, processed with fast electronics and transmitted thanks to multiplexed photonic capabilities and optical fibers, led to the massive and efficient network of today. This classical data network will not likely be replaced anytime soon but shows some weaknesses though, mainly concerning the security of information and some computation limitations. This is where Quantum Information Science (QSI) comes into play. With the study of quantum mechanical effects, researchers realized that encoding information on quantum states of particles (quantum bits) can be technologically useful, giving powerful capabilities and advantages for secure communication [1], computing [2] and complex simulation [3]. The idea of a quantum internet [4] emerged and could eventually extend the capabilities of nowadays telecommunication network in which quantum communications [5] or distributed quantum computing [6] could be implemented. Quantum networks also have applications in sensing and metrology [7].

In this chapter, I will first explain the basic concepts of quantum information science. After an introduction on quantum communication and quantum networks, I will describe how a long distance quantum communication link could be implemented, using the quantum repeater concept. This leads to the need of quantum memories for light compatible with the telecommunication wavelengths. Two quantum memory protocols, used during the PhD, will then be described in more details. I will also discuss the compatibility between fundamentally different quantum systems together, paving the way towards hybrid quantum networks. Finally I will introduce the concept of quantum frequency conversion, permitting the frequency manipulation of quantum states of light.

1.1 Quantum information science

1.1.1 Qubits

Unlike classical bits that are either 0s or 1s, quantum bits (qubits) [8] are encoded on the state of a quantum system. In quantum mechanics a quantum system can be in a superposition of orthogonal states. Using the the Dirac notation a qubit can be expressed as:

$$|\psi\rangle = \alpha|0\rangle + \beta|1\rangle, \tag{1.1}$$

where α and β are the complex probability amplitude such that $|\alpha|^2 + |\beta|^2 = 1$, and $|0\rangle$ and $|1\rangle$ are two orthogonal basis states.

An easy way to visualize such state is using the Bloch sphere representation (Fig. 1.2):

$$|\psi\rangle = \cos\left(\frac{\theta}{2}\right)|0\rangle + e^{i\phi}\sin\left(\frac{\theta}{2}\right)|1\rangle, \tag{1.2}$$

where θ and ϕ are azimuthal and longitudinal angles. The state of the qubit is then represented on the surface of the sphere. Once measured the wave function of the qubit collapses on one of the two orthogonal basis set by the
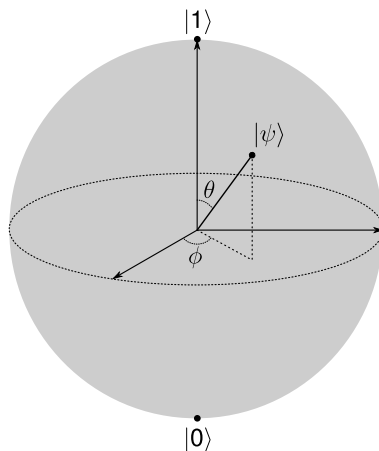
FIGURE 1.2: Bloch sphere representation.

measurement with probability α and β. Qubits are particularly sensitive to external perturbations that could destroy the quantum superposition.

A qubit can be *stationary*, meaning that it is based on a matter system such as single ions, single atoms, cold or hot atomic gases, color centers in diamonds, quantum dots, Josephson junctions or ion doped crystals. Depending on the system used, a qubit can be encoded on different degrees of freedom of the considered particle such as nuclear spins, electronic spins or circulation flux. Another kind of qubit called *flying* qubit, refers to qubits that can travel long distances. They are usually encoded on photons (even though cold atomic experiments sometimes fly on a plane [9]). The most used photonic qubit is the polarization of light using for instance horizontal and vertical orthogonal bases. Other degrees of freedoms like photon number (Fock states) or time of arrival (time-bin) can also be used.

Time-bin qubit

Polarization qubits are probably the most practical in term of generation and analysis but for long distance fiber-transmission, it is prone to decoherence caused by polarization fluctuation or polarization mode dispersion. Time-bin qubits [10], based on the time of arrival of a photon, are

more suitable for long distance communication. A relatively easy way of generating such a state is to send a single photon through an unbalanced Mach-Zehnder interferometer with a path length difference longer than the coherence length of the photon (Fig. 1.3), in which the phase φ between the short and long arm of the interferometer can be controlled. At the output, the photon is in a superposition state of having traveled in the short arm (*early* time-bin) and the long arm (*late* time-bin). The state can be then written as

$$|\psi\rangle = \alpha_{\mathrm{e}}|\text{early}\rangle + \alpha_{\mathrm{l}}\mathrm{e}^{i\varphi}|\text{late}\rangle, \tag{1.3}$$

where α_{e} and α_{e} are the probability amplitudes.

The analysis of the state can be performed using a second interferometer with the same path difference (Fig. 1.3). At the output 3 modes can be observed. The central one corresponds to the interference between the *early* and *late* time-bin of interest. The basis of measurement of this qubit can be set by rotating the phase difference β of the analysis interferometer. Interference fringes can then be measured, rotating either φ or β where the intensity of the interference is $\propto 1 \pm V\cos(\varphi - \beta)$. High visibilities V can be challenging to obtain, mainly when the time difference between the bins is long. Stable interferometers or phases involved in the preparation, the analysis or along the channel are needed.
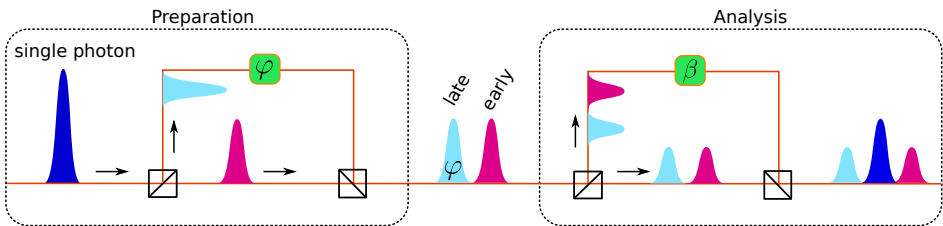
FIGURE 1.3: Time bin qubit preparation and analysis.

Since its introduction [10, 11], time-bin encoding was used in several QSI experiments such as long distance quantum teleportation [12–14], long distance distribution of qubits [15], high dimensional entanglement between

two photonic systems [16, 17], storage of time-bin photons in a quantum memory [18, 19], time-bin entangled photons from a quantum dot [20] and recently entanglement between a photonic time-bin qubit and a spin excitation in an atomic ensemble [21].

1.1.2 Entanglement

Entanglement is a key concept in quantum mechanics, which led to strong philosophical debates and new technological promises in quantum information science.

Two or more particles are said *entangled* when they cannot be described individually but only as a whole. The joint quantum state of two or more *entangled* particles cannot be factorized. For instance two entangled particles A and B can be described mathematically as

$$|\Psi_{A,B}^{\pm}\rangle = \frac{1}{\sqrt{2}} \left(|0_A, 1_B\rangle \pm |1_A, 0_B\rangle \right). \tag{1.4}$$

The striking effect is that when one particle is measured, the state of its twin particle collapses. This means that the measurement on the state of one particle has an effect of the state of the other. The non-intuitive fact is that this happens instantaneously, no matter the distance between the two particles, which contradicts the laws of local realism. This led to multiple debates in the scientific community, highlighted by the EPR (Einstein, Podolsky and Rosen) paper in 1935 [22], which suggested that quantum mechanics is not a complete theory. In 1964 John Bell proposed an inequality [23], know as the *Bell inequality* and testable experimentally. If violated, it proves that hidden variables [24] that could solve the EPR paradox do not exist and thus shows that the correlations between distant entangled particles do not obey local realism. The first experimental demonstration violating the Bell inequality was done in 1972 [25]. Since then, many experiments have been performed with various systems, including photons [26, 27], ions [28], atoms [29, 30] and hybrid light-matter

systems [31, 31–34]. Finally in 2015, the first loophole-free Bell test experiment was reported [35], measuring the entanglement between NV centers separated by 1.3 km. Shortly after, other experiments [36–38] also demonstrated loophole free Bell tests.

1.2 Quantum network and quantum communication

A quantum network is a general concept that has implications in quantum communication, distributed quantum computing [6] and metrology [7]. The idea is to have quantum nodes connected with each others via quantum channels [4]. Quantum nodes are matter systems, able to generate, store and process quantum information. In between, they exchange flying qubits (i.e. photons) that carry the information along quantum channels. Depending on the application and on the types of quantum nodes, a quantum network can have different architectures. Ideally the quantum nodes have moderate processing capabilities and are able to store and distribute entanglement across the network.
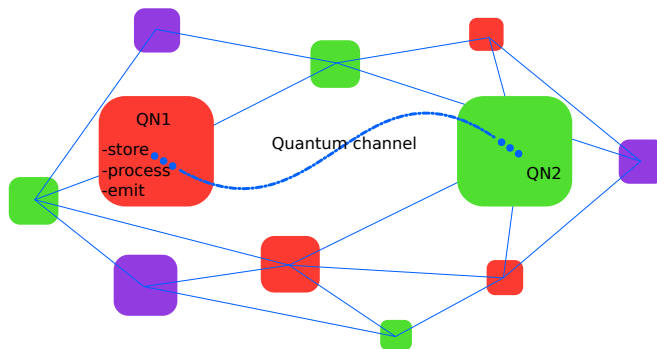
FIGURE 1.4: Quantum network.

Quantum communication is the ability to distribute information coded on quantum states of particles to distant places, e.g. for secure communication purposes [39]. One way of securing information is to use quantum key distribution (QKD). The first proposed implementation is the *BB84*, by

Charles Bennett and Gilles Brassard [40], and is today available commercially. The idea is to share a secrete key transmitted with single photons between two parties. Another protocol, the *E91* [41], makes use of entanglement between two nodes. For long distance communication two types of network are generally considered: one is fibered and uses existing telecom cables, and the other uses free space transmission with for instance satellite based-communications. In a recent work, a satellite-based entanglement distribution of entangled photon pairs to two locations separated by 1203 kilometers on Earth has been reported [42]. Another remarkable free-space communication is the demonstration of entanglement based teleportation between two islands separated by 144 km. For fiber transmission, demonstrations of quantum entanglement or teleportation never reached more than few hundreds of kilometers [14, 43, 44].

The main issue with direct transmission in fiber is the loss of signal over very long distances. Unlike the classical network in which the signal is amplified along the way, quantum information cannot be copied with 100 % fidelity (no-cloning theorem) [45]. Considering a single photon source at the telecom wavelength for which transmission losses are the lowest in fiber (0.2 dB/km), only 1 % is transmitted after 100 km, 0.000000000000000001 % after 1000 km. At such distances, direct quantum communication in optical fibers is impossible. To extend quantum communications to longer distances quantum repeaters have been proposed.

1.2.1 Quantum repeater

In order to overcome transmission losses and decoherence over long distances, the quantum repeater was proposed in 1998 [46].

The idea is to divide a long distance channel of length L by several segments of shorter lengths. Each segment is composed of two quantum nodes that can share entanglement together. Once two neighboring segments are simultaneously entangled, an operation called *entanglement swapping* is
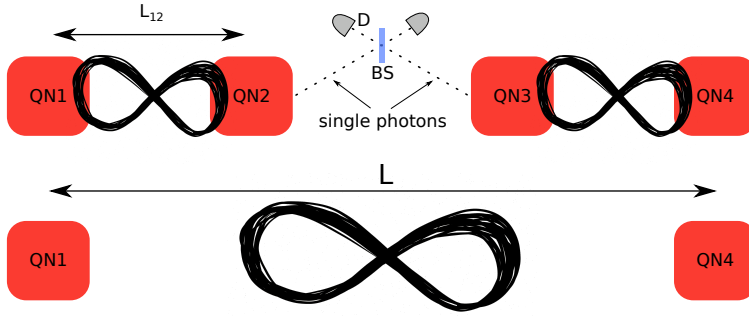
FIGURE 1.5: Entanglement swapping operation.

performed (Fig. 1.5). If successful, it extends the entanglement to the two outer nodes, although they have never interacted. The entanglement swapping [47] is a joint measurement (Bell state measurement) between two entangled states, which is actually a special case of quantum teleportation [40], and permits the distribution of entanglement in a heralded fashion. Repeating the operation many times, the length of the channel can considerably be extended. The issue is that entanglement generation within an elementary link is not a deterministic process, and the probability that N nodes are entangled with their neighbors at the same time decreases exponentially with the number of segments. The idea of a quantum repeater is to use quantum memories as nodes to store the entanglement while waiting that a neighboring node is ready for the entanglement swapping. Therefore, in such an architecture, a quantum node must be able to share entanglement with its neighbor, to store it and to emit it via single photons. Moreover in a fibered channel the single photons must be at the telecom wavelength to reduce the transmission losses. The compatibility of quantum memories with the telecom wavelength will be discussed in the next section.

Different architectures have been proposed for the quantum repeater [48]. The first one in 2001 is the DLCZ (named after Duan Lukin Cirac and Zoller) protocol [49]. It uses single collective spin excitations in atomic

ensembles, that are heralded by the emission and detection of single photons (detailed in the next section). Noticeable different architectures later proposed combine multimode absorptive quantum memories with photon pair sources [50] or single photons sources [51].

Note that new generations of quantum repeaters based on error correction have been proposed [52, 53] and do not require quantum memories and entanglement creation.

1.2.2 Quantum memories

An optical quantum memory is a device capable of storing a quantum state carried by light and of retrieving it on demand with high fidelity. A flying qubit (ie photon) should interact strongly with the matter system, and be transfered to an internal degree of freedom of the quantum memory.

Quantum memories are not only useful for quantum repeater applications. They also have interest in different quantum technologies such as deterministic single photon emissions [54, 55], linear optics quantum computing [56] or single photon detection [57]. They can be implemented in many systems such as single ions or atoms, vacancy centers in diamonds, warm or cold atomic ensembles and rare-earth ion doped crystals.

We can distinguish between two different types of quantum memories [58]. Some are emissive systems, equivalent to a photon pair source with embedded on-demand delay between the two photons. Other memories are absorptive and must re-emit the photon on-demand.

Several figures of merit of a quantum memory are to be considered. The storage and retrieval efficiency is an important characteristic. For quantum repeater applications, an efficiency above $90\,\%$ is often required [48]. Coherent light storage has been observed at this regime [59]. A second figure of merit is the storage fidelity, which estimates how the retrieved qubit is faithful to the stored one. It can be measured via quantum state

tomography [60]. In order to show the quantum character of a storage device, the classical limit of $F = \frac{N+1}{N+2}$ [61] is often used, as a value to surpass for the storage of a N-particle Fock the state. However higher fidelities are required for quantum repeater applications [48]. Another important characteristic of a quantum memory is the storage time as it limits the possible length of the entanglement distribution. Up to now the longest storage time observed is in the order of the minute [62] with classical light pulses, and 220 ms in the quantum regime [63]. Another requirement is the multimodal (in term of time, frequency and even space) capacity of the memory that can increase its performance[50].

One last important requirement discussed previously is the compatibility of a quantum memory with telecom light when considering fiber transmission. Three solutions are generally considered. The first one is to use a storage device that absorbs and emits light at the telecommunication wavelength. Currently the only promising system is Erbium ions for which quantum storage has been demonstrated, using Erbium-doped fiber [64]. Unfortunately it often suffers from very low storage efficiencies. A second solution is to use non-degenerate photon pair sources: one photon is resonant with the memory and is stored while the other one, at telecom wavelength, can travel long distances in fiber [50]. This approach has been shown in several experiments [65, 66]. A third solution is the use of quantum frequency conversion techniques [67] in order to shift the frequency of the quantum state carrier when needed. This will be the subject of this thesis.

Several protocols exist for light storage [58, 68, 69], however I will only describe two which I used during the PhD: the Atomic Frequency Comb (AFC) protocol, mainly used as an absorptive memory and the DLCZ protocol, used as an emissive memory. The two protocols are based on single collective excitations in atoms or ions ensembles.

1.2.2.1 AFC

The AFC protocol, proposed in Ref. [70], is well suited for inhomogeneously broadened and spectral holeburning media. When an incoming photon is collectively absorbed by such medium, an atomic coherence is created and is delocalized over N ions. This single collective excitation dephases due to the inhomogeneity as

$$|\Psi\rangle = \sum_{j=1}^{N} e^{i\delta_j t} e^{-i\boldsymbol{k}.\boldsymbol{r}_j} |g_1 \cdots e_j \cdots g_N\rangle, \qquad (1.5)$$

where δ_j is the detuning of the jth ion, and r_j its position. However, if the absorption line is tailored into a periodic structure (Fig. 1.6) with a well defined frequency spacing of Δ (referred to as a comb), we can assume that $\delta_j = m_j \Delta$. The atomic excitation will therefore rephase at a time $\tau_{\text{AFC}} = 2\pi/\Delta$ resulting in photon-echo like emission. For a given storage time and optical depth, there is an optimal finesse, F, that maximizes the efficiency. F is defined as the ratio of the comb teeth spacing Δ to the comb tooth width γ. The theoretical maximum storage efficiency in the forward
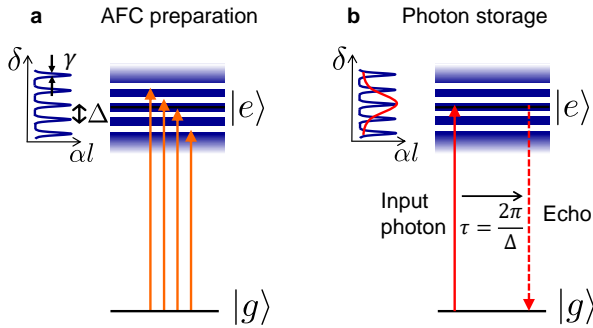
FIGURE 1.6: AFC protocol

direction is 54% but up to unity conversion is possible in the backward direction. Note that the storage time here is predetermined and therefore the light can not be recalled on-demand. However, in the full AFC scheme (*3-level* AFC) [71, 72], the optical excitation can be transferred to the

ground state to be stored as a long-lived spin-wave and then recalled on-demand.

After its first demonstration [18], the AFC protocol was used in several experiments including single photons and qubits storage [34, 64–66].

1.2.2.2 DLCZ

The DLCZ, named after its inventors Duan, Lukin, Cirac and Zoller [49], is an emmissive type of memory protocol, developed to be the basis of a quantum repeater architecture. It makes use of single collective spin excitations in an atomic ensemble. The protocol is depicted in the Fig. 1.7. It uses a three level system in a Λ configuration: two long lived ground
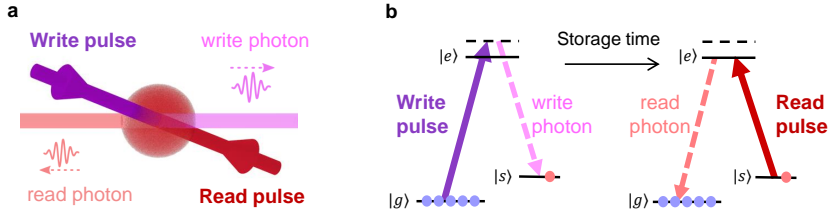
FIGURE 1.7: DLCZ protocol (a) Schematics of the DLCZ protocol on a atomic ensemble. (b) Level schemes.

states $|g\rangle$ and $|s\rangle$ and an excited state $|e\rangle$. All the N atoms are first prepared in the ground state $|g\rangle$. The first step of the protocol is the writing process: a weak pulse, called *write pulse*, off-resonant with the transition $|g\rangle - |e\rangle$, eventually transfers an atom to the $|s\rangle$ state, thus emitting a photon via Raman scattering, called *write photon*. These write photons are strongly correlated with the excitations created in the ensemble. The detection of a write photon heralds a single collective spin excitation - or spin-wave - which can be described directly after detection as

$$|\Psi(0)\rangle = \frac{1}{\sqrt{N}} \sum_{j=1}^{N} e^{i(\boldsymbol{k}_W - \boldsymbol{k}_w).\boldsymbol{r}_j} |g_1 \cdots s_j \cdots g_N\rangle, \qquad (1.6)$$

13

where $\boldsymbol{r}_j$ is the position of atom j, and $\boldsymbol{k}_W$ and $\boldsymbol{k}_w$ are the wave vectors of the write pulse and write photon respectively. The write photons are emitted isotropically but in practice only one mode is detected (at a small angle with respect to the write pulse to facilitate filtering). To avoid multiple excitations, reducing correlations between the write photons and spin-wave, low optical power is used for the write pulse. Conditioned on the detection of a write photon and after some storage time, the spin-wave can be efficiently read-out. A *read* pulse, sent on the $|s\rangle$-$|e\rangle$, maps the single collective excitation into a single *read* photon. The spatial mode is given by the phase-matching condition $\boldsymbol{k}_r = \boldsymbol{k}_W + \boldsymbol{k}_R - \boldsymbol{k}_w$, with $\boldsymbol{k}_R$ and $\boldsymbol{k}_r$ the wave vectors of the read pulse and read photon respectively. The temporal mode is given by the read pulse temporal waveform [73].

The first demonstrations of non-classical correlations between a spin wave and a photon were reported in Refs. [74, 75] and the first elementary segments of the DLCZ protocol were demonstrated few years later [76–79].

1.2.3 Hybrid quantum networks

As seen in the last sections, a quantum network can be much more powerful than the simple sum of its constituent. Pioneering experiments in this line of research include the photonic coupling of identical quantum nodes, such as atomic ensembles [76, 80, 81], single trapped atoms [30] and ions [29], and solid-state devices [82–84]. However, each platform comes along with individual functionalities, e.g., in terms of processing and storage. Hence, a hybrid quantum network, which benefits from the strengths of different platforms, would offer more capabilities than a network consisting of identical quantum systems.

The main challenge to efficiently interface two different quantum systems via a photonic link, is to obtain strong light-matter interaction between a single mediating photon and both matter systems, whose atomic transitions can differ significantly in wavelength and linewidth.

As a non-exhaustive list, an hybrid network could for instance combine the multiplexed and long lived storage of solid-state systems [48], the processing capabilities of single ions [85] or NV centers in diamonds [86], the efficient single photon emission of molecules and quantum dots [87, 88] and the non-linearity at the single photon level of Rydberg atoms [89].

1.3 Quantum frequency conversion

In the last sections, we have seen that it is necessary to manipulate the optical frequency of the flying qubit, in order to have different types of quantum nodes working with visible light to be compatible with the telecommunication wavelengths but also to be compatible with each-other, thus making hybridization of the quantum network possible. This is achievable using Quantum Frequency Conversion (QFC). In this section, I will introduce QFC based on non-linear interactions.

Non-linear optical effects occur when the response of a material depends non-linearly on the strength of an applied optical field [90]. Together with the development of the first laser systems, the first observations of such processes were made, for instance the second-harmonic generation, experimentally demonstrated by Franken et al. in 1961 [91]. The high non-linearities offered by some materials together with advanced fabrication and phase matching techniques led to the improvement of non-linear effects efficiencies. The conversion of single quanta of light then became possible.

QFC aims for the energy shift of an optical field, in a coherent and noise-free fashion, such that quantum properties are preserved to a high degree. Prem Kumar introduced quantum frequency conversion [67] in 1990 and demonstrated it experimentally one year later [92]. In his experiment, non-classical intensity correlations of squeezed light were preserved through the conversion using a Potassium titanyl phosphate (KTP) crystal. Optical frequency conversions based on three or four-wave mixing processes, have been demonstrated using different platforms. Non-linear effects in atomic

systems can be used to convert single photons [93, 94]. In ref. [93] Radnaev et al. used four-wave mixing in a cold Rubidium cloud and demonstrated quantum frequency conversion to the telecom wavelength of single photons emitted by a second cold atomic cloud. However the most used platform today are periodically poled non-linear crystals using quasi-phase matching technique [95]. In particular waveguides [96, 97], made out of Lithium Niobate or Potassium titanyl phosphate crystals, are used for their ability to confine light in longer distances and is compatible with integrated optics. Theses devices are finally relatively easy of use, and can offer close to unity internal conversion efficiencies [98]. There is also the possibility of using non-linear crystals in a cavity [99]. After cautious optimizations of the cavity parameters, up to 84 % external conversion efficiencies (without counting for filtering and fiber coupling efficiencies) was reported in Ref. [100]. Another promising platform in term of integration capability are microresonators based on Silicon Nitride or Aluminium Nitride waveguides [101, 102] although conversion of non-classical state has not been demonstrated yet. However highly efficient and low noise quantum frequency conversion in photonic crystal fibers using Bragg-scattering four-wave mixing were reported [103, 104].

The high conversion efficiencies offered by these different platforms, led to multiple experiments showing the increase of telecom detection efficiencies [99], the generation of non-classical states of light at a specific wavelength [105, 106], or the manipulation photon spectral bandwidth [107, 108]. Towards connecting quantum nodes to the telecommunication wavelength, a key experiment reported the entanglement between a C-band photon and an up-converted (800 nm) photon [97]. Two important contributions to the field of QFC showed phase-preserved frequency conversion [109, 110]. In the last few years many experiments finally demonstrated the connections of quantum systems to the telecommunication band for long distance communication application, such as quantum dots [111, 112], Rubidium atomic ensembles [93, 113–116], Praseodymium doped crystal [117], trapped ions [118–121] and NV centers [122].

The main challenge of QFC is to achieve high conversion efficiency together with a low noise generation at the target wavelength, given that the required pump light often generates a high amount of noise photons. Depending on the wavelengths of the input signal and the converted photons, we can distinguish between three different cases of noise generation in non-linear materials [98]. One in which the pump field frequency is far below the signal and idler photons, thus making noise-free frequency conversion possible [106, 123, 124]. A second case in which one of the two photons frequencies are close to the pump, where Raman noise is generated [112, 125]. A third case in which the pump field is in between the signal and idler photons and generates non-phase matched parametric fluorescence noise [126]. Note that cascaded conversion using a long wavelength pump, proposed in Ref. [126], is a solution to avoid noise generation at the target wavelength.

Suppression of these broadband noises is then often necessary when converting light at the single photon level. In particular, for photons emitted or absorbed by narrow-band quantum memories, temporal filtering of the noise (using a short detection gate) is limited by the long temporal waveform of the photons. In this case the challenge is therefore to implement efficient and stable narrow-band frequency filtering in order to achieve high signal-to-noise ratio of the converted photons.

A QFC device can also be used as a frequency domain beam splitter, as proposed in Ref. [127]. The idea is to reduce the conversion probability to 50 % such that a photon at the output is in a superposition of two colors. With this idea in mind, Ramsey interferences with single photons in a four-wave mixing process have been reported by Clemmen et al. [128]. Hong-Ou-Mandel interferences between two photons of different colors using a three-wave mixing process have been demonstrated by Kobayashi et al. [129].

1.4   Scope of this thesis

During my PhD, I studied frequency conversion of light compatible with quantum memories. The main result of this thesis is the experimental demonstration of an elementary link between heterogeneous quantum nodes, towards the realization of a hybrid quantum network. I will present the results of the quantum connection between a cold ^{87}Rb atomic ensemble and a Pr^{3+}:Y_2SiO_5 crystal, both systems being promising quantum nodes. This connection was performed using quantum frequency conversion techniques, bridging the wavelength gap between the two memories.

I will start, in chapter 2, by explaining in detail the quantum frequency conversion process. I will then describe two intermediate steps towards the connection between the two disparate nodes: the first one in chapter 3, in which I will describe a frequency converter device, connecting the 606 nm and the telecom wavelengths, that is then used to show the compatibility of the visible Praseodymium based quantum memory with the telecommunication wavelength. The second one, in chapter 4, is the connection of a cold atomic ensemble with the telecom C-band. We showed non-classical correlations between a spin wave stored in the atomic ensemble and a telecom photon. Finally in chapter 5, I will explain how the different systems and the QFC interface are combined to finally demonstrate quantum state transfer between the two disparate systems.

Chapter 2

Theory of Quantum Frequency Conversion

This chapter is largely inspired by Robert W. Boyd's textbook [90] and Jason Pelc's thesis [130]. It describes the theoretical background of quantum frequency conversion, starting with the classical description of non-linear optics and in particular the three-wave mixing process. I will finally give a quantum description of frequency conversion.

2.1 Three wave mixing

To describe non-linear optical phenomena in a dielectric material we consider its polarization (dipole moment per unit volume) $\boldsymbol{P}$ upon its interaction with an optical field. In linear optics $\boldsymbol{P}$ depends linearly on the applied field $\boldsymbol{E}$ as:

$$\boldsymbol{P}_L = \epsilon_0 \chi^{(1)} \boldsymbol{E}, \tag{2.1}$$

where ϵ_0 is the vacuum permittivity, and $\chi^{(1)}$ the linear susceptibility. In non-linear optics one can decompose the polarization as a power series in

the field strength as:

$$\boldsymbol{P} = \epsilon_0 \chi^{(1)} \boldsymbol{E} + \epsilon_0 \sum_{j>1} \chi^{(j)} \boldsymbol{E}^j$$

$$= \boldsymbol{P}_L + \boldsymbol{P}_{NL} \tag{2.2}$$

where $\chi^{(j)}$ are the non-linear optical susceptibilities of order j. The second term is the non-linear component $\boldsymbol{P}_{NL}$ of the polarization.

Let's now consider two electric fields $\boldsymbol{E}_1$ and $\boldsymbol{E}_2$ with frequencies ω_1 and ω_2 respectively in the form:

$$\boldsymbol{E}(t) = \boldsymbol{E}_1 \mathrm{e}^{-i\omega_1 t} + \boldsymbol{E}_2 \mathrm{e}^{-i\omega_2 t} + \text{c.c.} \tag{2.3}$$

The second order non-linear polarization $\boldsymbol{P}_{NL}^{(2)}$, corresponding to 3-wave mixing processes, then becomes

$$
\begin{aligned}
P_{NL}^{(2)}(t) =& \epsilon_0 \chi^{(2)} [E_1^2 \mathrm{e}^{-i2\omega_1 t} + E_2^2 \mathrm{e}^{-i2\omega_2 t} \\
&+ 2E_1 E_2 \mathrm{e}^{-i(\omega_1-\omega_2)t} + 2E_1 E_2 \mathrm{e}^{-i(\omega_1+\omega_2)t} + \text{c.c.}] \\
&+ 2\epsilon_0 \chi^{(2)} [E_1 E_1^* + E_2 E_2^*].
\end{aligned} \tag{2.4}
$$

The polarization of the medium develops here new frequency components: the two first terms ($2\omega_1$ and $2\omega_2$) correspond to the second harmonic generation of each field E_1 and E_2. The two next terms correspond to the difference generation ($\omega_1 - \omega_2$) and sum frequency generation ($\omega_1 + \omega_2$). The non-oscillating term is the DC component of the polarization induced by the optical field and corresponds to optical rectification [131].

The wave equation for the propagation of light through a non-linear medium can be estimated considering Maxwell's equations:

$$\nabla \cdot \boldsymbol{D} = \rho$$
$$\nabla \cdot \boldsymbol{B} = 0$$
$$\nabla \times \boldsymbol{E} = -\frac{\partial \boldsymbol{B}}{\partial t} \tag{2.5}$$
$$\nabla \times \boldsymbol{H} = \frac{\partial \boldsymbol{D}}{\partial t} + \boldsymbol{J}$$

where $\boldsymbol{D} = \epsilon_0 \boldsymbol{E} + \boldsymbol{P}$, ρ is the free charges density, $\boldsymbol{B}$ is the magnetic flux density, $\boldsymbol{H}$ is the magnetic field, $\boldsymbol{J}$ is the current density.

We assume that the material does not contain free charges ($\rho = 0$), neither free currents ($\boldsymbol{J} = 0$) and that the material is non-magnetic ($\boldsymbol{B} = \mu_0 \boldsymbol{H}$). We also consider that the material is non-linear with $\boldsymbol{D} = \epsilon_0 \boldsymbol{E} + \boldsymbol{P}$. Using the above simplifications, and combining Eq. 2.5.3 with Eq. 2.5.4, we obtain:

$$\nabla \times \nabla \times \boldsymbol{E} = -\mu_0 \frac{\partial^2 \boldsymbol{D}}{\partial t^2}$$
$$= -\frac{1}{c^2} \frac{\partial^2 \boldsymbol{E}}{\partial t^2} - \frac{1}{\epsilon_0 c^2} \frac{\partial^2 \boldsymbol{P}}{\partial t^2} \tag{2.6}$$

Using the identity $\nabla \times \nabla \times \boldsymbol{A} = \nabla(\nabla.\boldsymbol{A}) - \nabla^2 \boldsymbol{A}$ and assuming slowly varying amplitude such that $\nabla(\nabla.\boldsymbol{E}) \approx 0$ we find:

$$\nabla^2 \boldsymbol{E} - \frac{1}{c^2} \frac{\partial^2 \boldsymbol{E}}{\partial t^2} = \frac{1}{\epsilon_0 c^2} \frac{\partial^2 \boldsymbol{P}}{\partial t^2}. \tag{2.7}$$

Decomposing $\boldsymbol{D}$ in a linear and non-linear terms as $\boldsymbol{D} = \boldsymbol{D}^{(1)} + \boldsymbol{P}_{NL}$, where $\boldsymbol{D}^{(1)} = \epsilon_0 \epsilon_1 \boldsymbol{E}$ and $\epsilon_1 = n^2$ with n the refractive index, we can write Eq. 2.7 as:

$$\nabla^2 \boldsymbol{E} - \frac{\epsilon_1}{c^2} \frac{\partial^2 \boldsymbol{E}}{\partial t^2} = \frac{1}{\epsilon_0 c^2} \frac{\partial^2 \boldsymbol{P}_{NL}}{\partial t^2}. \tag{2.8}$$

This is a driven wave equation. Therefore the non-linear dielectric medium acts as a source upon its interaction with optical fields.

We now assume two collimated optical fields E_1, E_2 and E_3 interacting in a lossless optical medium and propagating along the z direction. This is a good approximation of a waveguide. In the absence of non-linear term the solution of Eq. 2.8 is a such that

$$E_i(x, y, z, t) = \zeta_i u_i(x, y) A_i(z) e^{-i(k_i z - w_i t) + \text{c.c.}}, \quad (2.9)$$

where $k_i = \frac{n_i \omega_i}{c}$ with $n_i^2 = \epsilon_1(\omega_i)$ the effective refractive index of mode i, $\zeta_i = \sqrt{\frac{2Z_0}{n_j \hbar \omega_i}}$ is a scale factor with $Z_0 = \sqrt{\frac{\mu_0}{\epsilon_0}}$, and $A_i(z)$ is the amplitude (slowly varying envelope) of mode i. u_i is the spatial mode of the optical field i propagating in a waveguide for example.

The non-linear polarization components at the three considered frequencies ω_1, ω_2 and ω_3 are [130]

$$\begin{aligned}
P_{NL}(\omega_1) &= \epsilon_0 \chi^{(2)} E_2(\omega_2) E_3^*(\omega_3) \\
P_{NL}(\omega_2) &= \epsilon_0 \chi^{(2)} E_1(\omega_1) E_3^*(\omega_3) \\
P_{NL}(\omega_3) &= \epsilon_0 \chi^{(2)} E_1(\omega_1) E_2^*(\omega_2).
\end{aligned} \quad (2.10)$$

Using the solution Eq. 2.9, combining Eq. 2.8 and Eq. 2.10 and assuming slowly varying amplitude approximation ($\left| \frac{\partial^2 A_i}{\partial z^2} \right| \ll \left| k_i \frac{\partial A_i}{\partial z} \right|$) we find the following coupled equations:

$$\begin{aligned}
\frac{dA_1}{dz} &= -i\kappa A_2^* A_3 e^{-i\Delta kz} \\
\frac{dA_2}{dz} &= -i\kappa A_1^* A_3 e^{-i\Delta kz} \\
\frac{dA_3}{dz} &= -i\kappa A_1 A_2 e^{i\Delta kz},
\end{aligned} \quad (2.11)$$

where $\kappa = \epsilon_0 \frac{\chi^{(2)}}{2} \left(\frac{2\hbar \omega_1 \omega_2 \omega_3 Z_0^3}{n_1 n_2 n_3} \right)^{1/2} \Theta$ is the coupling coefficient. Θ is the mode overlap given by

$$\Theta = \iint \chi^{(2)}(x, y) u_1(x, y) u_2(x, y) u_3(x, y) dx dy. \quad (2.12)$$

Δk is the phase mismatch ($\Delta k = k_1 + k_2 - k_3$ for sum frequency generation or $\Delta k = k_1 - k_2 - k_3$ for difference frequency generation).

Here we consider that a weak signal A_1 is converted by a strong pump A_2 to a field A_3. We assume the pump undepleted ($A_2(z) = A_2(z = 0) = A_p$ and $\frac{dA_2}{dz} = 0$), perfect phase matching ($\Delta k = 0$) and the initial conditions $A_1(z = 0) = A_{10}$ and $A_3(z = 0) = 0$. We find the following solutions for the signal and converted amplitudes:

$$
\begin{aligned}
A_1(z) &= A_{10} \cos(\gamma z) \\
A_3(z) &= A_{10} \sin(\gamma z),
\end{aligned}
\tag{2.13}
$$

where $\gamma = \kappa A_p e^{-i\pi/2}$.

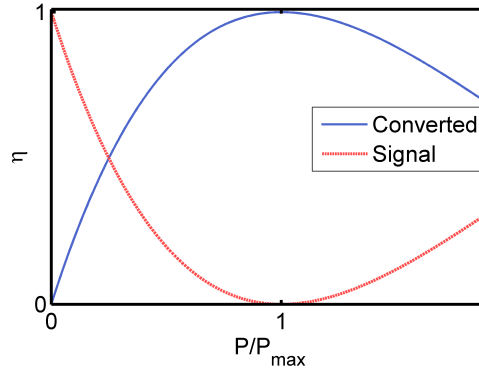FIGURE 2.1: Conversion efficiency (solid blue line) following Eq. 2.14 and depletion of the signal (dashed red line) as a function of the pump power.

We define the conversion efficiency as the ratio of the intensity of the converted field at the output of the waveguide of length L by the input field intensity is

$$
\eta = \frac{|A_3(L)|^2}{|A_{10}|^2} = \eta_{\max} \sin^2(\sqrt{\eta_n P} L),
\tag{2.14}
$$

where $\eta_n = \kappa^2$ is the normalized efficiency and $P = |A_2|^2$ is the pump power. The parameter η_{max} is here added to take into account experimental imperfections (losses or non-perfect mode matching in a waveguide).

2.1.1 Quasi-phase matching

In the first section we saw that the response of a material on a optical field can be non-linear with the effect that each atom of the material has a dipole moment that oscillates with different frequency components (Eq. 2.10). For the material to radiate constructively a new field at a new frequency, the ensemble of N atoms must oscillate in phase. This is known as the phase matching condition $\Delta k = 0$. For example for sum frequency generation the phase matching condition is $\frac{n_1 \omega_1}{c} + \frac{n_2 \omega_2}{c} = \frac{n_3 \omega_3}{c}$. Phase matching is often difficult to achieve in a collinear configuration as the refractive index increases with the frequency (dispersion). This issue can be solved using the birefringence properties of some materials (dependence of the refractive index on the polarization of the field). Fine tuning can then either be achieved by angle tuning of the interacting beams or the temperature of the crystal. However it is limited to some frequency ranges or types of materials.

The technique currently widely used is the quasi-phase matching technique using periodically poled non-linear materials in which the orientation of one crystalline axis is inverted periodically. As a result, the non-linear coefficient is inverted every half period $\Lambda/2$. The effect of a periodic poling on an emitted field is shown in Fig. 2.2. Without phase matching, the generated field oscillates around zero as a function of the distance. The idea of QPM is to inverse the sign of the non-linear coupling coefficient every time the generated field would start decreasing due to phase mismatch. As a result the field adds up constructively. The period Λ must be twice the coherent length $L_{\mathrm{coh}} = \pi/\Delta k$. In that case the wavevector mismatch is now $\Delta k_{\mathrm{QPM}} = \Delta k - 2\pi/\Lambda$ and can be set to zero with the right poling period. Fine tuning can then be performed with the crystal angle or temperature.
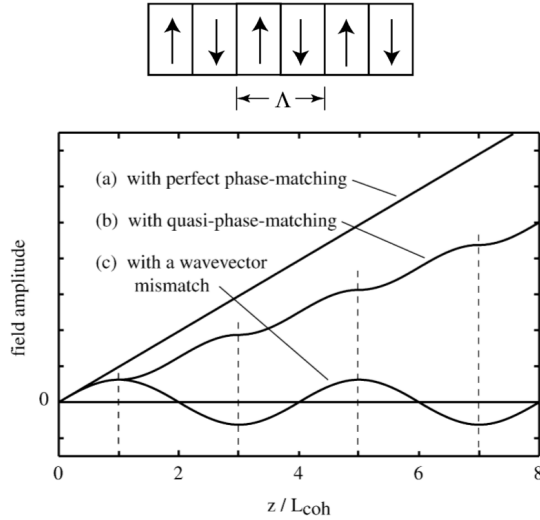
FIGURE 2.2: Quasi-phase matching. Converted field amplitude as a function of the length of the crystal for different phase matching conditions. Figure taken from Ref. [90].

2.2 Quantum description

To describe the frequency conversion of quantum states of light, a quantum approach must be taken. We therefore use the annihilation and creations operators $\hat{a}_i$ and $\hat{a}_i^\dagger$ for signal and converted states, instead of the envelope fields A_i introduced in the previous classical description. $\hat{a}_i$ $(\hat{a}_i^\dagger)$ annihilates (creates) a photon at frequency ω_i. They obey the following commutation relation $[\hat{a}_j, \hat{a}_k^\dagger] = \delta_{jk}$. Applied on a Fock state they have the property

$$
\begin{aligned}
\hat{a}|n\rangle &= \sqrt{n}|n-1\rangle \\
\hat{a}^\dagger|n\rangle &= \sqrt{n+1}|n+1\rangle
\end{aligned}
\tag{2.15}
$$

For consistency with the classical description, we consider a photon that can swap between the frequencies ω_1 and ω_3 using its interaction in a non-linear medium with a pump field at frequency ω_2. Such process can be described with a field interaction Hamiltonian. We here consider that the

pump field A_2 is classical as described in [67]:

$$\hat{\mathcal{H}} = i\hbar\kappa A_2^* \hat{a}_1 \hat{a}_3^\dagger - i\hbar\kappa^* A_2 \hat{a}_3 \hat{a}_1^\dagger. \tag{2.16}$$

In the Heisenberg picture the evolution of an operator $\hat{O}$ with time is given by

$$\frac{d\hat{O}}{dt} = \frac{i}{\hbar}\left[\hat{\mathcal{H}}, \hat{O}\right]. \tag{2.17}$$

Applying this relation to the Hamiltonian. 2.16, we find the following coupled equations:

$$\begin{aligned}
\frac{d\hat{a}_1}{dt} &= \kappa A_2^* \hat{a}_3 \\
\frac{d\hat{a}_3}{dt} &= -\kappa^* A_2 \hat{a}_1,
\end{aligned} \tag{2.18}$$

that have the solutions

$$\begin{aligned}
\hat{a}_1(t) &= \hat{a}_1(0)\cos(|\kappa A_2|t) + e^{i\phi_p}\hat{a}_3(0)\sin(|\kappa A_2|t) \\
\hat{a}_3(t) &= \hat{a}_3(0)\cos(|\kappa A_2|t) - e^{i\phi_p}\hat{a}_1(0)\sin(|\kappa A_2|t).
\end{aligned} \tag{2.19}$$

For initial conditions $|\Psi(0)\rangle = |n_1(0), n_3(0)\rangle = |1, 0\rangle$ the evolution of the photon number operators can be calculated as

$$\begin{aligned}
\langle\Psi|\hat{n}_1(t)|\Psi\rangle &= \langle\hat{n}_1(0)\rangle\cos^2(|\kappa A_2|t) \\
\langle\Psi|\hat{n}_3(t)|\Psi\rangle &= \langle\hat{n}_1(0)\rangle\sin^2(|\kappa A_2|t),
\end{aligned} \tag{2.20}$$

which evolution is depicted in Fig.2.3. One observes here the same behavior as in the classical case 2.13. At the proper interaction time $t = \frac{\pi}{2|\kappa A_2|}$, the input photon is entirely converted to the other frequency with a phase factor ϕ_p given by the pump field. The final state is now $|\Psi(t = \frac{\pi}{2|\kappa A_2|})\rangle = |0, 1\rangle$, which means that the state is preserved while the photon frequency is shifted.

The Hamiltonian. 2.16 can also be interpreted as a frequency domain beamsplitter. As the coupling can be tuned with the pump field or interaction length, one can also use such device as a frequency domain beam splitter [127] where interference between photons of different colors is possible.
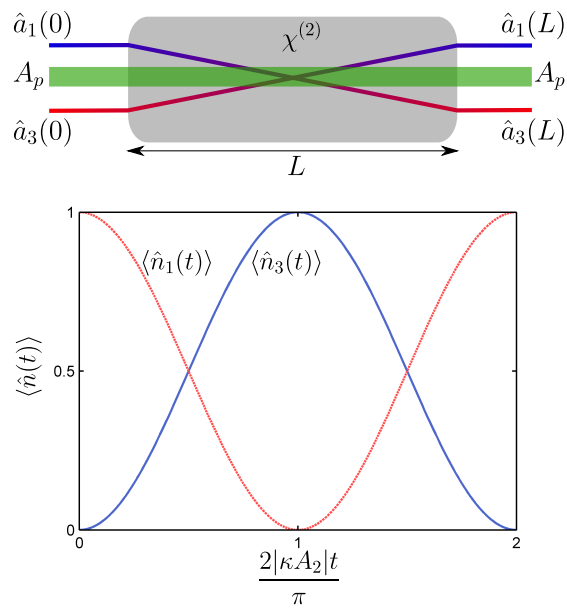
FIGURE 2.3: Top: Input/Output schematics of quantum frequency conversion. Bottom: Photon number time-evolution.

Chapter 3

Quantum Frequency Conversion between 606 nm and the Telecom C-band

In this chapter I will introduce the quantum frequency conversion device, that bridges the gap between the 606 nm and 1552 nm wavelengths, capable of both up and down-conversion of single photons compatible with narrow-band Praseodymium-based quantum memories. In section 3.1 I will first describe the setup and show the classical performances of the converter. In section 3.2 I will describe and characterize the noise processes, and show the conversion of single-photon level light. The two last parts are based on the two following papers [132] and [117]. The first paper, described in section 3.2 and 3.3, shows the down-conversion of storable heralded single photons emitted by a photon pair source. The second one, described in section 3.4, shows the storage in the Pr^{3+}:Y_2SiO_5 quantum memory of up-converted telecom C-band light at the single photon level.

3.1 The frequency converter

In this section I will first describe the setup of the converter device and show the classical performances of the device in both up and down-conversion configuration.

3.1.1 Waveguide

During the PhD we used several commercial non-linear waveguides based on Lithium Niobate (LN) or Potassium Titanyl Phosphate (KTP). The bulk crystals are first periodically poled for quasi phase matching (described in chapter. 2). This is generally done by applying high voltage periodically along the crystal length in order to invert the domain structure and change the sign of the non-linear coefficient [133]. Waveguides are then engineered by creating a guiding channel inside or on top of the crystal. This can be done with different techniques [134], separated in two categories: one in which the refractive index is modified inside the crystal (buried waveguides). Ti-doping for LN, Annealed and reverse proton exchange are the most used techniques. Waveguides can also be fabricated by etching part of the crystal to create a refractive index step with the air (ridge waveguides).

3.1.2 Setup

The frequency converter, depicted in Fig. 3.1, is based on a 1.4 cm long Periodicaly Poled Lithium Niobiate (PPLN) ridge-waveguide (HC Photonics). It is glued with silver paste to a copper mount, itself attached to a Y-translation stage. The crystal chip is actively stabilized in temperature using a Peltier element placed in between the copper mount and the translation stage. The temperature of the mount is measured and stabilized using an home-made proportional-integral-derivative (PID) controller
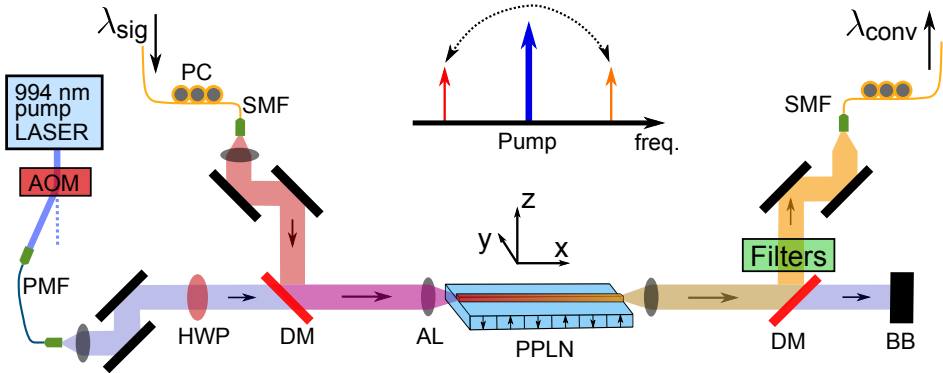
FIGURE 3.1: Setup of the frequency converter device. Acousto Optical Modulator (AOM), Polarization Maintaining Fiber (PMF), Half Wave Plate (HWP), Dicroic Mirror (DM), Polarization Controller (PC), Single Mode Fiber (SMF), Aspheric Lens (AL), Periodically Poled Lithium Niobate (PPLN). Beam Block (BB).

(ICFO) that feedbacks a correction signal on the Peltier device. The converter is here stabilized at around 65 degrees Celsius. At both input and output of the waveguide, XYZ translation stages (Elliot Scientific) hold aspheric lenses that couple or out-couple the light. The 994 nm pump radiation is derived from an external cavity diode (Toptica) and then amplified using a tapered amplifier (Toptica). The amplified light is then sent through a gating acousto-optical modulator (AOM) used to switch on and off the pump field. A polarization maintaining (PM) optical fiber cleans the spatial mode and sends up to 850 mW towards the converter. The polarization of the pump light is controlled by a $\lambda/2$ wave plate. The pump beam is then overlapped with the signal mode using a dicroic mirror and coupled with about 60 % efficiency into the waveguide. At the output, it is separated from the converted mode using a dicroic mirror and finally blocked or monitored, using a photo-diode or a powermeter.

The QFC can be used in both up or down-conversion configuration: either telecom or 606 nm light can be used as signal. They come from single mode fibers and their polarizations are adjusted with polarization controllers. The signal is then reflected onto a dicroic mirror to be overlapped with the pump mode. The converted signal at the output of the waveguide is then

separated from the pump and coupled into a single mode fiber. Depending on the experiment it can be spectrally filtered with several elements (bandpass filter, diffraction grating, fiber Bragg grating, etalon...) and finally detected with a powermeter, photodiode or a single photon detector.

3.1.3 Classical characterization

The classical characterization of the converter device mainly consists in measuring the efficiency of the conversion process. In this thesis it is always defined as the number of photons converted relative to the number of signal photons. Three different efficiencies are defined here: the external, the internal and the device conversion efficiency.

The external conversion efficiency

$$\eta_{\text{ext}} = \frac{\text{P}_{\text{conv}}^{\text{out}}}{\text{P}_{\text{sig}}^{\text{in}}} \frac{\lambda_{\text{conv}}}{\lambda_{\text{sig}}} \tag{3.1}$$

is the conversion efficiency "outside" the waveguide, where $\text{P}_{\text{conv}}^{\text{out}}$ is the power of the converted light measured at the output of the waveguide and $\text{P}_{\text{sig}}^{\text{in}}$ is the power of the input signal measured before the waveguide. The ratio of signal and converted wavelengths $\frac{\lambda_{conv}}{\lambda_{sig}}$ corrects for the energy loss or gain of the converted photon.

The internal efficiency

$$\eta_{\text{int}} = \eta_{\text{ext}} / \eta_{\text{coupling}} \tag{3.2}$$

is the external efficiency, corrected for the coupling efficiency η_{coupling} of the signal in the waveguide. Another way of estimating the internal efficiency is to measure the depletion of the signal after the waveguide:

$$\eta_{\text{depl}} = 1 - \frac{\text{P}_{\text{sig}}^{\text{out}}}{\text{P}_{\text{sig}}^{\text{out}}(P=0)}, \tag{3.3}$$

depending on the ratio of signal power measured after the waveguide with and without pump power P applied. This has the advantage of being insensitive of any losses and calibration errors.

Finally, the device efficiency

$$\eta_{\text{dev}} = \eta_{\text{ext}}\eta_{\text{loss}} \tag{3.4}$$

takes into account all possible losses η_{loss} of the converted light before and after the waveguide. In this thesis it always takes into account a fiber coupling, but also different filtering elements in the converted mode or other optical transmission losses.

3.1.3.1 Sum frequency generation

I first characterized the converter in the up-conversion configuration where 1550 nm telecom light (Toptica DL) is coupled as an input with the 994 nm pump laser, resulting to a converted light at 606 nm via sum frequency generation. Fig 3.2a shows the measured converted light power at the output of the waveguide as a function of the input telecom signal wavelength. It differs from the expected sinc behavior [90], most probably because of imperfections in the poling period of the crystal. The waveguide is here at room temperature and optimized for the conversion of 1549 nm light to 605.5 nm. It will later be stabilized at 65 degrees Celsius to reach the desired phase matching condition of the process: $\frac{1}{1552\,\text{nm}} + \frac{1}{994\,\text{nm}} = \frac{1}{606\,\text{nm}}$.

About 1 mW of continuous wave light at 1552 nm is coupled using an aspheric lens (51 % efficiency) together with the 994 pump with (62 % coupling efficiency). The internal conversion efficiency is plotted as a function of the coupled pump power (red empty squares in Fig 3.2b). It is monitored by measuring the converted signal and correcting for all transmission losses and waveguide coupling efficiency (Eq. 3.2). Up to the available
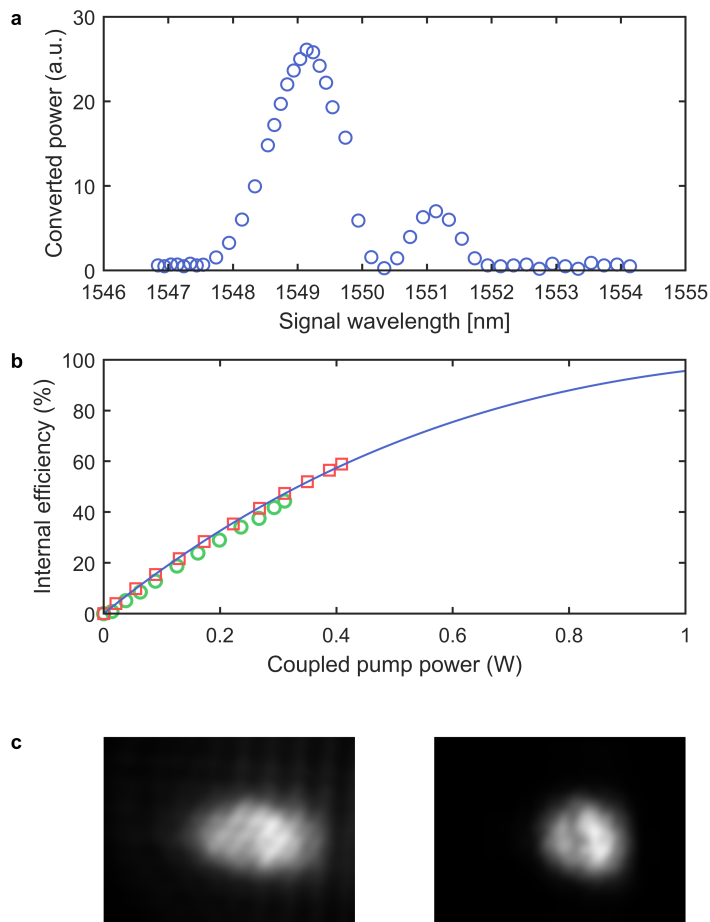
FIGURE 3.2: Classical characterization of the converter. (a) Quasi-phase matching curve: 606 nm converted power as a function of the input telecom signal wavelength. (b) Internal efficiency measurement as a function of the coupled pump power. The internal efficiency measurement is estimated first by measuring the converted signal power (red empty squares) or by measuring the depletion η_{depl} of the coupled input signal (green empty dots). The data from the direct measurement (red squares) is fitted with Eq. 2.14 (blue curve). (c) Spatial mode of the converted 606 nm light measured with a camera (Imaging Source) directly after the waveguide (left) or corrected by an anamorphic prism pair (right).

coupled pump power of 415 mW, we measure an internal conversion efficiency of 59 %. The depletion of the signal (empty green circle) as a function of the pump power is also measured and is always consistent with the internal efficiency measurement, meaning that there are no calibration errors or significant loss of the converted light in the waveguide. The internal efficiency (red squares data points) is fitted with Eq. 2.14 [135]: $\eta_{\mathrm{int}} = \eta_{\mathrm{max}} \sin^2\left(\mathrm{L}\sqrt{\eta_n \mathrm{P}}\right)$. We find that, with η_{max} fixed at the bound of 100 %, the normalized efficiency η_n is $(94\pm1)\,\%\,\mathrm{W}^{-1}\,\mathrm{cm}^{-2}$. This measurement can be imprecise though as changing the pump power often leads to local change of temperature of the waveguide and thus modifies the phase matching condition [136]. It means that, at fixed input wavelength, the temperature of the waveguide has to be slightly re-optimized for each pump power, which can moreover lead to misalignment of the setup. A solution to this problem is shown in the following subsection (down-conversion experiment).

The output mode at 606 nm is measured to be elliptical (Fig 3.2c). In order to increase single-mode fiber coupling efficiency of the converted light, it is circularized by an anamorphic prism pair with an horizontal magnification of 2.5.

In this up-conversion configuration this setup will be used for the experiment described in Chapter 5.

3.1.3.2 Difference frequency generation

In the down-conversion configuration the output mode becomes the input mode and the pump field is coupled from the other side of the converter. Here the pump laser at 994 nm is coupled with 55 % efficiency, together with a 606 nm signal with 57 % coupling efficiency inside the waveguide. The frequency converter is first characterized using classical light as input. The conversion efficiency of the device is measured as a function of the coupled pump power inside the waveguide, using 1 mW of classical input
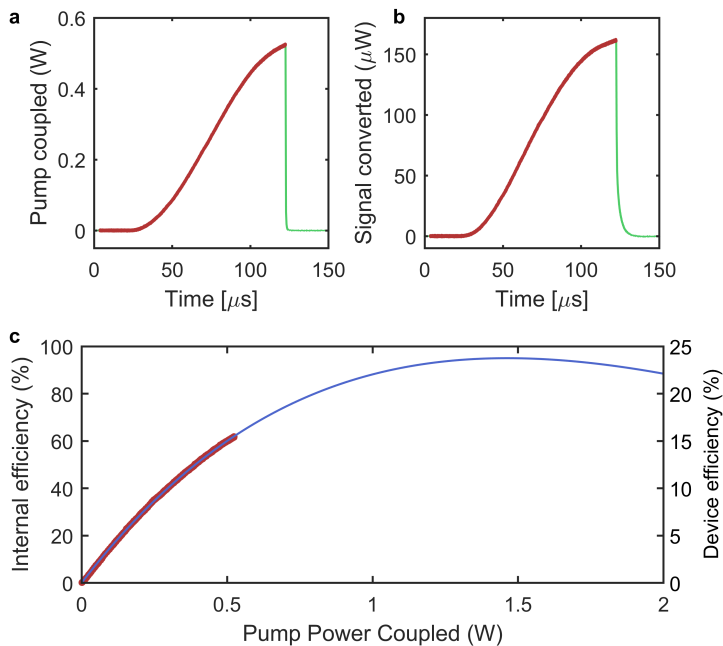
FIGURE 3.3: (a) Monitored pump power after the waveguide using a photodiode. (b) Monitored converted signal power after the waveguide using a second photodiode. The red line is the selected data for the measurement. (c) The red trace shows the internal conversion efficiency as a function of the coupled pump power deduced from the data shown in (a) and (b). The blue curve is a fit of the data using Eq. 2.14

light at 606 nm (derived from Toptica DL SHG pro). The pump power is swept using an AOM over a short time of 100 μs. The coupled pump power and the difference-frequency converted light are then monitored at the output of the waveguide using photodiodes. This fast measurement has the advantage of avoiding thermal effects explained in section 3.1.3.1. The blue trace in Fig. 3.3(a) shows the measured internal efficiency depending on the pump power, inferred by correcting for all losses. At the maximum coupled pump power available of 530 mW, we measure an internal conversion efficiency of 62 %. This value is in accordance with the measured depletion of the 606 nm signal. The device efficiency, also shown on the right axis, includes all optical losses: signal transmission (93 %), coupling efficiency of the signal in the waveguide (57 %), filtering efficiency (62 %)

for single-photon level operation (see next section) and single mode fiber coupling efficiency (79 %) of the converted signal. The conversion efficiency is fitted with the Eq. 2.14. The fit gives a maximum internal efficiency of (95 ± 0.1) % (24.5 % device efficiency) at 1.45 W of coupled pump power and a normalized efficiency of (86.1 ± 0.1) %W^{-1}cm^{-2}. The results are consistent with the up-conversion operation.

In this section we demonstrated the high efficiency of our device, capable of ≈ 15 % conversion efficiency at maximum available pump power. In order to reach the maximum conversion efficiency given by the extrapolation, higher pump powers or a longer waveguide could be used. We would then reach a device efficiency of 25 %. This could also be greatly improved, for example using fiber pigtailed waveguide in order to increase the waveguide coupling efficiency. Higher filtering efficiencies could also be achieved using for instance volume Bragg gratings.

3.2 Down conversion of memory compatible weak coherent states to telecom

Converting single photon level light is more challenging as the converted photons must be detected with high signal-to-noise ratio whereas the converter often generates pump-induced noise photons. In this section I will first describe the different noise processes possible in a conversion experiment and characterize the specific noise involved in the conversion between 606 and 1552 nm light. Finally I will explain how we estimate the performance of our converter device in term of signal-to-noise ratio, and in particular the μ_1 parameter. Finally I show that, using strong filtering of the noise, our QFC is compatible with narrow-band quantum memory. These results are described in Ref. [132].

3.2.1 Noise processes

The noise processes are depicted in Fig. 3.4(a). A strong pump field generally generates Raman noise around its central frequency. In a PPLN waveguide Raman noise has been estimated to have a width of about 30 THz [98, 137]. It therefore does not play a significant role in our experiment, since the frequency shift between the pump and the telecom signal is 109 THz. A second type of noise is weakly-phase matched Spontaneous Parametric Down Conversion (SPDC) noise created by the pump. This noise is enhanced by imperfection in the poling period of the crystal, as described in Ref. [126] and is generated over the region of lower frequencies. When converting from 606 nm to 1552 nm ($\lambda > \lambda_{pump}$) we then observe direct SPDC noise. This process is expected to be linear with the pump field intensity. Part of this noise, within the phase matching bandwidth of the frequency converter, can be eventually converted to 606 nm by the pump field via sum frequency generation. In the case of conversion from 1552 nm to 606 nm ($\lambda < \lambda_{pump}$), the expected behavior is therefore very

different as the reconversion of the noise leads to a quadratic dependence with pump power.

We measure the noise using only the pump as the input of the waveguide, and detecting the photons either at the 1552 nm output or at the 606 nm output. In order to limit the noise detected, we use filtering stages in each output modes. The 606 nm noise is filtered with a diffraction grating and an etalon (10 GHz bandwidth) and the telecom noise is filtered with a fiber Bragg grating (2.5 GHz) and an etalon (210 MHz). Figs. 3.4(b and c) show the noise count rates at the telecom and 606 nm wavelengths, at the output of the waveguide and normalized as counts per seconds over 1 GHz bandwidth. The telecom noise (Figs. 3.4b) saturates as a function of the pump power due to the above explained back-conversion to 606 nm. This gives approximately a factor 2 reduction of the expected linear noise at the maximum pump power. Taking the first 3 points to fit a linear slope, we find an internal SPDC noise generation coefficient of α_N=76 kHz/mW/cm normalized to a 1 THz bandwidth, similar as the one described in Ref. [138]. The blue curve, matching our data, shows a simple model of the expected noise level taking into account α_N and the back-conversion effect as:

$$N_{telecom}(P) = \alpha_N P \int_0^L \left(1 - \eta_{max} \sin^2\left((L-x)\sqrt{\eta_n P}\right)\right) dx, \qquad (3.5)$$

where the parameters η_{max} and η_n are the efficiencies found with the classical conversion efficiency measurement. The converted noise detected at 606 nm (Figs. 3.4c) shows a clear quadratic behavior, as expected. The red line shows the expected back-converted noise level using the same model as Eq. 3.5:

$$N_{606}(P) = \alpha_N P \int_0^L \eta_{max} \sin^2((L-x)\sqrt{\eta_n P}) dx. \qquad (3.6)$$

The expected behavior of the signal-to-noise ratio of a converted photon as a function of the pump power are shown in Figs. 3.4(d-e). It takes into account the classical efficiency measurement (section 3.1.3.2) and the noise models 3.5 and 3.6.
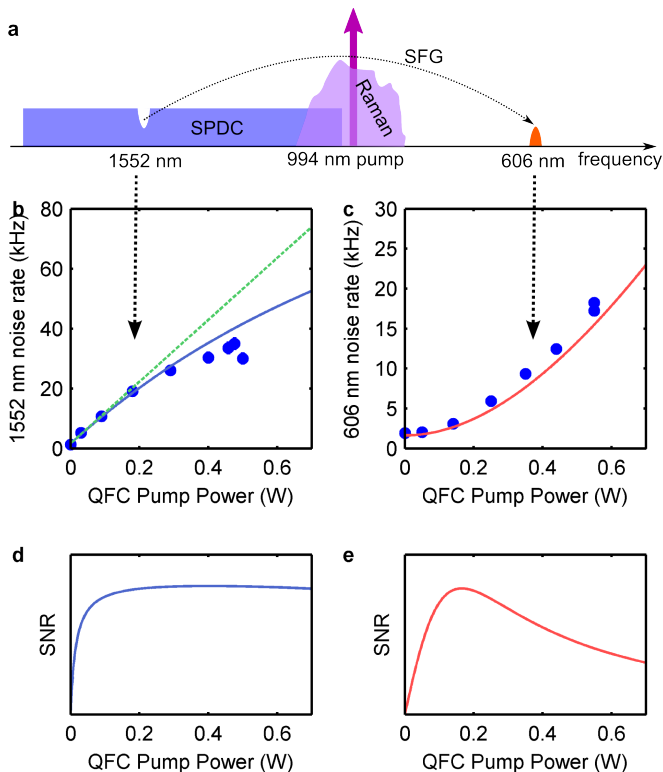
FIGURE 3.4: QFC noise characterization. (a) Schematic of the different noise processes induced by a strong pump field in the waveguide. (b) Measurement of noise in the 1552 nm region, dominated by Spontaneous Parametric Down Conversion (SPDC) noise photons, as a function of the pump power coupled in the waveguide. (c) Noise measurement in the 606 nm region. The two measurements are performed gating the single-photon detector and using the narrow band filters shown in the setup section (of 10 GHz bandwidth for the 606 nm photons and 210 MHz bandwidth for the converted 1552 nm photons). The data are normalized as counts per second at the output of the waveguide, over 1 GHz bandwidth assuming a continuous measurement (i.e. eliminating temporal gate). (d-e) Expected behavior of the signal-to-noise ratio of a down-converted (d) or up-converted (e) photon taking into account the classical efficiency measurement and the noise models shown in plots b and c. This figure is meant to show the behavior of the SNR and does not show quantitative numbers which depends on the experimental parameters.

3.2.2 The μ_1 measurement - Weak coherent states down-conversion

To estimate the performance in term of signal-to-noise ratio of our noisy device, a typical measurement that will be shown all along the manuscript, is the so called μ_1 measurement. It gives the number of input photons μ_{in} per pulse at the input of the device, such that the signal-to-noise ratio (SNR) of the converted photon at the output of the device is equal to 1: $\mu_1 = \frac{\mu_{\text{in}}}{\text{SNR}}$ [125]. In practice it is estimated by measuring the SNR of the converted photon for several input photons number per pulses of attenuated laser light (weak coherent states) and by fitting a linear function to it.

This parameter depends on the external conversion efficiency, on the noise filtering applied to the converted mode, but also on the photon duration used (as the amount of noise detected depends on the integration window duration). μ_1 is a practical and useful parameter to estimate the feasibility of connecting the converter to a specific system with a specific bandwidth. A single photon, heralded with an efficiency η_{herald}, can be converted with a SNR $= \frac{\eta_{\text{herald}}}{\mu_1}$.

To assess the potential of our QFC device for converting light emitted by narrow-band quantum memories to the telecom wavelength, we characterize it sending 606 nm weak coherent states with 200 ns FWHM Gaussian shape, mimicking long single photons compatible with Praseodymium doped quantum memories [19, 66, 139]. To reduce this amount of detected noise, the converted telecom photon is filtered with a fiber Bragg grating (65 % transmission, 2.5 GHz bandwidth) and an etalon (95 % transmission, 210 MHz bandwidth and free spectral range (FSR) of 4 GHz). The converted photons are then detected with an InGaAs single photon detector (ID230, ID Quantique, 10 % efficiency, 10 Hz dark counts) and integrated over a 400 ns time window, containing more than 98 % of the pulses. Fig. 3.5 a and b show examples of histograms of the converted photons for 0.3 input photon number per pulse, without the etalon (a) and with the
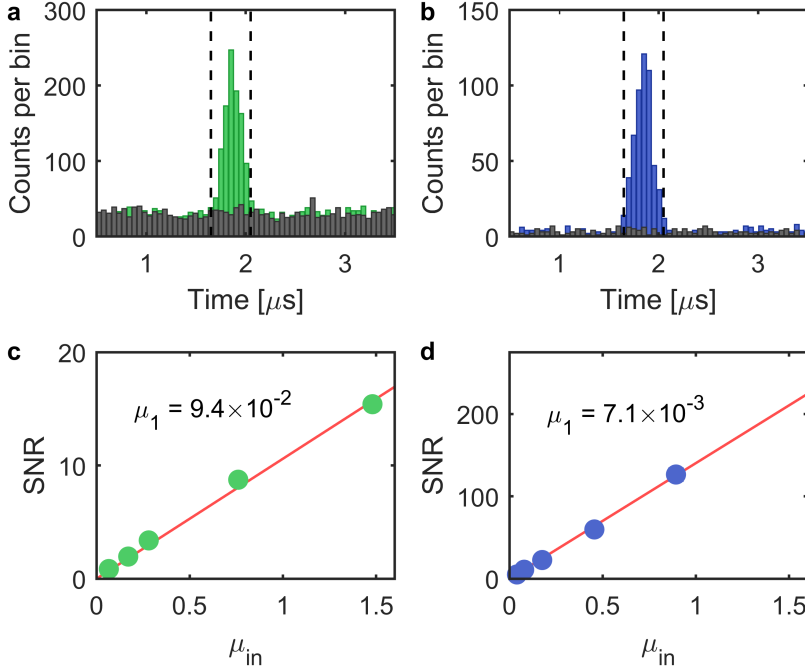
FIGURE 3.5: μ_1 measurements. Figure (a) show the histogram (51 ns bin size) of converted weak coherent states with an input photon number of 0.3 per pulse at 606 nm. The 1552 nm converted signal is filtered with a Fiber Bragg grating (2.5 GHz bandwidth) and measured over 400 ns integration window. The grey histogram shows the noise level measured, for which a 6 μs integration window is used. Figure (c) shows the SNR as a function of the input photon number per pulse, together with the fit of the data, revealing the μ_1 parameter. Figures (b and d) show the same measurement done adding a filtering etalon of 210 MHz bandwidth, which increases significantly the SNR.

etalon (b) showing strong noise suppression. We then measured the signal to noise ratio of the converted photons

$$\text{SNR} = \frac{C_{\text{conv}} - C_{\text{noise}}}{C_{\text{noise}}}, \tag{3.7}$$

where $C_{\text{conv}}(C_{\text{noise}})$ is the number of converted (noise) photon counts in the integration window. It is measured with different average input photon numbers per pulse, ranging from 0.04 to 1 and from a linear fit we extract the parameter μ_1 (Fig 3.5c d). We show that adding the etalon as a filter

42
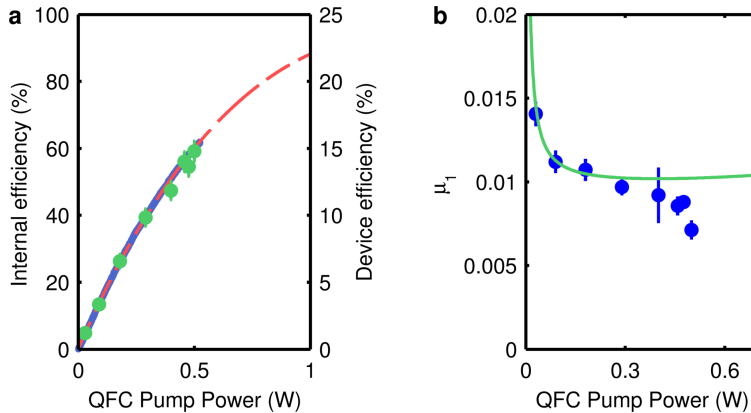
FIGURE 3.6: QFC performances. (a) Conversion efficiency from 606 nm to 1552 nm as a function of the coupled pump power. The blue curve shows the efficiency using bright classical light and sweeping the coupled pump power from 0 to 530 mW in 100 μs. The red curve shows the fit of the efficiency shown in section 3.1.3.2. The greens points show the efficiency measured with weak coherent states. (b) μ_1 measurements of the converted weak coherent states as a function of the coupled pump power.

decreases by on order of magnitude the μ_1, compatible with the filtering bandwidth improvement. This confirms that the noise is broadband.

Fig. 3.6(b) shows a measurement of μ_1 (with the full filtering) as a function of the pump power. Interestingly, we observe a decrease in μ_1 with increasing pump power, down to $(7 \pm 0.5) \times 10^{-3}$ at $500\,\text{mW}$ pump power. Although not intuitive, the decrease of μ_1 (i.e increase of SNR) with the pump power is explained by the saturation of the noise at telecom in the waveguide, discussed in the previous section. The green curve shows the expected values of the μ_1, calculated from the classical conversion efficiency measurement, and the noise level (eq. 3.5). The device efficiency is also extracted from this measurement and plotted in Fig. 3.6(a), matching with the classical measurement.

These measurements show the capability of converting long photons with high signal to noise ratio, thanks to the high efficiency of the process and to the strong spectral filtering of the QFC noise.

3.3 Down-conversion of storable heralded single photons to the telecom C-band

To prove that our QFC device preserves the quantum properties of memory compatible quantum light, we use a photon pair source, schematically depicted in Fig. 3.7(b), that generates heralded single photons at 606 nm compatible with the Praseodymium based quantum memory [66, 139]. This experiment has been performed together with Dario Lago-Rivera [132] who was operating the photon pair source. We show that non-classical correlations between heralding and heralded photons are preserved. We also measured the heralded autocorrelation function of the heralded photon using the converter device as a frequency-domain beam splitter, yielding a value of 0.19±0.07. The results are published in Ref. [132].

3.3.1 The photon pair source

The source is a new generation of an earlier source [140, 141] that has been used to to demonstrate quantum storage of heralded single photons in a Pr^{3+}:Y_2SiO_5 memory [66, 139]. It is based on a 2 cm long PPLN crystal, placed in a bow-tie cavity (FSR of 261 MHz). Pumped with 426 nm light in CW, it generates a signal photon at 606 nm, and an idler photon at 1436 nm. The biphoton linewidth is 1.8 MHz, making the 606 nm photon compatible for storage in a Pr^{3+}:Y_2SiO_5 based quantum memory [66, 139]. The idler telecom photon is filtered with a Fabry-Perot cavity (linewidth of 80 MHz, FSR = 17 GHz) in order to select a single frequency mode out of the 8 modes at the output of the bow-tie cavity. It is then used to herald the signal 606 nm photon with an efficiency η_S^h of 25 % in single mode fiber. In the 606 nm arm, there is no filtering of a single frequency mode and the non-correlated modes contribute to accidental coincidences. Pumped with 1.65 mW of 426 nm light, the source generates about 280 heralded 606 nm photons per second which are strongly non-classically correlated to the heralding photon. This number is limited by the transmission of the

a Quantum frequency converter

b Photon pair source
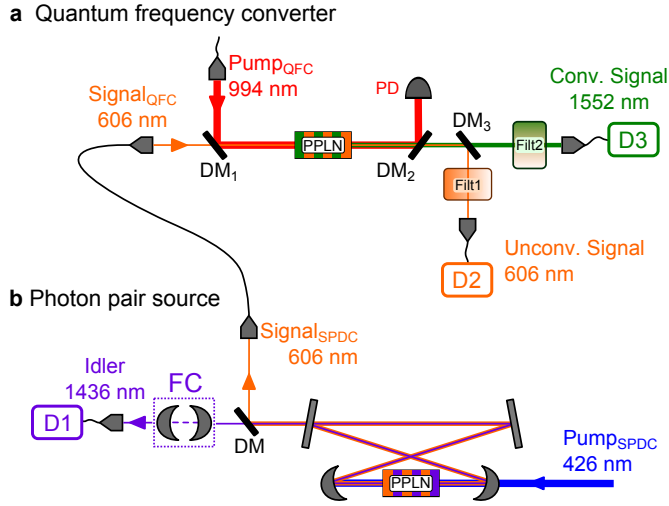
FIGURE 3.7: (a) QFC setup. At the input of the device, single photons at 606 nm can be coupled together with a strong 994 nm pump into the Periodically Poled Lithium Niobate (PPLN) waveguide. At the output, the pump, the unconverted and the converted lights are separated by means of Dicroic Mirrors (DM). The coupled pump is monitored with a Photodiode (PD). The unconverted and the converted fields go through filtering stages and are coupled into a single mode fiber. Finally they are detected with single-photons detectors (D2 and D3) (b) Source setup. The photon pair source consists of a PPLN crystal inside a bow-tie cavity. It is pumped with a 426 nm continuous-wave laser beam. The generated idler photon at 1436 nm and signal photon at 606 nm are doubly resonant with the cavity. At the output of the cavity they are separated by means of a dicroir mirror. The idler photon passes through a Filter Cavity (FC), is then coupled to a single mode fiber and finally detected at D1. The 606 photon is also coupled to a single mode fiber and sent to the quantum frequency converter.

heralding photons (filtering cavity and fiber coupling) and their detection at D1 (10 % efficiency). The correlation time of the photon pair is measured to be 120.9 ns. We measure the normalized cross correlation function $g_{s,i}^{(2)} = \frac{P_{s,i}}{P_s P_i}$, where $P_{s,i}$ describes the probability for a coincidence detection of a signal and an idler photon, and P_s (P_i) is the detection probabilities for single signal (idler) events. Using a detection window of 400 ns we obtain $g_{s,i}^{(2)} = 15.9 \pm 0.9$, well above the classical threshold of 2, assuming thermal statistics for the signal and idler fields. The single photon nature of the heralded 606 nm photon is verified measuring the heralded second-order

autocorrelation function $g^{(2)}_{H,source}$. This is done using a 50/50 fiber-beam splitter in the 606 nm arm and detecting the heralded correlations between the two outputs. The source exhibits $g^{(2)}_{H,source} = 0.12 \pm 0.01$, well below the classical threshold of 1, and below the threshold of 0.5 for a two photon Fock state.

3.3.2 Preservation of non-classical correlations and frequency-domain beam splitter

Finally, we connect the photon pair source to the quantum frequency converter. The correlations between the herald and the non-converted signal (detectors D1 and D2), and between the herald and the converted signal (detectors D1 and D3) are measured as a function of the QFC pump power and are shown in Fig. 3.8(a). At 0 mW pump power, the normalized cross correlation function of 13.6±0.9 for the non-converted light (grey open squares) corresponds to the source without any effect of the QFC (except for the additional transmission losses). The $g^{(2)}_{s,i}$ value for the non-converted photons then rapidly drops when increasing the pump power due to the drop of SNR induced by the high amount of quadratic noise generated through the 10 GHz etalon filter. In contrast, when looking at the 1552 nm converted signal (blue dots) we observe that the value of $g^{(2)}_{s,i}$ slightly increases with pump power up to 12.3 ±0.7 at 440 mW. It is worth mentioning that the filtering stage of the converted signal used to obtain a high SNR of the converted photon also filters a single frequency mode from the bow-tie cavity. It then reduces the number of accidentals coincidences from the source, as the other modes, non-correlated with the single frequency idler mode, are not detected. On the contrary, the QFC itself adds noise to the channel, thus reducing the cross correlation function. Thus it is difficult to directly compare the converted cross correlation function with the non-converted one shown in the Figure 3.8(a). Instead we measured the cross-correlation $g^{(2)}_{s,i}$ of the source before the QFC sending the 606 nm heralded single-photon through a 12 MHz transparency window of
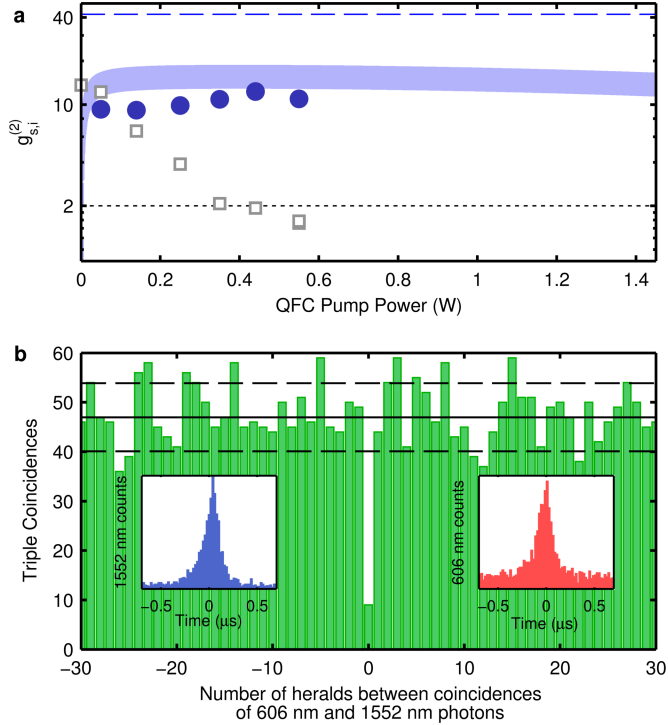
FIGURE 3.8: Non-classical correlations. (a) Cross correlation measurement between the 1436 nm heralding photon and the converted 1552 nm photon (blue dots) The blue shaded area shows the expected values taking into account the SNR of the converted light and the estimated cross-correlations for the source in single mode before the conversion. The grey open squares show the depleted 606 nm photon as a function of the coupled pump power of the QFC. Error bars are smaller than the points. The dotted line represents the classical threshold of 2. The dashed blue line represents the measured cross-correlation of the source in single mode configuration for signal and idler. (b) Histogram of the triple coincidence between the heralding photon, the 1552 converted photon and the 606 unconverted photon, measured with 250 mW of coupled QFC power. The left (right) inset shows the histogram of the heralded converted (unconverted) photons.

a $Pr^{3+}:Y_2SiO_2$ doped crystal [139], that filters a single frequency mode of the bow tie cavity and measure $g_{s,i}^{(2)} = 42\pm7$. We now have an estimate of the performance of the source in fully single mode operation that can be compared with the converted one measured (blue dots in Fig. 3.8(a)). The effect of the noise of the QFC device on correlations can be estimated using the same approach as in Ref.[113]:

$$g_{c,i}^{(2)} = g_{s,i}^{(2)} \frac{\eta_S^h/\mu_1 + 1}{\eta_S^h/\mu_1 + g_{s,i}^{(2)}}, \tag{3.8}$$

where $g_{c,i}^{(2)}$ ($g_{s,i}^{(2)}$) is the cross-correlation function of the converted (unconverted) photon. We plot the expected correlations after conversion (blue shaded area in Fig. 3.8(a)) using the μ_1 model shown previously (green curve of Fig. 3.6(b)). We can then observe that, up to the pump power of 1.45 W for which the maximum conversion efficiency should occur, the correlations, although degraded by the QFC-induced noise, remain well above the classical limit of 2. The model suggests that the converted light can exhibit non-classical correlations at any pump power. The small discrepancy between the measured data and the model is probably due to an overestimation of the non-converted correlations as the filtering is much narrower in that case.

In order to show the preservation of the single photon nature of the converted heralded photon, we measure – for the first time to our knowledge – the heralded-autocorrelation function of the signal photon using the QFC as a frequency-domain beam splitter [128, 129]. The pump power of the QFC can be tuned in such a way that the photon entering the waveguide has a probability of 50 % to be converted and 50 % to stay in its original state (Eq. 2.16). We can then record the triple coincidences between the heralding photon at D1, the unconverted 606 photon at D2 and the converted 1552 nm photon at D3 to measure the heralded autocorrelation function $g_{s,c|i}^{(2)}$ in a 400 ns window. To equalize the photon detection rates between the two outputs of the frequency beam splitter we fix the QFC pump power at 250 mW, which also dramatically reduces the amount of

quadratic noise detected at D2. The histogram of the triple coincidence is shown in Fig. 3.8(b), sorted by the number of heralding events between succeeding detections at signal or converted photon detectors [142]. The value at bin 0 corresponds to $g^{(2)}_{s,c|i}$ of 0.19±0.07. It is well below the classical threshold and proves the single photon nature of the converted light. Note that this value is an upper bound as a high amount of uncorrelated noise is added to the non-converted output of the beam splitter. This measurement also highlights the potential of a quantum frequency converter as a beam splitter device, which for instance could be used to perform Bell measurements between modes of different wavelength [127].

3.4 Storage of up-converted telecom C-band photons in a doped crystal

Of great interest to long distance quantum communication is the implementation of a quantum memory for telecommunication light (1550 nm). It is well known that telecom C-band optical fibers have the least loss (0.2 dB/km), so a telecom optical memory would integrate directly with fiber-optical networks and quantum repeater architectures.

In this section, I will present the storage of up-converted single-photon level telecom light at 1570 nm, in a Praseodymium doped crystal, using the Atomic Frequency Comb protocol (introduced in section 1.2.2.1). This experiment was performed in 2014 [117] together with Kutlu Kutluer who was operating the Praseodymium doped quantum memory. I will first describe the converter device and the solid state memory. Finally I will show that the up-converted photons can be retrieved after storage, with high signal-to-noise ratio.

3.4.1 The frequency converter

The frequency converter used for this experiment is a 2.6 cm long Periodically-Poled Potassium Titanyl Phosphate (PPKTP) waveguide, used in the early stage of the PhD. It is quasi-phased matched for the sum-frequency generation process $\frac{1}{1570\,\text{nm}} + \frac{1}{987\,\text{nm}} = \frac{1}{606\,\text{nm}}$. The setup is very similar to the one described previously in section 3.1. The telecom light, coupled with 55 % efficiency, is overlapped in the waveguide with the 987 pump, coupled with 36 % efficiency. The converted light at 606 nm is filtered with a diffraction grating (Thorlabs, GR13-1205) and an etalon (Light Machinery) with finesse 6 and linewidth 10 GHz. It is finally coupled to a telecom fiber, slightly multimode for 606nm but allowing for an efficient coupling of 75 %. At maximum coupled pump power available of 252 mW, the measured device efficiency is 21±1 %, corresponding to 75 % internal efficiency.
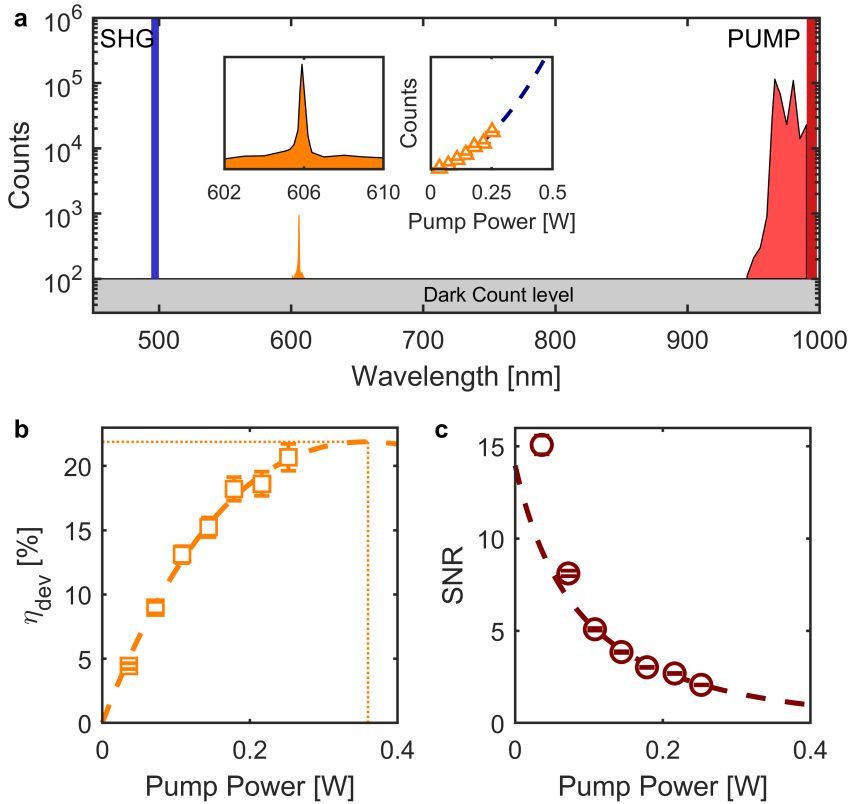
FIGURE 3.9: PPKTP characterization. (a) Visible noise spectrum of the PPKTP waveguide with a 994 nm coupled pump. The left inset shows a closer look at the data around 606 nm. The right inset shows the dependence of the noise at 606 nm with the pump power. Note that some optical elements used in this measurement were optimized for 606 nm and not for wavelengths around 1 μm. (b and c) Weak coherent state conversion. Device efficiency (b) and signal-to-noise ratio (c) measured for an input photon number per pulse of μ_{in}=1, as a function of the coupled pump power.

In a PPKTP waveguide the noise processes are similar as in a PPLN waveguide. To verify this, we measured the spectrum of the noise in the visible range using a monochromator (Horiba microHR, 0.25 nm resolution at 400 nm). Only the pump field was sent at the input of the waveguide, and the dicroic mirror and filtering stage were removed. The data is shown in Fig. 3.9. We observe the anti-Stoke Raman noise up to 14 THz above the pump frequency. At the conversion target 606 nm wavelength, we observe a noise peak. Its width is limited by the resolution of the monochromator. It is quadratic with pump power (see right inset of Fig.3.9(a)), clearly showing that it is parametric down-conversion noise, back-converted to 606 nm within the phase matching bandwidth.

The converter is then characterized converting weak coherent states with 1 average photon per 140 ns long pulses, as a function of the pump power coupled. From this measurement, the device efficiency (Fig 3.9a) and the signal to noise ratio (Fig 3.9b) are extracted. The fit of the efficiency using Eq. 2.14 gives a maximum device efficiency of $\eta_{\mathrm{dev}} = (22 \pm 1\,\%)$ at 360 mW of pump and a normalized efficiency of $\eta_n = 100 \pm 10\,\%/\mathrm{W\,cm^2}$. The signal to noise ratio decreases dramatically with pump power, as expected for a quadratic noise behavior.

3.4.2 The solid state memory

The building of the solid state memory setup was not part of my PhD. However I will briefly describe it here. The solid state storage device is based on the atomic frequency comb (AFC) protocol [70], described in section 1.2.2.1. As the memory medium, we use a 5 mm long $\mathrm{Pr^{3+}:Y_2SiO_5}$ crystal with 0.05 % doping leading to an absorption coefficient of $23\,\mathrm{cm^{-1}}$ with light polarized along the $\mathrm{D_2}$ crystal axis. For light polarized along the $\mathrm{D_1}$ axis, the absorption coefficient is reduced greatly [143]. The transition of interest is at 606 nm which connects the first sublevels of the $^3\mathrm{H_4}$ ground and the $^1\mathrm{D_2}$ excited manifolds. To cool this crystal down to 3 Kelvin we use a Montana Instruments Cryostation. For this experiment only the 606 nm

a

b

$^1D_2(1)$ ± 5/2e
4.8 MHz ± 3/2e
4.6 MHz ± 1/2e

605.977 nm

± 1/2g
10.2 MHz
$^3H_4(1)$ ± 3/2g
17.3 MHz
± 5/2g

c
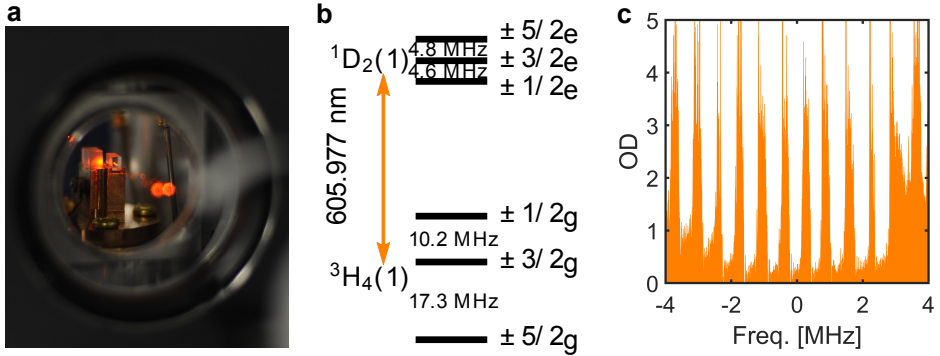
FIGURE 3.10: (a) Picture of the doped crystal sitting in the Montana cryostation (Credit: Kutlu Kutluer). (b) The level scheme for Pr^{3+}:Y_2SiO_5 with the hyperfine splittings given in MHz. (c) an example of the AFC for a storage time of $\tau_{AFC} = 1.6\,\mu s$. This AFC is resonant with the $\pm 1/2_g - \pm 3/2_e$ transition.

laser source used for preparation is based on sum-frequency-generation of 1570 nm and 987 nm in a second PPKTP waveguide.

We use a double pass AOM to first create a 12 MHz wide transparency window (referred to as 'pit') via spectral holeburning the atoms to other hyperfine levels of Pr^{3+}:Y_2SiO_5. We burn ions back into the pit by sweeping the laser 4 MHz centered at +30 MHz with respect to the pit centre. This populates the $\pm 1/2_g$ and $\pm 3/2_g$ ground states within the pit (see fig. 3.10(b) for level diagram), and by then emptying again the $\pm 3/2_g$ ground state via optical pumping, we are left with a 4 MHz wide single class of ions within the $\pm 1/2_g$ ground state [144, 145]. Within this single class, spectral holes at regular Δ intervals are burnt resulting in a 4 MHz wide AFC resonant with the $\pm 1/2_g - \pm 3/2_e$ transition (see fig. 3.10(b)). The burnt ions are then placed into the $\pm 3/2_g$ and $\pm 5/2_g$ ground states. The total preparation time for the memory is around 200 ms.

Finally, the preparation mode is sent at an angle of about $4\,^\circ$ with respect to the input mode, overlapping only on the memory. This allows to spatially filter the strong preparation light away from the single photon detection mode.

3.4.3 Results
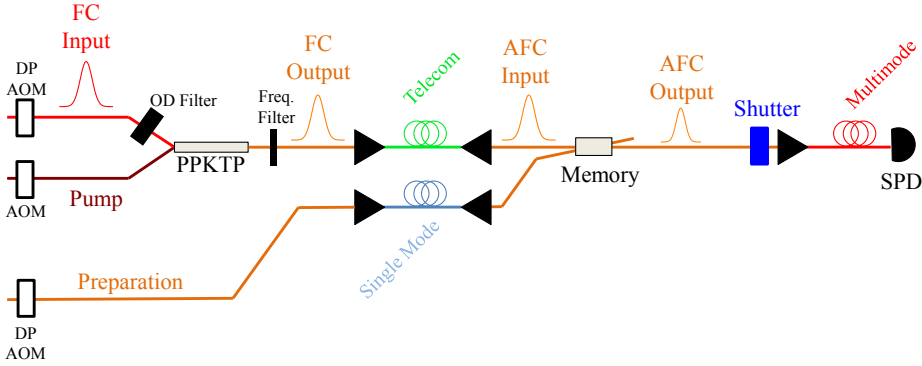
FIGURE 3.11: Experimental set-up. Pulses of 1570 nm light are created with a double pass acousto-optic modulator (DP AOM) and are then reduced to the single-photon-level using a neutral density filter (OD Filter). Both signal and pump at 987 nm are coupled into the periodically-poled potassium titanyl phosphate (PPKTP) nonlinear waveguide producing the 606 nm output. The output mode of the FC is filtered with first a diffraction grating and then an etalon with finesse 6, linewidth 10 GHz. The mode is then coupled to the memory based on the AFC protocol (see text) via a telecom fiber (slightly multimode for 606 nm). The light used to create the AFC passes a DP AOM before being in and out coupled of a single mode optical fiber, giving a total of 2 mW of power before the crystal. The AFC output mode is coupled to a single photon detector via a multimode fiber. A shutter is used to protect the SPD during the preparation period.

We now couple the light to the crystal, with Fig. 3.12 showing the results. At the input of the FC, photon numbers ranging from 0.05 to 2 photons per 140 ns pulse were used and the μ_1 parameter was measured for 3 cases: the frequency converter alone, the photons passing through a 12 MHz transparency window created in the memory crystal and finally the stored and retrieved photons from the memory. For the second case, the light is polarized along the D_1 crystal axis, whereas for the third case the polarization is along the D_2 axis. For all measurements in this section, the pump power is set to 144 mW leading to an QFC device efficiency of $15 \pm 1 \%$.

For the case of the frequency converter alone, where the photons are measured after coupling to the telecom fiber, we measure $\mu_1 = \frac{\mu_{\text{in}}}{\text{SNR}} = 0.37 \pm 0.02$ photons. The integration window taken is $400\,\text{ns}$ which includes the entire pulse.

We then out-couple the light and steer it toward a $12\,\text{MHz}$ transparency window tailored in the inhomogenous absorption line of the $\text{Pr}^{3+}:\text{Y}_2\text{SiO}_5$ crystal and we measure $\mu_1 = 0.23 \pm 0.004$ photons. The signal and noise detection windows here are the same as the previous case. An improvement in the μ_1 is seen, this is due to the absorption of the noise by inhomogenous linewidth of the sample. The etalon placed after the converter (see fig. 3.11) has a linewidth of around $10\,\text{GHz}$ resulting in noise with this bandwidth. With the noise polarized along the D_1 axis we measure a reduction of $33\,\%$ which is consistent with an absorbing line of width $6 - 12\,\text{GHz}$.

Finally, for the case of the stored light we measured $\mu_1 = 1.38 \pm 0.03 \times 10^{-3}$ photons, about a factor of 270 improvement compared to the frequency converter only case. The memory efficiency is measured to be $\eta_{\text{AFC}} = 19.8 \pm 0.1\,\%$. One key feature here is that the echo signal is delayed by a known time of $\tau_{\text{AFC}} = 1.6\,\mu\text{s}$, which allows us to disable the $987\,\text{nm}$ pump of the frequency converter before the echo is re-emitted from the sample. This can be seen clearly in Fig. 3.12(a) where at a time of about $1\,\mu\text{s}$ the pump is disabled resulting in a dramatic drop of noise in the echo temporal window. The pump is disabled for a total time of $5\,\mu\text{s}$ by turning on an AOM (see Fig. 3.11). Most of the pump is then diffracted and is not coupled to the waveguide. The remaining pump in the zero order mode of the AOM can be coupled, this is why the noise does not go down to the dark count level.

Due to the narrowband nature of the memory (about $4\,\text{MHz}$ relative to the $> 5\ \text{GHz}$ noise), the memory itself acts as a filter of the noise storing only a fraction of it. This, in combination with the fact that the pump is gated, thus allows for a 2 orders of magnitude reduction in the μ_1 for the echo.
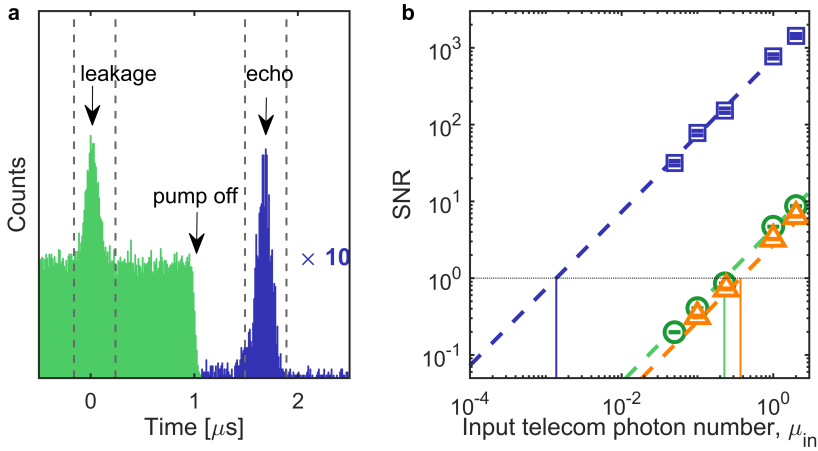
FIGURE 3.12: Signal to noise ratio as a function of the input telecom photon number, μ_{in} for a pump power of 144 mW after the waveguide. The integration window is 400 ns. The red triangles show the results for the FC only, the orange circles show the case of the photons passing through a transparency window and finally the blue squares show the AFC echo. The dashed lines show a linear fit forced to go through zero. The black dotted line represents SNR= 1, with the thin vertical lines showing the μ_1 for each case. Error-bars (smaller than the symbols) represent one standard deviation. Inset: An example of an input (light, orange histogram) and an echo (dark, blue histogram) for $\mu_{\text{in}} = 0.1$ photons per pulse and $\tau = 1.6\,\mu$s. Note the echo histogram is multiplied by 10. The vertical dashed lines indicate the integration window for the signal. A comb is prepared 200 times, with 6000 pulses sent per comb. The bin size is 10.24 ns.

From the echo and the input photon number we can extract the total efficiency of our device (including frequency conversion, all optical loss and storage efficiency), which we measure to be $\eta_{\text{tot}} = 1.55 \pm 0.02\,\%$. From the device efficiency of the converter ($\sim 15\,\%$ at 144 mW pump power), an additional 66 % transmission loss from memory input to the SPD and the AFC efficiency ($\sim 20\,\%$), we have quantitative agreement between using strong and single-photon-level light. In this experiment we have also shown that the signal-to-noise ratio and the total efficiency stay constant up to $5\,\mu$s storage time [117], before decreasing due to the loss of finesse of the comb. In order to increase storage time, spin wave storage [70, 139] could also be implemented.

To conclude, we have demonstrated the storage of up-converted single-photon-level telecom light in a Pr^{3+}:Y_2SiO_5 crystal with storage times of up to $10\,\mu s$. This was the first demonstration of single-photon-level light storage interfaced with frequency up-conversion. We have shown that the stored photon can be retrieved with high signal to noise ratio, despite the high amount of noise generated by the converter device. With this in mind, we view our memory also as a noiseless converter of telecom light to the visible.

Conclusion

In this chapter, I introduced a frequency converter setup, capable of both up and down conversion of single-photon level light between $606\,nm$ and telecom wavelength, with high efficiency and high signal-to-noise ratio detection, possible thanks to strong filtering of the pump-induced noise.

In a first experiment we showed the frequency conversion of memory-compatible single photons. We demonstrated that the non-classical correlations between heralded and heralding photons from a photon pair source are preserved thanks to the high signal to noise ratio conversion. We also highlighted the possibility of using a converter device as a frequency-domain beam splitter. This work opens the route towards connecting different solid-state quantum memory systems emiting in the visible range (e.g. Europium and Praseodymium quantum memories or NV centers) to the telecom C-band.

In a second experiment, we demonstrated that telecom single photon level light can be converted and stored in a visible photonic quantum memory based on Praseodymium doped crystal and finally retrieved in a noiseless time window.

Whereas noiseless conversion is possible in cascaded processes [126], these results show that filtering allows single stage conversion with low noise.

Chapter 4

Non-classical correlations between a spin-wave and a telecom photon

In this chapter we demonstrate non-classical correlation between a frequency converted telecom C-band photon and a spin-wave stored in an atomic ensemble quantum memory. The QM is implemented in a cold ensemble of ^{87}Rb atoms following the DLCZ protocol (see 1.2.2.2). The photons emitted from the ensemble and heralding the spin-waves are converted from 780 nm to 1552 nm by means of a non-linear waveguide. We show ultra-low noise operation of the device enabling a high signal to noise ratio of the converted single photon, leading to a high spin-wave heralding efficiency. This chapter is based on Ref. [115] which was published in Optica. The experiment was done in collaboration with Pau Farrera who was in charge of the cold atomic memory.
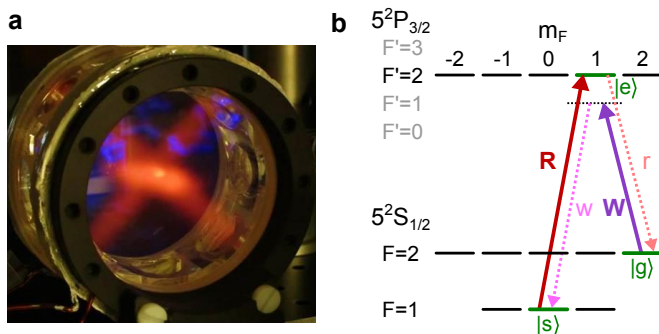
FIGURE 4.1: (a) Picture of the atomic cloud, trapped inside the vaccuum cell. (b) Energy levels and coupling scheme for the DLCZ experiment.

The experimental setup is depicted in Fig. 4.2 and basically consists of two parts – the atomic QM and the quantum frequency conversion device (QFCD). We will first describe the two systems.

4.1 The cold atomic quantum memory

The building and operation of the cold atom QM was not part of my PhD. I nevertheless describe it here (text from Refs. [115, 146]), to help the reader understand the full experiment.

The cold atomic QM consists of a cloud of ^{87}Rb atoms (Fig 4.1), kept in a UHV chamber and cooled via magneto optical trapping (MOT). The cooling and repumping beams are derived from the write and read diode lasers (two external cavity diode lasers, Toptica) which are locked via doppler free absorption spectroscopy to Rubidium reference cells to be resonant with the D_2 line of ^{87}Rb at 780 nm. After passing through acousto optic modulators (AOMs) in double pass configuration, the cooling beam is 20 MHz red-detuned to the $|F = 2\rangle \leftrightarrow |F' = 3\rangle$ transition, and the repumping beam is resonant to the $|F = 1\rangle \leftrightarrow |F' = 2\rangle$ transition. They are combined with a magnetic gradient of 20 G/cm to load $N \approx 10^8$ Rubidium atoms into the MOT. After a 2 ms long optical molasses phase, the temperature of the atoms is about $T \approx 100\,\mu$K. Next, all population is

prepared in the $|g_A\rangle = |5S_{1/2}, F = 2, m_F = 2\rangle$ Zeeman sublevel by applying the repumping light and the σ^+ polarized optical pumping light on the $|F = 2\rangle \rightarrow |F' = 2\rangle$ transition.

To generate the spin-wave inside the atomic cloud, we send write pulses (derived from the write laser and a subsequent AOM) which are $40\,\mathrm{MHz}$ red detuned from the $|g_A\rangle \rightarrow |e_A\rangle = |5P_{3/2}, F = 2, m_F = 1\rangle$ transition and exhibit a duration of $20\,\mathrm{ns}$ (full width half maximum FWHM). The write pulses pass a polarization beam splitter (PBS) and a quarter wave plate to set their polarization to σ^- in the frame of the atoms. The quantization axis is set by a bias magnetic field of $B = 110\,\mathrm{mG}$ along the write/read photon direction. The write pulses generate Raman-scattered write photons, which are emitted on transition $|e_A\rangle \rightarrow |s_A\rangle = |5S_{1/2}, F = 1, m_F = 0\rangle$. A small fraction of the isotropically emitted write photons is collected at an angle of $3.4°$ with respect to the write/read pulse axis. The write photons pass a combination of quarter wave plate, half wave plate, and PBS to couple just the ones with the correct σ^+ polarization into a polarization maintaining (PM) optical fiber. Afterwards the write photons are either sent to the converter device (see next section), either spectrally filtered by a monolithic Fabry-Perot cavity with approx. $50\,\mathrm{MHz}$ linewidth and 24% total transmission (including subsequent fiber couling) before finally being detected by SPD D1 with 41% efficiency and a dark count rate of $130\,\mathrm{Hz}$.

To gain information about the spin-wave, we sent a read pulse ($\tau_R = 35\,\mathrm{ns}$, $P_R = 190\,\mu\mathrm{W}$) resonant to the $|s\rangle \leftrightarrow |e\rangle$ transition to convert the spin-wave back into a single read photon. Due to collective interference of the atoms, the read photon is emitted in a spatial mode given by the phase matching condition $\mathbf{k}_r = \mathbf{k}_R + \mathbf{k}_W - \mathbf{k}_w$, with $\mathbf{k}_{r,R,W,w}$ denoting the respective wave vectors of the single photons and pulses [49]. The read photon is then polarization filtered before being sent through a monolithic Fabry-Perot cavity ($\eta_{cav} \approx 20\%$ total transmission, including cavity transmission and subsequent fiber coupling) for spectral filtering and finally detected in a window of $100\,\mathrm{ns}$ by a silicon SPD (Excelitas SPCM-AQRH-14) with $\eta_{d,780} = 40\%$ efficiency. The retrieval efficiency is defined as the probability
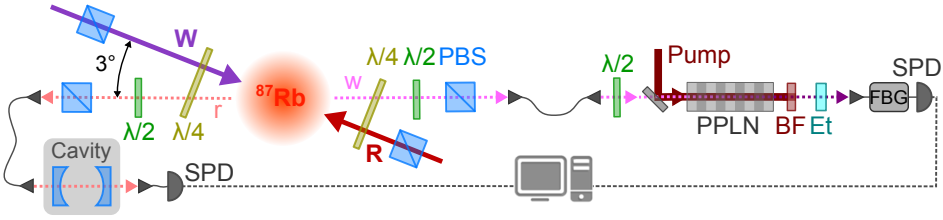
FIGURE 4.2: (a) Experimental setup. Write pulse (W) and Read pulse (R) are sent counter-propagating into the atomic cloud. Write and read photonic modes are denoted by w and r. The QFCD consists of the PPLN waveguide, a bandpass filter (BF), a narrowband etalon (Et), and a fiber bragg grating (FBG).

to map a heralded spin-wave onto a read photon. Its raw value is calculated as $\eta_{ret} = p_{cw,r}/p_{cw}$, where $p_{cw,r}$ is the probability per trial to detect a coincidence between a converted write and a read photon and p_{cw} is the probability per trial to obtain a detection event in the converted write photon detector. The fiber-coupled retrieval efficiency $\eta_{ret}^{fiber} = \eta_{ret}/(\eta_{cav}\eta_{d,780})$ corresponds to the probability of finding a read photon in the optical fiber after the vacuum cell, i.e. corrected for filtering and detector efficiency only.

4.2   The quantum frequency converter

The quantum frequency converter device (QFCD) used to shift the wavelength of the write photons is based on a PPLN waveguide, initially developped by Xavier Fernandez Gonzalvo and Boris Albrecht [113, 125]. The write photon is sent to the QFCD and first overlapped on a dichroic mirror with the spatial mode of the pump laser at 1569 nm which before was spectrally cleaned by two bandpass filters (Semrock NIR1, center wavelength 1570 nm, transmission bandwidth 8.9 nm), leading to an ASE suppression of more than 100 dB at 1552 nm. A combination of lenses ensures optimal focussing and mode matching of the beams into the temperature stabilized

3 cm long buried-PPLN-MgO waveguide (HC Photonics) in which the conversion of the write photon from 780 nm to 1552 nm takes place. Afterwards, the pump radiation is blocked by a combination of two bandpass filters (Semrock NIR01-1550/3-25) each with a transmission bandwidth of 7 nm around 1552 nm and an maximum optical depth of $OD \approx 12$. However, further filtering is required to detect the converted write photon at the single photon level because of noise generated by spontaneous Raman scattering of the pump beam which leads to a broad background around the target wavelength (only 2.1 THz away from the pump frequency). In contrast to former work [113, 125], we apply a two-stage additional filtering consisting of an etalon with a bandwidth of 210 MHz and a free spectral range of 4 GHz and a fiber Bragg grating (FBG) of 2.5 GHz bandwidth. The total extinction ratio of the whole filtering stage for the pump radiation at 1569 nm is > 150 dB (100 dB for the two bandpass filters, 44 dB for the FBG and 11 dB for the etalon). This allowed us to achieve high values of SNRs at low photon number, which is necessary for the quantum frequency conversion of the heralding write single photons. The converted write photons are finally detected by an InGaAs single photon detector (SPD) (ID Quantique ID230) with an detection efficiency of $\eta_{d,1552} = 10\%$ and a dark count rate of 10 Hz.

We measured a clear linear dependence with pump power of the Raman noise. Interestingly no saturation or deviation from the linear behavior due to back-conversion was observed, as in Chapter 3 with SPDC noise. This is yet not explained, but could be due to imperfect filtering, or polarization dependent noise.

The performance of the QFCD can be deduced from Figure 4.3. For characterization of the QFCD, we couple 1.2 mW continuous wave input light at 780 nm to measure the total conversion efficiency and single photon level coherent input pulses of 16 ns duration with a mean photon number per pulse of $\mu_{\text{in}} = 0.16$ to measure the SNR versus the coupled pump power (measured behind the waveguide). The plotted internal efficiency
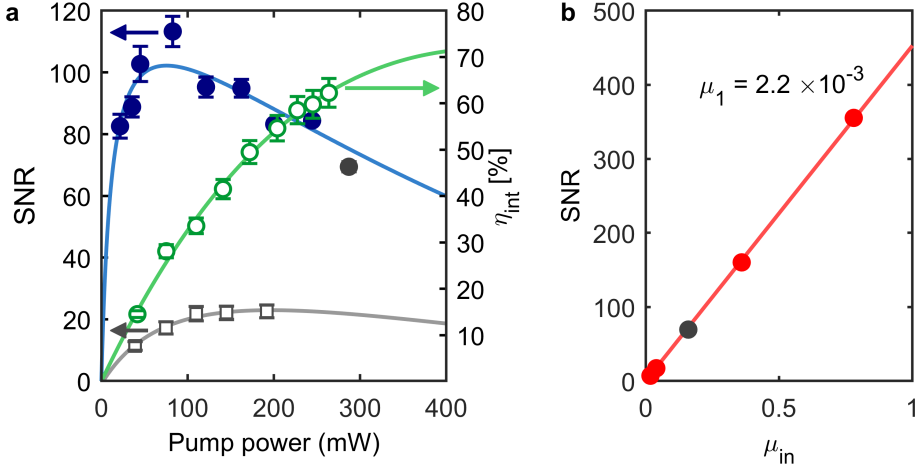
FIGURE 4.3: Signal to noise ratio SNR (blue dots for full filtering, grey squares without etalon, left axis) measured with a mean input photon number per pulse of $\mu_{\mathrm{in}} = 0.16$ and internal efficiency η_{int} of the QFCD (green circles, right axis) measured with classical input light vs. pump power measured after the waveguide. The data are fitted by functions, modeling the expected behavior (solid lines). (b) μ_1 measurement: SNR vs. μ_{in} for a fixed pump power of $P_{\mathrm{pump}} = 287\,\mathrm{mW}$.

η_{int} excludes all optical losses, e.g. due to initial coupling in the waveguide ($\eta_{\mathrm{cpl}} \approx 74\%$), all subsequent filtering stages ($\eta_{\mathrm{filter}} \approx 36\%$), all optical surfaces including one optical isolator ($\eta_{\mathrm{surf}} \approx 70\%$) and the final fiber coupling ($\eta_{\mathrm{fiber}} \approx 75\%$). The data are fitted with the Eq. 2.14 and we retrieve a normalized conversion efficiency of $\eta_n = 61\,\%/\mathrm{W/cm}^2$ and a maximum internal efficiency of $\eta_{\mathrm{int}}^{\mathrm{max}} = 72\%$ which corresponds to a maximum total device efficiency of $\eta_{\mathrm{dev}}^{\mathrm{max}} \approx 10\%$ with $\eta_{\mathrm{dev}} = \eta_{\mathrm{int}}\eta_{\mathrm{loss}}$, with $\eta_{\mathrm{loss}} = 14\%$. The SNR, defined as the background subtracted conversion signal over the background, follows the expected behavior (blue line) showing a drop for low pump powers due to the dark count limitation of our detector ($DC_{1552} = 10\,\mathrm{Hz}$) as well as a decrease for very high pump powers due to the non-linear dependence of η_{int} on P_{pump}. For comparison we also included a trace of the SNR measured without the etalon (grey squares) which shows significantly worse filtering. Fig 4.3(b) shows the SNR depending on the mean input photon number μ_{in} for full filtering (including

the etalon) for a fixed pump power of $P_{\text{pump}} = 287\,\text{mW}$. We observe the expected linear dependence $\text{SNR} = \text{SNR}_{\text{max}} \times \mu_{\text{in}}$ with $\text{SNR}_{\text{max}} = 452$ for a single photon input (i.e. $\mu_{\text{in}} = 1$). This represents a more than fivefold improvement compared to former reported results [113].

4.3 Frequency conversion of write photons

We then combined the QFCD with the cold atomic QM to convert the write photons from $780\,\text{nm}$ to $1552\,\text{nm}$ and investigate the joint properties of the telecom photons and the atomic spin-wave stored in the QM.

To demonstrate that the conversion of the write photon preserves its quantum character, we measured the normalized second-order cross-correlation between the converted write photon and the read photon defined as $g^{(2)}_{cw,r} = p_{cw,r}/(p_{cw}p_r)$. For comparison we also took the cross-correlation $g^{(2)}_{w,r}$ without write photon conversion, for which we replaced the QFCD by a Fabry-Perot filtering cavity with similar characteristics as the one used for the read photons but resonant with the write photons. The obtained data are shown in the Fig. 4.4(a) as blue dots for $g^{(2)}_{cw,r}$ and light blue dots for $g^{(2)}_{w,r}$ vs. the applied power of the write pulse. We observe the highest cross-correlation of $g^{(2)}_{cw,r} \approx 20$ for a write pulse power of $P_W \approx 10\,\mu W$. For higher P_W, $g^{(2)}_{cw,r}$ decreases, as expected for a DLCZ-type QM. For lower values of P_W, $g^{(2)}_{cw,r}$ slightly drops due to noise introduced by the QFCD and the dark counts of the SPDs [147]. This also explains the deviation of $g^{(2)}_{cw,r}$ from $g^{(2)}_{w,r}$ in the low P_W regime. The measured $g^{(2)}_{cw,r}$ in Fig. 4.4(a) are well above the classical limit of 2, assuming thermal statistics for the write and read beams (see below). This shows that we can operate the combined QM-QFC device for a large range of write pulse powers in a highly non-classical regime. The experimental data follow well the expected behavior taking into account the background noise created by the QFCD pump laser (indicated by the blue shaded area) which can be deduced from (see
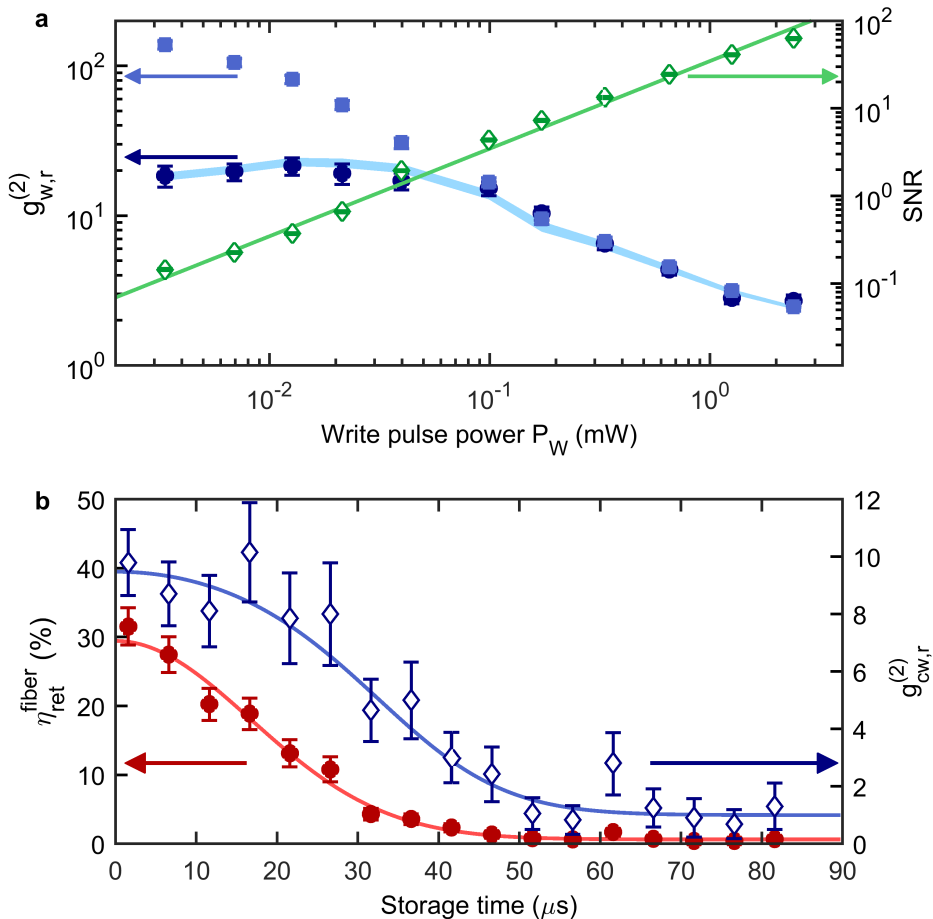
FIGURE 4.4: (a) Normalized cross-correlation of the unconverted write photons (light blue dots, left axis) and the converted ones (blue dots) with the read photons and SNR of the converted write photons (green diamonds, right axis, errorbars smaller than symbol size) vs. peak power of the write pulse. The blue shaded area corresponds to the expected $g_{cw,r}^{(2)}$ as inferred from Eq. (4.1), and the SNR is fitted by a linear regression (green line). (b) Retrieval efficiency (red circles, left axis) and normalized cross-correlation of the converted write photons and read photons (blue empty diamonds, right axis) vs. storage time in the QM. The write and pump powers were fixed at $P_W = 0.18\,\text{mW}$ and $P_{\text{pump}} = 290\,\text{mW}$.

Appendix A)

$$g_{cw,r}^{(2)} = \frac{g_{w,r}^{(2)} + \text{SNR}^{-1}}{1 + \text{SNR}^{-1}}. \tag{4.1}$$

Here, $g_{w,r}^{(2)}$ denotes the measured cross-correlation if the write photon is sent through a filtering cavity (similar to the read photon cavity) instead of the QFCD and SNR is the signal to noise ratio of the converted write photon. $\text{SNR} = (p_{cw} - p_N)/p_N$, where p_N is the probability to have a detection when the write photon is blocked before the QFCD (see Supplementary material of Ref. [115]). The good agreement between the experimental data and the simple model suggests that the noise generated by the QFCD pump beam is the main limiting factor for the value of $g_{cw,r}^{(2)}$.

Moreover, we proved unambigusously the high degree non-classical correlations between the converted write photons and the retrieved read photons by violating the Cauchy-Schwarz inequality for classical light, given by

$$R = \frac{\left(g_{cw,r}^{(2)}\right)^2}{g_{cw,cw}^{(2)} \cdot g_{r,r}^{(2)}} \leq 1 \tag{4.2}$$

where where $g_{cw,cw}^{(2)} = \frac{p_{cw,cw}}{p_{cw}p_{cw}}$ ($g_{r,r}^{(2)} = \frac{p_{r,r}}{p_r p_r}$) denotes the unheralded auto-correlation function of the converted write (read) photons. The measured correlation values for different write powers and the inferred Cauchy-Schwarz parameter R are given in Table 4.1. Even for relatively high write pulse powers we clearly violate equation (4.2). For $P_W = 0.17\,\text{mW}$ we obtain $R = 31$ violating the Cauchy-Schwarz inequality by more than four standard deviations, clearly demonstrating strong non-classical correlations between the converted write photons and the retrieved read photons.

Finally, we investigated the capability of the combined QM-QFC device to preserve the non-classical correlations of the converted write photons and the stored spin-wave depending on the storage time in the QM. The retrieval efficiency η_{ret} (green circles in Fig. 4.4(b)) decreases over storage time due to dephasing of the stored spin-wave mainly induced by thermal atomic motion and to a smaller degree by external spurious magnetic field

TABLE 4.1: Measured values of the coincidence detection probability $p_{cw,r}$, the cross-correlation $g^{(2)}_{cw,r}$ and the unheralded auto-correlations $g^{(2)}_{cw,cw}$ and $g^{(2)}_{r,r}$ of the converted write photons and read photons for different write pulse powers P_W. Errors correspond to ± 1 standard deviation. The Cauchy-Schwarz parameter R is calculated from Eq. (4.2).

P_W [mW]	$p_{cw,r}$ [%]	$g^{(2)}_{cw,r}$	$g^{(2)}_{cw,cw}$	$g^{(2)}_{r,r}$	R
2.39	$4.2 \cdot 10^{-3}$	2.48(6)	2.0(2)	2.16(9)	1.4(2)
0.65	$1.2 \cdot 10^{-3}$	4.49(8)	2.3(3)	2.04(9)	4.4(7)
0.17	$0.3 \cdot 10^{-3}$	9.9(2)	1.6(4)	2.0(1)	31(7)

gradients. The decay can be fitted with a theoretical model introduced in the supplementary material of Ref. [115] (see green line in Fig. 4.4(b)) giving a decay time of $\tau = 23.6 \pm 0.8\,\mu\text{s}$. However, the storage time is not a fundamental limitation here, as it could be increased by orders of magnitude using other techniques [93, 148–151]. The normalized cross-correlation $g^{(2)}_{cw,r}$ between the converted write photons and the retrieved read photons is shown as blue dots in Fig. 4.4(b) for a write pulse power of $P_W = 0.18\,\text{mW}$. We observe the expected decay of $g^{(2)}_{cw,r}$ and fit the data with the above mentioned model, giving a decay time of $\tau = 25.8 \pm 1.2\,\mu\text{s}$ which is consistent with the result obtained when fitting η_{ret}. Fig. 4.4(b) shows that we stay in the non-classical regime ($g^{(2)}_{cw,r} > 2$) up to storage times of about $40\,\mu\text{s}$ which corresponds to a fiber transmission length of approximately $8\,\text{km}$.

Discussion and conclusion

The performance of the QFCD is currently mainly limited by technical issues like coupling efficiencies in the PPLN waveguide and into the final optical fiber as well as transmission efficiencies through the filtering stage and other optical surfaces. However, with the current device conversion efficiency of about $10\,\%$ and typical fiber-absorptions of $0.2\,\text{dB/km}$ for $1552\,\text{nm}$ and $3.5\,\text{dB/km}$ for $780\,\text{nm}$, the unconverted photon travelling in a $780\,\text{nm}$ fiber would experience a higher loss after around $3\,\text{km}$ than a

frequency converted photon travelling in a telecom fiber. Hence, even with this seemingly low conversion efficiency, QFC beats direct transmission already after a few km.

Second, we note that a QFCD converting photons to the telecom C-band with a given device efficiency η_{dev} is equivalent in terms of loss to an additional fiber length of $L = -10/0.2 \cdot \log(\eta_{\text{dev}})$. For the current device efficiency of 10 %, this corresponds to an additional loss of $-10\,\text{dB}$ meaning an equivalent of 50 km extra fiber in each arm of a telecom quantum repeater. A device efficiency of 50 % would correspond to 15 km of additional fiber in each arm.

Finally, we note that to alleviate the requirements for spectral filtering and thus to increase the QFC efficiency, also different conversion strategies with further separated wavelengths could be considered [98]. A larger wavelength separation would decrease the Raman noise or could even suppress it completely. However, to convert the 780 nm photon into the telecom C-band ($1530\,\text{nm} - 1565\,\text{nm}$) where the losses in optical fibers are the lowest, not much flexibility is possible. The Raman noise is present up to $700\,\text{cm}^{-1}$ (21 THz) away from the excitation pump, as measured in [137]. In our case, the frequency separation between the pump at 1569 nm and the target wavelength at 1552 nm is 2.1 THz. Using a pump at the edge of the gain spectrum of Erbium amplifiers, around 1605 nm, the separation in frequency between that pump and the target wavelength at 1517, nm would be 11 THz, which is still inside the Raman noise window. The solution for a noise-free conversion as mentioned in Ref. [98] would indeed be to use a pump at around 2000 nm converting the 780 nm photons to 1280 nm into the telecom O-band (frequency difference of 84 THz). This is an interesting approach, but one would have to deal with other issues such as higher transmission losses in fibers, a more challenging mode matching in the non-linear wave-guide, and the need for more sophisticated technical resources.

In conclusion, we demonstrated highly non-classical correlations between a frequency converted telecom C-band photon and a spin-wave stored in an atomic quantum memory. The photon heralding the spin-wave was converted from 780 nm to 1552 nm using an integrated non-linear waveguide. We showed that by improved optical filtering very high signal to noise ratios (up to $\mathrm{SNR}_{\max} = 452$ for a weak coherent input pulse with in average one photon per pulse) could be achieved. This was the key to obtain high non-classical correlations between the converted write and read photons up to $g_{w,r}^{(2)} \approx 20$ when the QFCD was combined with the QM, as well as high SNRs for the detection of the converted write photon, leading to high spin-wave heralding efficiencies. Moreover, we proved that the quantum character of the converted write photons and read photons are preserved by violating the Cauchy-Schwarz inequality by more than four standard deviations. Finally, we demonstrated that the non-classical correlations between the heralding telecom write photon and the near infrared read photon could be stored in the QM up to $40\,\mu$s. Our experiment shows that quantum frequency conversion based on integrated non-linear waveguide is a viable approach to create quantum correlation between telecom photons and long-lived spin-waves.

Chapter 5

Quantum state transfer between the cold atomic cloud and the solid-state memory

Although significant efforts have been devoted to build hybrid quantum systems e.g. devices combining different quantum systems on a single chip [152], or different species of closely spaced trapped ions [153, 154], interactions between these systems are typically mediated by microwave photons or Coulomb interactions, which are not favorable for long distance quantum communication.

Instead, photonic interconnections between different quantum systems have so far been realized only in very few experiments. Ref. [155] reported the interaction (slow light) in a warm Rubidium cell of a single photon emitted from a quantum dot. In Ref. [156], a similar experiment is reported with single photons emitted from a molecule, interfaced with a hot Sodium ensemble. Refs. [157] and [158] reported the photonic coupling of a quantum dot with a single ion and a solid-state memory, respectively. However

these experiments neither demonstrated quantum state transfer nor interfaced two different long-lived quantum memory (QM) systems, which are both crucial requirements for quantum networks applications. A photonic quantum interconnection between different platforms was demonstrated in Ref. [159], using a single atomic species. The main challenge to efficiently interface two different quantum systems via a photonic link, is to obtain strong light-matter interaction between a single mediating photon and both matter systems, whose atomic transitions can differ significantly in wavelength and linewidth.

In this chapter I will present the photonic connection between the Rubidium cold atomic ensemble and the Praseodymium doped crystal, introduced in the previous chapters, using a quantum frequency conversion interface. In Chapters 3.3 and 4, I showed that non-classical properties of single photons can be preserved through a noisy frequency conversion process to the telecom C-band, under the condition that the converted single photons are retrieved with high enough signal-to-noise ratio. In Chapter 3.4, I showed that telecom light at the single photon level, converted using a noisy device, can be stored in the solid state memory and retrieved with high signal to noise ratio. The conditions seem to be met for the connection of the Rubidium-based cold atomic cloud - emitting non-classical light at 780 nm - with the Praseodymium-doped crystal - able to store single-photon level light at 606 nm - using a noisy frequency conversion interface.

This chapter is based on Ref. [146] and the text is mostly adapted from this reference. This experiment was performed together with Pau Farrera who was in charge of the cold atomic memory and Kutlu Kutluer who was responsible for the solid state memory. In this work I was in charge of the connection between the two systems, including the frequency conversion interface, the frequency stabilization and the data collection. In section 5.1, I will first depict the full experiment, composed of the cold atomic quantum memory, the frequency conversion interface and the solid state quantum memory (introduced previously) and explain how they are adapted for

bandwidth and precise frequency matching. In a second section 5.2, I will test the conversion interface and solid state memory together, showing the conversion and storage in the solid state memory of weak coherent states at 780 nm. In the last part 5.3, I will show that a single collective spin excitation (spin-wave) stored in the cold atomic QM can be optically transferred onto a long-lived collective optical excitation inside the crystal. I will also show that time-bin qubits can be faithfully transfered between the two systems. By transmitting correlated single photons and qubits, we demonstrate quantum correlation preserving and coherent quantum state transfer between the disparate quantum nodes.

5.1 The experiment

The full setup is depicted in Fig. 5.1 ((a) for schematics (b) for full picture)[1]. It is composed of 3 different experiments: the cold atomic memory, the frequency conversion interface and the solid state memory. At site A the cold atomic memory emits a photon at 780 nm. It is then first converted to the telecom C-band and sent to another laboratory, at site B. There, it is converted back to visible at 606 nm and finally stored in the solid state memory.

5.1.1 The cold atomic memory

The Rubidium cold atomic based DLCZ memory used in this experiment is described in chapter 4.1. Contrary to that chapter, we here convert the read photons. To match the acceptance bandwidth of the solid state memory, the read photons must exhibit long temporal waveform. To that end we use the capability of this system of shaping the temporal waveform of the emitted read photon, shown in [115].

---

[1] **Fig 5.1 caption. (a) Schematic setup and relevant level schemes.** At site A a cold cloud of ^{87}Rb atoms is held inside a MOT. Following the DLCZ protocol, non-classically correlated photon pairs are produced by first sending classical write pulses (1) generating a spin-wave inside the atomic cloud heralded by a write photon (2) which is spectrally filtered by a monolithic Fabry-Perot cavity (not shown). Upon a write photon detection at D1, the spin-wave is read-out by sending a classical read pulse (3) generating the read photon (4). QFCD1 consists of a periodically poled lithium niobate (PPLN) crystal with an integrated proton exchange (PE) waveguide continuously pumped by a strong pump laser at 1569 nm. It converts the read photon from 780 nm to 1552 nm (5). The converted photon is then separated from the strong pump light via dielectric band pass filters (not shown) before it is sent via a telecom fiber to site B where QFCD2 (consisting of a PPLN ridge waveguide pumped by strong 994 nm laser radiation) converts it to 606 nm via SFG (6) before the photon is again spectrally filtered by several elements. The Pr^{3+}: Y_2SiO_5 crystal was initially prepared with an AFC (0) using a strong preparation beam at 606 nm, to store the converted read photon (7). After retrieval it is finally detected at D2 (8).

(b) Full Setup Abbreviations: PBS polarizing beam splitter; $\lambda/2$ ($\lambda/4$) half (quarter) wave plate; AOM acousto optic modulator; PC polarization controller; FS fiber switch; DM dichroic mirror; BF band pass filter; Gr diffraction grating; PP anamorphic prism pair; Et etalon; S mechanical shutter.
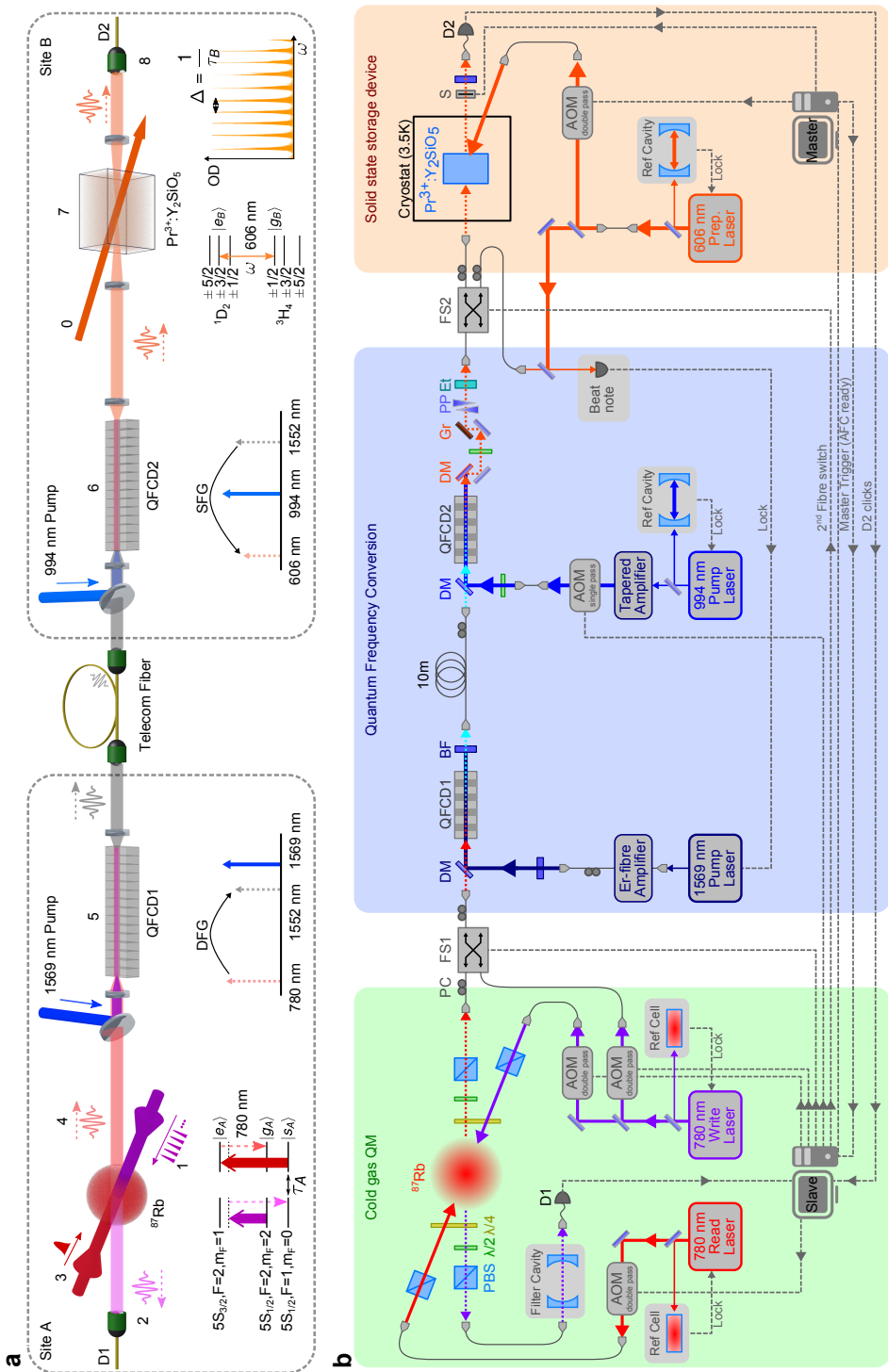
FIGURE 5.1: **Experimental setup:** Description in footnote.
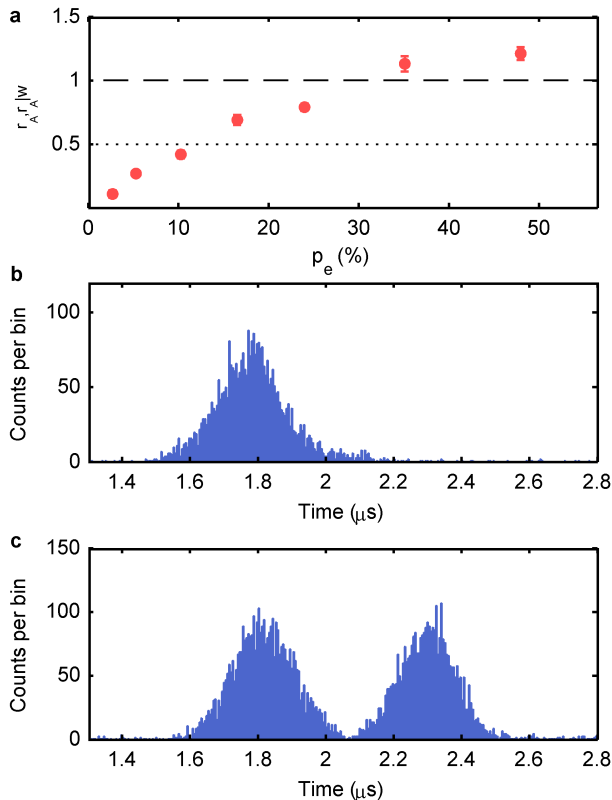
FIGURE 5.2: **Time-bin single read photon.** (a) Anti-bunching parameter of the read photon after the MOT vs p_e. The dashed line indicates the threshold for classical states ($\alpha \geq 1$) and the dotted line for a two-photon Fock state ($\alpha = 0.5$). (b) Conditional histograms of a 200 ns long read photon, (c) time-bin read photon. Both histograms are taken at $p_\text{e} = 5\%$ after the MOT at site A.

The write photons, heralding spin waves in the atomic ensemble are spectrally filtered by a monolithic Fabry-Perot cavity with approx. 50 MHz linewidth before finally being detected by SPD D1.

To read-out the atomic spin-wave, the intensity and temporal wave shape of the read pulses are tailored to efficiently generate read photons with tunable waveform [115]. We are thereby able to create single photons which exhibit sub-natural linewidths in the range of 2 MHz, matching the

spectral requirements of the AFC memory.

Fig 5.2(b) shows an example histogram of a 200 ns long read photon generated at $p_e = 5\%$ in the cold atomic QM detected right after the MOT at site A. Fig. 5.2(a) shows the heralded autocorrelation function $\alpha = g^{(2)}_{r_A, r_A | w}$ for different p_e measured via a Hanbury Brown Twiss setup inserted directly after the MOT. We obtain strongly anti-bunched read photons in the single photon regime ($\alpha < 0.5$) for low $p_e \lesssim 11\%$, in the non-classical regime ($\alpha < 1$) for $p_e \lesssim 25\%$, before surpassing the classical threshold for higher p_e due to multiple spin-wave excitations.

To generate sub-natural linewidth single photons in the cold atomic QM which exhibit a temporally delocalized wave shape suitable for encoding photonic time-bin qubits, we follow the approach also described in [115]. Instead of sending a simple Gaussian shaped read-out pulse to the cold atomic ensemble, we apply an appropriately imbalanced doubly-peaked read-out pulse. The first (early) peak reads out the stored spin-wave with half the retrieval efficiency $\eta^A_{\text{ret}}/2$, and the second (late) peak with full retrieval efficiency η^A_{ret}. This creates the desired time-bin read photon with equal photon detection probabilities in both time-bins ($c_1 = c_2 = \frac{1}{\sqrt{2}}$). By controlling the phase φ between both read-out peaks we can thus create a time-bin photon representing an equatorial qubit state $|\Psi_{\text{eq}}\rangle = \frac{1}{\sqrt{2}}(|e\rangle + e^{i\varphi}|l\rangle)$.

We are thus able to generate two sub-natural linewidths time-bins photons with identical shape as needed for high visibility interference for the coherence preservation and qubit analysis experiments. Fig 5.2(c) shows an example histogram of a time-bin read photon generated at $p_e = 5\%$ in the cold atomic QM detected right after the MOT at site A. Characterization of that photon via a Hanbury Brown Twiss setup after the MOT yields a heralded autocorrelation function of $g^{(2)}_{r_A, r_A | w} = 0.26 \pm 0.02$ confirming the single photon nature of that time-bin read photon.

The read photons then are filtered by a combination of half wave plate and PBS before they are coupled with an efficiency of approximately 60% into

a PM fiber. The fiber is connected to a micro-electro-mechanical single-mode fiber-optic switch (FS1) which directs the read photons or classical lock light to the QFC interface (see subsection 5.1.3).

5.1.2 The solid-state memory

The solid state memory is based on Praseodymium ion-doped crystal. We use the Atomic Frequency Comb (AFC) protocol described in Chapter 3.4.

In this experiment we take adavantage of the intrincic temporal multi-modality of the AFC scheme [18]. We can imprint two simultaneous combs by performing the comb burning operation twice with two different period-icities, Δ_1 and Δ_2, such that the AFC gives access to two different storage times, τ_{B1} and τ_{B2}. Fig 5.3(a,b,c) show the combs structures and their corresponding echos for the different storage times used in the experiment. Fig 5.3(c) shows the simultaneous double comb, leading to two balanced echos after storage of a single input pulse. In this way, the AFC memory can also act as an interferometer, capable of analyzing a time-bin qubit.

To illustrate the capability for the AFC to act as time-bin analyzer, we send double Gaussian pulses separated by 500 ns, mimicking a time-bin qubit. The pulses are stored on two superimposed combs with $2\,\mu$s and $2.5\,\mu$s storage times, such that the late echo of the early bin and the early echo of the late bin overlap in time and interfere. The phase φ of the late pulse is controlled and strongly constructive and destructive interference are observed. In Fig 5.3(d) the red trace shows the interference with $\varphi = 0$ and the green one with $\varphi = \pi$. The data on the left panel shows the area of the interfering peak as a function of the phase φ of the late pulse, yielding a visibility of 95 %. This shows the capability of the solid state memory to store and analyze a time-bin photon, acting as an interferometer.

In order to fully analyze a time-bin qubit, the phase of one arm of the interferometer must be controlled. We exploit the fact that the emitted echo from an AFC acquires a phase shift of $e^{i2\pi\delta/\Delta}$, where δ is the frequency
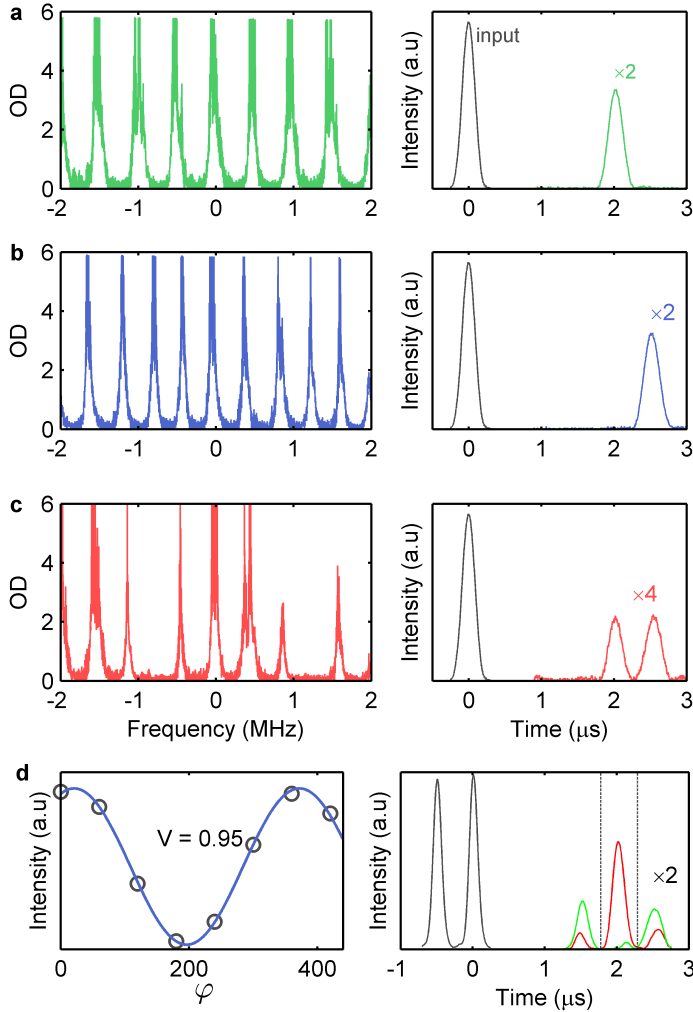
FIGURE 5.3: **AFC storage characterization.** Different absorption spectra of atomic frequency combs with different periodicities Δ are shown on the left side. 200 ns FHWM input pulses derived from the 606 nm preparation laser are sent to the different AFC structures at $0\ \mu s$ and their corresponding echos are shown on the right side. (a) $\Delta = 500\,\text{kHz}$ (b) $\Delta = 400\,\text{kHz}$ (c) double periodicity with $\Delta_1 = 400\,\text{kHz}$ and $\Delta_2 = 500\,\text{kHz}$ leading to a double echo at $2\,\mu s$ and $2.5\,\mu s$. (d) Interference fringe of doubly peaked classical pulses separated by 500 ns stored on two superimposed AFC, as a function of the phase φ of the late pulse.
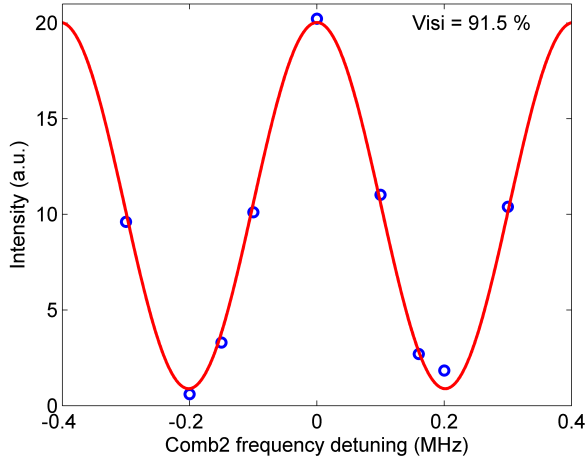
FIGURE 5.4: Interference of doubly peaked classical input pulses on two superimposed AFC combs (with storage times 2 and 2.5 μs) as a function of the center of the second comb with periodicity $\Delta_2 = 400$ KHz.

detuning between the center of the AFC and the input photon, and Δ the periodicity of the comb [70]. Fig. 5.4 shows that we can achieve high visibilities of the interference by shifting the center of one of the two superimposed comb. In this measurement we used classical 606 nm pulses on two superimposed AFCs (with storage times 2 and 2.5 μs) and measured the intensity of the interference as a function of the center of the second comb with periodicity Δ_2=400 kHz. We observed the expected phase shift of 2π for a 400 kHz comb detuning. Hence, shifting δ for one of the two AFCs, allows full control of the interferometer and permits us to set the measurement basis. This will be used for quantum state tomography measurements, shown in the last section of this chapter (5.3.5).

5.1.3   The interface

The interface is based on the cascaded-conversion from 780 to 606 nm, using two frequency converters described in the previous chapters. The first frequency conversion device, converting 780 nm photons to 1552 nm, is described in Chapter 4.2, with the exception that the filtering stage is

here not used (except for bandpass filters blocking the pump light). This leads to a device efficiency of 17% at $290\,\mathrm{mW}$ of coupled pump power. The converted light is sent to the solid state lab via a 10 meters single-mode telecom fiber where the second conversion happens. The second device is described in Chapter 3.1 [2]. It is here used in the up-conversion configuration, from 1552 to 606 nm. The converted light is filtered with a diffraction grating (diffraction efficiency $\eta_{\mathrm{Gr}}^{606\,\mathrm{nm}} = 75\%$) and an etalon ($T_{\mathrm{Et}}^{606\,\mathrm{nm}} = 95\%$, FSR = $60\,\mathrm{GHz}$, finesse $\mathcal{F} = 6$). The device efficiency of this device is $\eta_{\mathrm{dev}}^{\mathrm{QFCD2}} = 15\%$ at $450\,\mathrm{mW}$ of $994\,\mathrm{nm}$ pump power.

As explained in 3.2, a high amount of noise is induced by the pump fields, at the target conversion wavelength. In the first converter the pump at $1570\,\mathrm{nm}$ generates Raman noise at $1552\,\mathrm{nm}$. This noise can then be converted by the second QFC to the target wavelength $606\,\mathrm{nm}$. In the second converter, the $994\,\mathrm{nm}$ pump generates non-phase matched fluorescence at longer wavelengths. This noise at $1552\,\mathrm{nm}$ is phase-matched with the conversion and is back-converted to $606\,\mathrm{nm}$. In order to stop the generation of noise at the target wavelength in this cascaded conversion interface, switching off only the 994 nm pump field is then sufficient. The technique presented in Chapter 3.4, that consists in switching the pump off during storage of the photon in the AFC memory, thus retrieving it in a noiseless time window, can here be applied as well.

---

[2]Initially we planned to use the PPKTP waveguides (AdvR) originally generating 606 nm light for the solid state experiments, from the 1570 and 987 nm pump lasers. To meet the new phase matching conditions we attempted to cool them down to $\approx$2 degrees Celsius in a Nitrogen environment but ended up damaging the chips. We later purchased a PPLN buried-waveguide (HCP) meeting our quasi-phase matching conditions, but this waveguide showed signs of 994 nm pump-induced absorption effects, degrading the conversion efficiency after few hours of operation. We later obtained a new PPKTP waveguide (AdvR), which showed a good internal conversion efficiency from the depletion measurement, but about half of the converted light was lost at the output facet of the chip. This effect was then confirmed with a second chip from the same fabrication batch. We finally acquired a PPLN ridge-waveguide (HC photonics). Although not as long as planned, it did not exhibit transmission losses or absorption effects.

5.1.4   Frequency stabilization

Active stabilization of the involved laser frequencies is necessary to ensure that the converted read photons emitted by the cold atomic QM are resonant to the AFC structure prepared in the crystal. Herefore, the conversion interface is used in two different configurations: a 'QFC' mode where the read photons are converted and sent to the AFC memory, and a 'LOCK' mode where 780 nm continuous wave (CW) light, derived from the write laser, is converted and used to stabilize the frequency of the converted read photons. Two single mode fiber switches (FS1 & FS2) placed before and after the interface are used to swap between the two modes.

The first FS placed before the interface has two inputs and one output and the second one after the interface has one input and two outputs. In the QFC mode, the first FS couples the 780 nm read photons to the frequency converters and the second switch directs the converted 606 nm photons to the solid state storage device. In the LOCK mode, FS1 couples 2 mW of 780 nm CW light to the interface and FS2 sends the converted light to the lock system. An optical beat note between the converted 'LOCK' light and the reference 606 nm laser (used to prepare the AFC structure in the crystal) is measured using a photodiode. The beat note is stabilized at 104 MHz using a frequency comparator (based on a phase locked loop referenced to an internal clock) which feeds back an error signal to the 1569 nm pump laser. Any drift of the involved lasers, inducing a frequency shift of the converted photons is then compensated by acting on the current of the 1569 nm pump laser, thus ensuring that the later converted 606 nm read photons are resonant to the AFC structure in the crystal. Frequency drifts of the lasers also have an impact on the transmitted qubits phase preservation, as discussed in section 5.2.2.

Note that in order to increase the frequency stability of the experiment the linewidth of the 994 nm pump laser diode is reduced, locking its frequency using the Pound Drever Hall technique to an external reference cavity with 690 kHz linewidth and a free spectral range (FSR) of 1 GHz.

The probability for a 780 nm photon entering the first fiber switch FS1 and to exit the second fiber switch FS2, at 606 nm is about 1.2%. This includes all possible losses: conversion efficiencies, waveguide coupling, fiber coupling, optical filtering and transmissions (see Table 5.1).

5.2 Weak coherent states conversion and storage

The QFC interface, the storage in the crystal, and the locking system were first tested and characterized with weak coherent states of light mimicking the single read photons and time-bin qubits obtainable from the cold atomic QM.

5.2.1 Signal to noise ratio and time-bin qubit

Using light from the 780 nm write laser which is sent through another AOM beam line and a set of neutral density filters, we generated attenuated laser pulses of Gaussian shape and 200 ns duration, at the same optical frequency of the read photons from the cold atomic QM. The weak laser pulses are converted through the QFCDs, then stored for $\tau_B = 2.5\,\mu$s in the crystal and eventually retrieved and detected at D2. The histogram for a mean input photon number of 2 at 780 nm is shown in Fig 5.5(a). The leakage of the input photon can be observed at $0\,\mu$s, the strong noise suppression at $1\,\mu$s and the echo at $2.5\,\mu$s. The obtained SNR of the retrieved echo is shown in Fig 5.5(b), as a function of the average input photon number per pulse. The linear fit highlights the performance in term of SNR of our system, showing $\mu_1 = 0.022 \pm 0.001$ – with μ_1 being the minimum number of photons per pulse at the input necessary to achieve a SNR of 1 for the detected echo. The echo then shows a SNR of 14 for an average photon number of 0.3 per pulse at 780 nm - corresponding to the expected number of read photons at the input of the first QFCD per heralded excitation in the cold atomic QM (fiber-coupled DLCZ retrieval efficiency $\eta_A^{\text{ret}} \approx 30\%$).
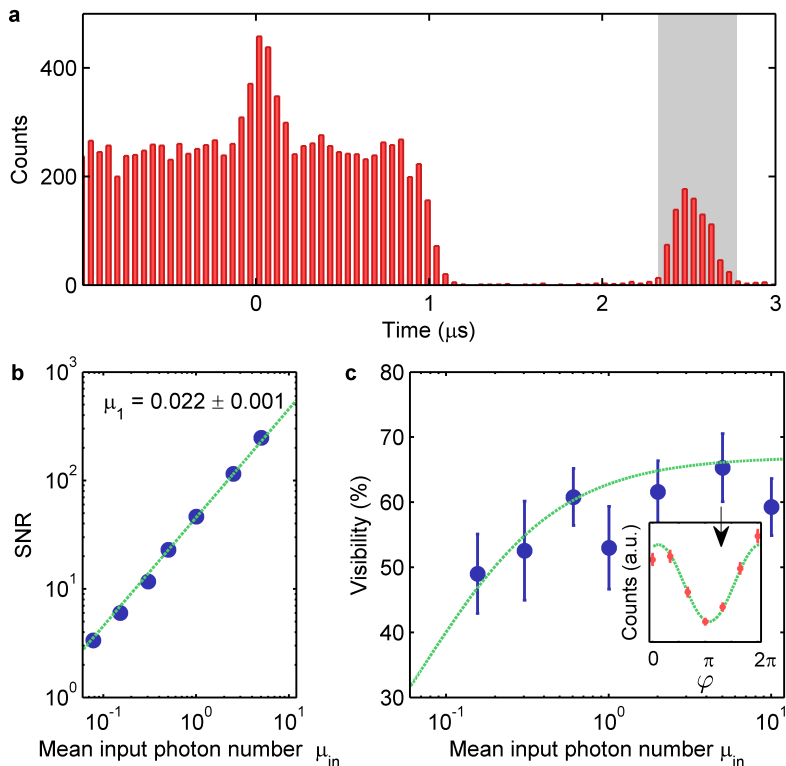
FIGURE 5.5: **Weak coherent state measurements.** (a) Histogram of an echo after $2.5\,\mu$s storage time with an mean input photon number per pulse of 2 at 780 nm. The shaded area shows the integration window. (b) SNR of the echo retrieved from the crystal, if a weak coherent state is frequency converted in the QFCDs and stored in the memory depending on the mean input photon number per pulse μ_{in} before the interface. The green line is a fit with the expected linear behaviour. (c) Visibility of interfering weak coherent time-bin pulses depending on their mean input photon number μ_{in}, after the pulses were frequency converted and stored for $\tau_{B_1} = 2\mu$s and $\tau_{B_2} = 2.5\mu$s in the AFC memory. The green line is the predicted behavior of the visibility taking into account the measured SNR. The inset shows as an example the interference fringe taken at $\mu_{in} \approx 5$.

Next, weak coherent time-bin qubits – attenuated doubly-peaked Gaussian pulses, separated by $500\,\mathrm{ns}$ and with tunable phase difference φ between the early and late bins – were sent through the QFCDs and the solid state storage device. The memory is prepared with two AFCs offering simultaneous storage for $\tau_{B_1} = 2\mu s$ and $\tau_{B_2} = 2.5\mu s$. The early and late bins are overlapped and the interference between the early and late pulses is measured as a function of the relative phase φ. The visibility of this interference is shown in Fig 5.5(c) as a function of the photon number per time-bin qubit μ_{in}. With strong coherent pulses the visibility of this interference is measured to be $V_0 = 67\%$. The decrease of visibility for lower input photon number μ_{in} is due to a decrease in SNR. Taking this effect into account, the visibility becomes [19]

$$V(\mu_{\mathrm{in}}) = V_0 \frac{\mu_{\mathrm{in}}}{\mu_{\mathrm{in}} + 2\beta\mu_1}, \qquad (5.1)$$

where V_0 is the maximum visibility, and β the correcting factor for the reduced efficiency of a double comb AFC compared to a single one. The simple model reproduces well our data, using the SNR measured in Fig 5.5(a) and V_0 measured with strong light pulses (see following section). The visibilities in the single photon regime, presented in the main text correspond here to a regime where $\mu_{in} \approx 0.3$ (mimicking the retrieval efficiency η^A of the atomic memory).

5.2.2 Visibility limitation

Due to our relatively high SNR, the main limitation in our case is most likely given by laser jitter, which stochastically shifts the central frequency of the read photon. A frequency shift δ induces a relative phase $2\pi\delta(\tau_1 - \tau_2)$ between the two interferometer arms, thus reducing the measured visibility over several experimental trials. This can be seen in Fig. 5.6, showing the global phase of the interference fringe using doubly peaked pulses at the input of the solid state memory with two superimposed AFC with storage times of 2 and $2.5\,\mu s$ as a function of the optical frequency detuning of the
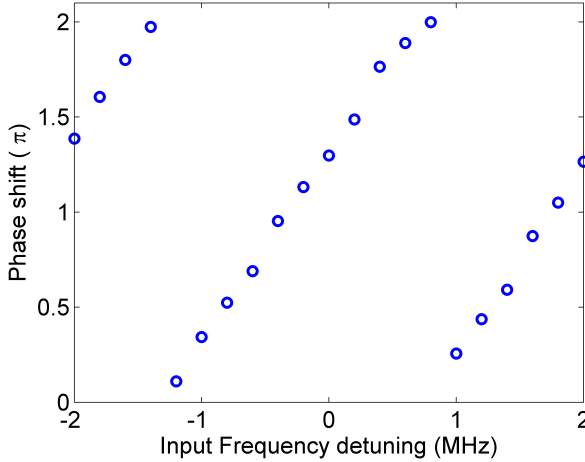
FIGURE 5.6: **Global phase versus input pulse frequency detuning.** Global phase of the interference fringe using classical pulses at the input of the solid state memory with two superimposed AFC with storage times difference of 500 ns as a function of the optical frequency detuning of the input light pulses to the center of the combs.

input light pulses to the center of the combs. We here observe a 2π phase shift for a 2 MHz frequency shift. All the lasers involved in the experiment contribute to this effect — the 780 nm read laser generating the time-bin photon, the two pump lasers of the QFCDs converting the time-bin photon, the 780 nm write laser generating the lock light, and the 606 nm laser preparing the AFCs and acting as the reference for the beat-note lock.

Considering a Gaussian global laser linewidth of σ, the visibility V_0 of the interference between the two time-bins separated by $\Delta\tau$ can be expressed as [160]

$$V_0 = \exp\left(-\frac{(2\pi\sigma\Delta\tau)^2}{2}\right). \tag{5.2}$$

Depending on lasers stability, maximum visibilities V_0, measured with strong coherent pulses, between 65% and 75% have been observed. This corresponds to a global linewidth of the lasers between 570 and 700 kHz FWHM ($\hat{=} 2.35\,\sigma$). Fig 5.7 shows the visibility as a function of the FWHM of the Gaussian linewidth, according to equation (5.2).
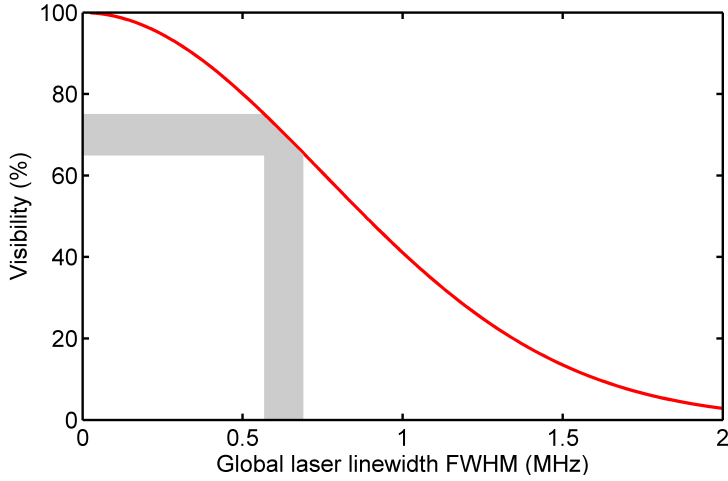
FIGURE 5.7: **Interference visibility.** Visibility as a function of the laser linewidth FWHM $(2.35\,\sigma)$ depicting Eq. 5.2. The shaded area shows the operating range.

When the pump laser at 994 nm was not stabilized on a Fabry-Perot cavity, we observed a significantly lower maximum visibility, around 60% (corresponding to a visibility of around 50 % in the single photon regime). At this time we could measure the stabilized beating signal at 104 MHz (plotted in the inset of Fig 5.8a). The Fourier transform of the beating signal is shown in Fig 5.8a. Although not clearly Gaussian it appears to have a width lower than 1 MHz, in accordance with the above estimation. This spectrum profile was used to simulate the interference fringe between two bins separated by 500 ns, which showed a visibility of 58 % (Fig 5.8b), in agreement with the measured one.

5.3 Quantum state transfer

5.3.1 Time sequence

The timing of our experiment is synchronized on the 1 Hz cycle of the Montana cryostation. Over this one second cycle, the vibrations induced by
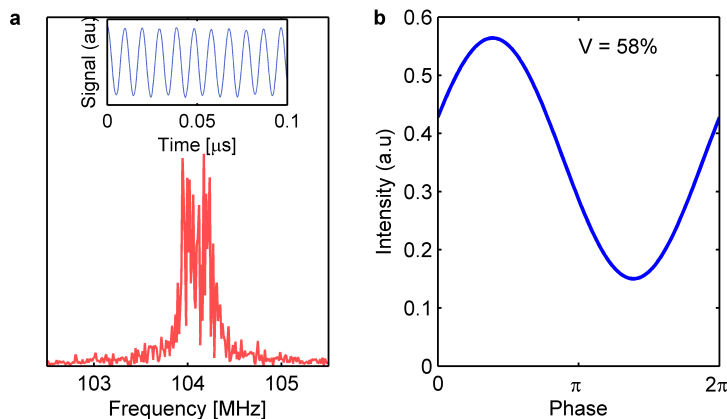
FIGURE 5.8: **Beating spectrum.** (a) Fourier transform of the stabilized beating signal (plotted in the inset) integrated over $400\,\mu s$. (b) Simulated interference fringe for a time-bin difference of 500 ns, taking into account the beating spectrum shown in (a).

the Helium pumping affect the efficiency of the AFC memory. Fig 5.9(a) shows an estimation of the timing of these vibrations windows. We first prepared an AFC structure in the first 200 ms of the cycle, and measured the AFC echo amplitude, for different delays between the end of the AFC preparation and the input pulse (to be stored in the AFC). A full cryostation cycle can be here observed between 1 and 2 seconds in Fig 5.9(a). We observe an exponential decay of the echo amplitude due to the AFC degradation induced by the finite ground state population lifetime. We can also observe dramatic drops of efficiency, caused by the vibrations. We here conclude that after the AFC preparation, we have a window of 300 ms to perform the experiment, where the storage efficiency is high enough.

The time sequence for the experiments is shown in Fig 5.9(b). It starts by preparing the AFC in the crystal for up to 200 ms. Once completed, the Master Computer sends a trigger to the Slave Computer that controls the rest of the experiment (see also Fig 5.1(b)). The main experiment is then performed during the next 290 ms (corresponding to the low vibration time window of the cryostat cycle). The rubidium atoms are cooled at site A inside the MOT for 17 ms while the frequency conversion interface is in the LOCK mode. The interface is then switched to the QFC mode
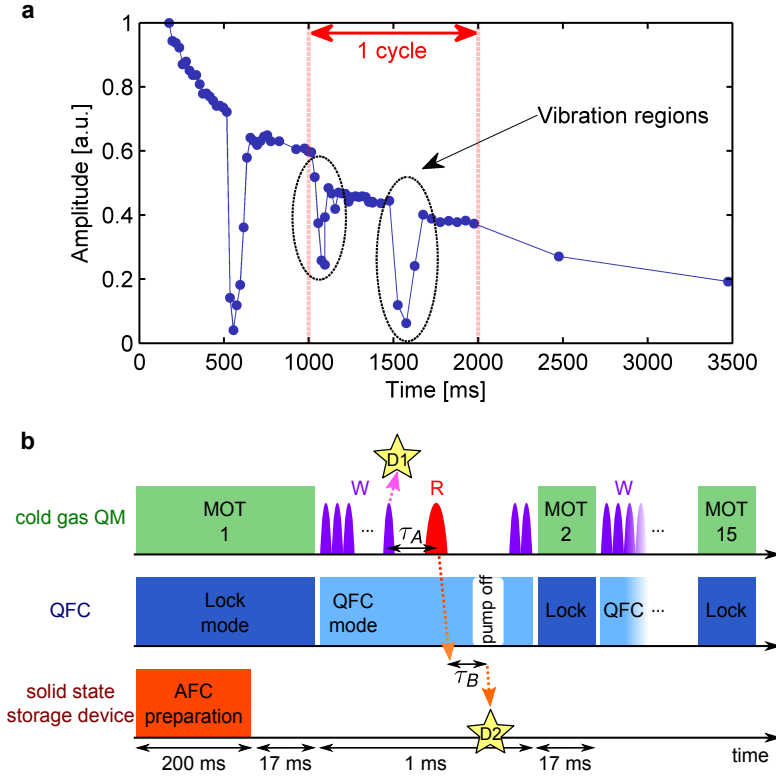
FIGURE 5.9: **a. Cryostation cycle.** Amplitude of the AFC echo as a function of the time delay between the end of the comb preparation and the input pulse. The AFC preparation is triggered every second based on the cycle of the cryostation. The data was measured together with Kutlu Kutluer, and is also shown in his thesis. **b. Experimental time sequence.** First the AFC in the crystal is prepared (bottom row) before the main experiment involving the cold atomic QM (top row) and the conversion interface (center row) starts. Eventual detections of write photons at D1 and converted, stored and restored read photons at D2 are indicated by stars.

and 20 ns long write pulses are sent to the atomic memory. If a write photon is detected at detector D1, the atomic ensemble is read out after a DLCZ storage time τ_A by sending a 340 ns long read pulse. The emitted read photon is converted in the QFCDs and afterwards stored for τ_B in the AFC. During the storage, the 994 nm pump is gated off [117] for 5 μs by the AOM behind the tapered amplifier in order to retrieve the read photon in a noiseless time window. The write/read process lasts for 1 ms

until the Rb atoms are recaptured by a new MOT and the interface is switched to the lock mode for the next 17 ms. After 15 MOT captures and the corresponding write/read trials, the sequence restarts at the next cryostat cycle, preparing a new AFC in the crystal. Accounting for the AFC preparation, the MOT captures and the frequency locking, the duty cycle of the experiment is 1.5 %.

5.3.2 Losses

The probability to obtain an emitted, converted, stored and retrieved photon after the crystal, conditioned on a write photon detection at D1, is approximately 10^{-3}. This includes 1.2% total conversion efficiency (with all optical losses) from 780 nm to 606 nm. The optical losses of the system are listed in Table 5.1.

TABLE 5.1: **System losses.** Detailed optical transmissions and efficiencies of the experiment.

		T, η	
Cold gas	read retrieval (in fiber)	30%	
FS1	transmission	72%	
QFCD1	waveguide coupling	44%	$\eta_{dev} = 17\%$
	conversion	56%	
	filtering & fiber coupling	68%	
QFCD2	waveguide coupling	51%	$\eta_{dev} = 15\%$
	conversion	60%	
	filtering	75%	
	fiber coupling	64%	
FS2	transmission	70%	
Crystal	AFC storage	29%	
	optical transmission	52%	
	detection	45%	
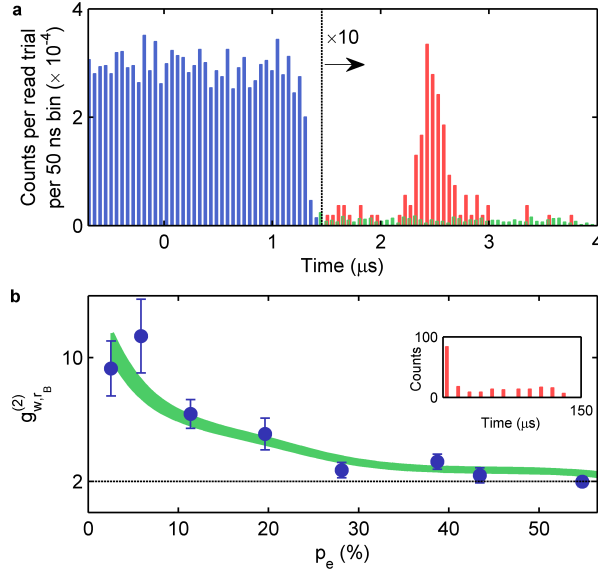
FIGURE 5.10: **Photon conversion and storage.** (a) Time histogram of detections at D2 if the spin-wave (excitation probability $p_e \approx 35\%$) is read-out from the cold atomic Rb QM, the photons are frequency converted in the QFCDs, and stored at $t = 0$ in the crystal. During storage (at $t = 1.2\,\mu s$), the pump of QFCD2 is gated off, and the re-emitted photons are detected as a pronounced AFC echo at $t = 2.5\,\mu s$ (red trace, detected coincidence rate $\sim 90\,/h$ in a $400\,ns$ window around the echo). The green trace corresponds to the noise level, i.e. if no read photon is sent. (b) Normalized cross-correlation $g^{(2)}_{w,r_B}$ between the write photons from the cold atomic QM and the converted, stored and retrieved read photons from the crystal for different p_e. The green area corresponds to the expected $g^{(2)}_{w,r_B}$ as deduced from a similar model as in [113]. The dashed line represents the classical upper bound $g^{(2)}_{w,r_B} \leq 2$. The inset shows a typical $g^{(2)}$ histogram of coincidence detections for several read-out trials separated by the trial period of $\sim 13\,\mu s$ obtained at $p_e \approx 11\%$. Error bars correspond to $\pm 1\,s.d.$ of the photon counting statistics.

5.3.3   Quantum correlation preservation

We now present the photon generation, conversion, and storage involving the whole experimental setup. We first verify that photons emitted by the atomic QM can be successfully converted and stored in the crystal. We create at site A a heralded 200 ns long (FWHM) Gaussian read photons at $p_e \approx 35\%$. Figure 5.10(a) shows the histogram of detection events at D2. The photons arrive at the crystal at $t = 0\,\mu$s, however, no leakage is visible here, as they are buried in the noise generated by the QFCDs. The noise is suppressed at $t = 1.2\,\mu$s by gating off the pump of QFCD2. At $t = 2.5\,\mu$s we detect a pronounced echo signature from the retrieved read photons with a Signal to Noise Ratio SNR $= 17 \pm 2$, mostly limited by the dark counts of D2. The echo shows the same Gaussian temporal shape as the initial read photons with a FWHM of 200 ns.

To investigate the non-classicality of the state transfer, we measured the normalized cross-correlation function $g^{(2)}_{w,r_B}$ of the converted, stored and retrieved photons with the initial write photons for different p_e by comparing coincidences in different storage trials (see Fig. 5.10(b)). At $p_e \approx 5\%$ (with a coincidence rate of approximately 20 counts per hour) we obtain $g^{(2)}_{w,r_B} = 11.4 \pm 2.4$, demonstrating quantum-correlation preserving state-transfer, as the $g^{(2)}_{w,r_B}$ value stays well above the classical bound of $g^{(2)} = 2$ assuming thermal statistics for the write and read photons. Note that the unheralded autocorrelation of the write photon was measured with a value $g^{(2)}_{w,w} \approx 2$, as expected for the two-mode squeezed state generated at the output of the atomic cloud and that the read photon at the output of the atomic cloud showed some bunching with $1 < g^{(2)}_{r_A,r_A} < 2$ (see Tab. 5.2). However the unheralded autocorrelation of the read photons after storage in the solid state memory was not measured due to unrealistic integration times. Alternately we measured it after the frequency conversion interface and found a value $g^{(2)}_{r_{QFC},r_{QFC}} \approx 1$, meaning that the noise added by the QFC has a Poissonian statistics. From these measurements, we conclude that the autocorrelation of the read photons at the output of the crystal

should not have a value higher than 2, which means that $g^{(2)}_{w,r_B} > 2$ is a strong non-classical bound. The preservation of quantum correlations holds true for a broad range of p_e and for storage times τ_B up to $10\,\mu$s. The experimental data in Fig. 5.10(b) match well with the expected behavior (green area) calculated via a simple model taking into account the measured cross-correlation $g^{(2)}_{w,r_A}$ after the MOT and the total SNR of the read photon after conversion and storage [113].

TABLE 5.2: **Unheralded autocorrelation measurements.** Normalized autocorrelation values for the write and read photon fields. $g^{(2)}_{w_A,w_A}$ is measured after the write photons are filtered with the Fabry-Perot cavity. $g^{(2)}_{r_A,r_A}$ is measured at the output of the fiber that collects the read photons from the atomic cloud. $g^{(2)}_{r_{QFCD2},r_{QFCD2}}$ is measured at the output of QFCD2 at site B.

p_e [%]	$g^{(2)}_{w_A,w_A}$	$g^{(2)}_{r_A,r_A}$	$g^{(2)}_{r_{QFCD2},r_{QFCD2}}$
35	1.97(0.10)	1.36(0.05)	1.06(0.05)
10	1.91(0.10)	1.48(0.06)	0.96(0.04)
5	2.13(0.20)	1.35(0.07)	1.00(0.04)

The preservation of non-classical correlations between the write photons – detected at D1 at site A – and the converted, stored and retrieved read photons – detected at D2 at site B – depending on the storage time τ_B in the crystal is also investigated. First, we show in Fig. 5.11(a) the total detection probability at D2 of a converted-stored read photon when a heralding write photon is detected at D1. For small τ_B we obtain total efficiencies up to 0.02% matching the expected range determined by individual optical losses. The decrease of the total efficiency over storage time follows the drop of the AFC memory efficiency due to the change in finesse and effective optical density of the prepared AFC at different τ_B caused by the finite laser linewidth [70]. In Fig. 5.11(b), the normalized cross-correlation $g^{(2)}_{w,r_B}$ between the write and read photons depending on τ_B is shown. We observe a relatively constant $g^{(2)}_{w,r_B} \approx 6$ up to a storage time of $\tau_B \approx 8\,\mu$s until it finally drops below the classical threshold of $g^{(2)}_{w,r} = 2$ at $\tau_B \approx 10\,\mu$s, where the AFC efficiency is low and its echo detection is limited by dark counts of the detector D2. The green area shows
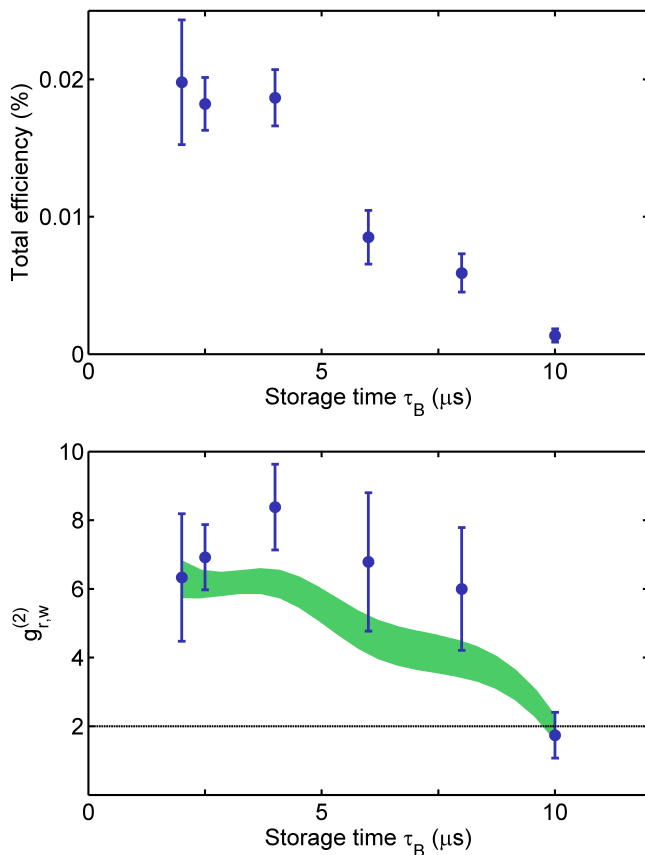
FIGURE 5.11: **Storage efficiency and cross-correlation versus storage time.** Total storage efficiency and normalized cross-correlation function $g^{(2)}_{w,r_B}$ of the initial write photon at site A and the converted, stored and retrieved read photon at site B depending on the storage time τ_B in the crystal, taken at $p_e \approx 10\%$.

the expected correlations taking into account the SNR of the AFC echo, inferred from the AFC efficiencies of Fig. 5.11(a), using the same model as [113].

5.3.4 Coherence preservation

Next, we studied the coherence properties of the state transfer between the two different quantum systems. We use time-bin qubits, which offer
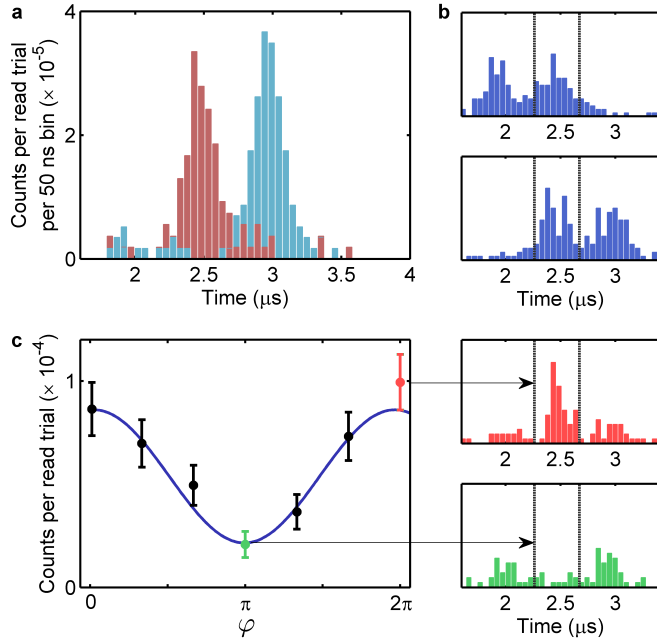
FIGURE 5.12: **Coherence Preservation.** (a) Detected echo of Gaussian shaped read photons which were created ($p_{\mathrm{e}} \approx 35\%$) at either an early time $t = 0$ (red) or at a later time $t = 0.5\,\mu\mathrm{s}$ (blue) at site A and stored for $\tau_B = 2.5\,\mu\mathrm{s}$ at site B. (b) Time-bin photons stored and retrieved after either a short storage time $\tau_{B_1} = 2\,\mu\mathrm{s}$ (top) or a long one $\tau_{B_2} = 2.5\,\mu\mathrm{s}$ (bottom). (c) Time-bin interference fringe, i.e. coincidence counts between initial write photon detections at D1 and detection events during the time-bin-overlap at D2 if a time-bin read photon is stored and retrieved from the crystal prepared with two AFCs. Error bars correspond to $\pm 1\,\mathrm{s.d.}$ of the photon counting statistics. On the right two examples of time histograms between detection events at D1 and D2 are shown for $\varphi = 0°$ (top) and $\varphi = 180°$ (bottom). The $400\,\mathrm{ns}$ coincidence window where the time-bins overlap is indicated by dashed lines.

advantages for long distance quantum communication due to their robustness against external perturbations. If a heralding write photon is detected at D1, we shape the read pulse in a way that the spin-wave stored in the Rb QM is mapped onto a photonic time-bin qubit $|\Psi\rangle_A = c_1|e\rangle + c_2 e^{i\varphi}|l\rangle$, where $|e\rangle$ and $|l\rangle$ represent early and late time-bin, φ is their relative phase, controlled by the phase of the second read pulse, and $c_1^2 + c_2^2 = 1$. To store the photonic time-bin qubit, we take advantage of the intrinsic temporal multimodality of the AFC scheme [18].

95

Figure 5.12(a) shows the time histogram of detection events at D2 of the early and late time-bins (created at $p_e \approx 35\%$) sent through the QFCDs, and stored and retrieved from the crystal prepared with a single AFC of $\tau_B = 2.5\,\mu s$ storage time. The two echoes represent the polar states of a time-bin qubit and exhibit an average SNR above 19 ± 2. If a delocalized time-bin photon $(c_1 = c_2 = \frac{1}{\sqrt{2}})$ is created in the Rb QM, converted in the QFCDs and stored in the crystal for either $\tau_{B_1} = 2\,\mu s$ or $\tau_{B_2} = 2.5\,\mu s$, we detect the histograms shown in Fig. 5.12(b). In order to analyze the qubit, we use the crystal as an interferometer by preparing two overlapped AFCs with storage times τ_{B_1} and τ_{B_2} ($\eta^B = 10\%$ each) [18]. In that case, we obtain the histograms shown in the right panels of Fig. 5.12(c). These two histograms were recorded with a phase shift of $\varphi = 0°$ (top) and $\varphi = 180°$ (bottom) between the early and late time-bin. Strong interference between the two temporal modes can be seen in the central region where the time-bins overlap. Measuring the coincidences in that time window vs. φ gives the interference fringe depicted in Fig. 5.12(c) with a fitted visibility of $V = 60 \pm 9.9\%$, confirming the high degree of coherence preservation between the two disparate quantum systems.

5.3.5 Time-bin Qubit transfer

Finally, to demonstrate qubit transfer between the cold atomic cloud and the crystal via telecom photons, we decreased p_e to 5% generating true single time-bin read photons at site A with an anti-bunching parameter of $\alpha = 0.26 \pm 0.02$ (cf. Fig. 5.2(a)). Following the same approach as above, we show in Fig. 5.13(a) that with converted and stored single time-bin photons, we obtain interference between overlapping bins with visibilities around 70%. Moreover, we show that, by changing the central frequency of the second AFC by $200\,kHz$, the phase of the interference fringe can be shifted by $180°$ verifying the intrinsic phase analyzing capabilities of the AFC. This capability permits the measurement of time-bin qubits in different bases and hence a full analysis of the stored qubits by quantum state
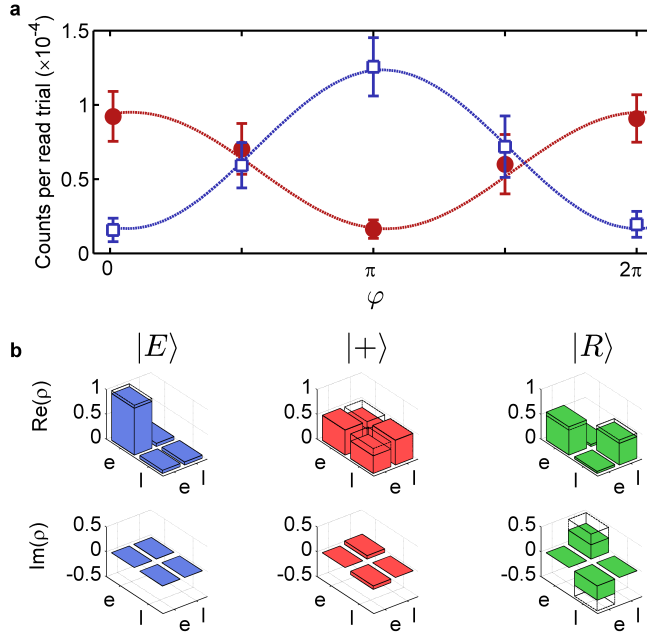
FIGURE 5.13: **Single photon qubit transfer.** (a) Interference fringes from a single time-bin read photon $|\Psi_{\text{eq}}\rangle = \frac{1}{\sqrt{2}}(|e\rangle + e^{i\varphi}|l\rangle)$ generated at site A ($p_e \approx 5\%$ corresponding to $\alpha = 0.26$) if the second AFC is prepared with zero detuning (red dots, $V = 70 \pm 6\%$) or shifted by $200\,\text{kHz}$ (blue open squares, $V = 76 \pm 3\%$). Error bars correspond to $\pm 1\,\text{s.d.}$ of the photon counting statistics. (b) Real and imaginary parts of the reconstructed density matrices measured after the crystal at site B if the qubits $|E\rangle$, $|+\rangle$, $|R\rangle$ are generated at site A, converted in the QFCDs and stored at B. Open boxes indicate the target state.

tomography. Figure 5.13(b) shows the reconstructed density matrices ρ of the retrieved states after the crystal at site B when three orthogonal time-bin qubits ($|E\rangle = |e\rangle$, $|+\rangle = 1/\sqrt{2}(|e\rangle + |l\rangle)$, $|R\rangle = 1/\sqrt{2}(|e\rangle + i|l\rangle)$) are generated in the cold atomic QM at site A, afterwards converted in the QFCDs, and stored at site B. The state reconstruction is based on maximum likelihood estimation. The qubit fidelity conditioned on a successful detection of the photon after the retrieval from the crystal (conditional fidelity) is calculated as $\mathcal{F}^c_{|\psi\rangle} = \langle \psi | \rho | \psi \rangle$ with $|\psi\rangle$ denoting the target state. From Fig. 5.13(b) it is evident that we obtain a high overlap between the reconstructed qubits and the target states with conditional fidelities of $\mathcal{F}^c_{|+\rangle} = 85.4 \pm 6.6\%$, $\mathcal{F}^c_{|R\rangle} = 78.2 \pm 6.9\%$, and $\mathcal{F}^c_{|E\rangle} = 93.8 \pm 2.8\%$, where

the errors were estimated via Monte Carlo simulations taking into account the uncertainty of the photon counting statistics. Despite the low total efficiency of the state transfer we demonstrate an average conditional fidelity of $\mathcal{F}^c = 85.8 \pm 3.3\%$ for the generated and transferred qubit which is consistent with results inferred at higher p_e and surpasses the classical threshold of 66.7% [61] by more than 5 standard deviations.

The fidelity of the polar states is limited by the SNR of the detected photons: $\mathcal{F}_\mathrm{pol} \approx \frac{\mathrm{SNR}+1}{\mathrm{SNR}+2}$. The fidelity of the equatorial states is mainly limited by the visibility of the interference between early and late time-bins: $\mathcal{F}_\mathrm{eq} \approx (1 + V)/2$. The visibility V depends on background noise and the overall frequency jitter of the lasers involved in the experiment (as shown in the previous section 5.2.2).

Conclusion

In this chapter, I showed a proof of principle of quantum communication between heterogeneous quantum nodes, opening prospects for combining quantum nodes with different capabilities. Using the systems introduced in the previous chapters, we built an interface capable of connecting the cold atomic ensemble and the solid state memory. We proved it in two different ways: we first demonstrated that quantum correlations between a photon and a single collective spin excitation in the cold atomic ensemble can be transferred onto the solid-state system. We also showed that single-photon time-bin qubits generated in the cold atomic ensemble can be converted, stored and retrieved from the crystal with a conditional qubit fidelity of more than 85%.

Discussion and perspectives

For potential applications in hybrid quantum networks, the transfer efficiency (currently 10^{-3}) should be greatly increased. Note that the largest

part of the inefficiency is due to technical optical loss in the various elements ($\eta_{loss} = 0.04$). This could be significantly improved, using e.g. fiber pigtailed waveguide converters. The combined quantum memory efficiency ($\eta_{QM} = 0.09$) could also be largely increased with state of the art techniques [63, 161]. Increased efficiencies would also enable spin-wave storage in the crystal, leading to on-demand read-out and longer storage times [139]. While all efficiencies could be in principle pushed towards unity, an interesting direction to alleviate optical losses would be to implement a non-destructive detection of the time-bin qubit with the AFC, as recently proposed in ref. [162]. The duty cycle of the experiment (and hence the total count rate) could also be greatly enhanced, e.g. by using a dipole trap in the cold atomic cloud, and by reducing vibrations in the cryostat, e.g. using damping springs.

In this experiment we have been using short storage times in order to maximize the efficiency and the strong quantum correlations. As shown in Chapter 4, we have measured storage times of a spin wave created in the cold atomic cloud up to $\approx 50\,\mu$s. Here the storage time is mainly limited by the spin wave dephasing induced by the atomic motion as well as spurious magnetic field gradient. Much longer storage times are possible using state of the art techniques like optical lattices [63, 93]. Concerning the solid state memory, the storage time with the two-level AFC is limited to several microseconds (up to $15\,\mu$s has been observed in our lab [163], $50\,\mu$s in Europium doped crystal [164]). At larger times the echo efficiency is strongly affected by the loss of comb finesse due to the finite linewidth of the preparation laser (as the teeths of the comb get closer to each other). The 3-level AFC protocol (spin wave storage), on top of enabling on-demand storage as discussed above, gives access to much longer storage times by converting the optical coherence into a long-lived spin coherence. However this protocol generally adds noise to the retrieved echo, induced by the strong control pulses necessary for the population transfer [139], and very long storage times using advanced spin rephasing techniques is still a challenge at the single photon level [62, 165]. In our

lab, in order to implement spin-wave storage of the converted single photon emitted by the atomic ensemble and achieve a signal to noise greater than 1 after the retrieval, we estimate that the total conversion efficiency should be increased by one order of magnitude. The mean photon number at the input of the memory would then be equivalent to the μ_1 of ≈ 0.035 measured in our system for $11\,\mu$s spin-wave storage (see Dr. Kutlu Kutluer's thesis [163]).

In the experimental setup a 10 meters telecom fiber was used to connect the two QFC devices. The low transmission losses of a telecom fiber ($\approx 0.2\,$dB/km) opens up the possibility to increase the quantum channel length. In the current state of our experiment the noise level per trial in a 400 ns detection window was measured to be $\approx 8\times10^{-6}$ and photon detected in the same window per trial $\approx 1.5\times10^{-4}$ leading to a SNR ≈ 18. In order to observe non-classical correlations, we can assume that a SNR>1 is needed. We could therefore afford a 12 dB transmission loss in between the two experiments, corresponding to 60 km of fiber. However here a large proportion of the observed noise comes from the dark counts of the APD, which could be replaced with superconducting nano-wires detectors with lower dark counts level, permitting a much longer channel length.

A next milestone would be to demonstrate entanglement between disparate systems. In our experiment, this could be done by converting and storing in the solid state memory, the write photon, heralding a spin wave in the cold atomic ensemble. Entanglement between the two memories could be then proved measuring correlations between the read out spin wave (read photon) in the cold atomic ensemble and the retrieved write photon after being mapped onto a single collective excitation in the crystal. In the case of time-bin qubit encoding, two interferometers must be used. For the converted and stored photon, the AFC memory can act as one as shown in this chapter. For the read photon one need to build a stable 110 meters long fiber-interferometer (as the separation between the time bins must be at least 500 ns as required by the AFC memory acceptance bandwidth). The stability of these interferometers is key to showing high

interference visibilities. Towards this goal, Pau Farrera et al. [21] showed time-bin entanglement between a spin wave and single photon at 780 nm, with time-bin separation of 170 ns using two stabilized fiber interferometers of 40 meters.

The tunability of the frequency conversion processes also shows that our technique could be extended to connect other physical platforms, e.g. single ions or NV centers. Moreover, it gives a perspective on how the distance between nodes can be extended by back- and forth-conversion of photonic qubits into the telecom C-band.

Chapter 6

Conclusion

In this conclusion I will first summarize the content of this work, listing the obtained results and advancements in the chronological order. I will finally introduce the future directions based on the different aspects of the thesis.

6.1   Summary of the thesis

The main result of the thesis is the quantum connection between the cold Rubidium ensemble and the Praseodymium-doped crystal. It implied building a quantum frequency conversion interface that bridges the wavelength gap between the two quantum memories.

We started by developing a quantum frequency up-conversion interface from 1570 nm to 606 nm. This was implemented using a PPKTP waveguide and a pump field at 987 nm. The device could reach 21 % conversion efficiency and a μ_1 of 0.37, thanks to the proper filtering applied on the parasitic pump-induced noise. This device was then used to show the conversion of C-band weak coherent states followed by storage in the ion-doped crystal using the 2-level AFC protocol. The photons were retrieved

in a noise-free window, with a signal-to-noise ratio 2 order of magnitude higher than before storage. This experiment is reported in Ref. [117] and explained in Chapter 3.4.

As a second contribution, we improved the frequency down-conversion setup from 780 nm to 1552 , initially built by Xavier Fernandez Gonzalvo. The conversion efficiency was increased and the filtering narrowed. Following the work of Boris Albrecht [113] and in collaboration with Pau Farrera, the device was used to convert write photons emitted by the Rubidium ensemble to the C-band wavelengths. We could demonstrate non-classical correlations between a telecom photon and a spin-wave stored in the ensemble. This is reported in Ref. [115] and explained in Chapter 4.

Meanwhile we started to work on the full conversion interface. This implies using the down-converter from 780 nm to 1552 nm and to modify the up-conversion device to now shift the photons wavelengths from 1552 nm to 606 nm, using a pump at 994 nm. The PPLN based-converter we used is fully described in Chapter. 3, and exhibits a device conversion efficiency from 1552 nm to 606 nm of 15 %. The full interface is also composed of two fiber switches, that permit to swap between the conversion of single photons and the one of classical light for laser locking purposes. A Pound-Drever-Hall stabilization was also implemented for the 994 nm pump. Finally the full interface could reach a total conversion efficiency of 1 % and a frequency stability of the converted photons of 600 kHz. With this interface we performed the main experiment of the thesis, which is the quantum state transfer between the cold atomic cloud and the crystal: we showed that a read photon emitted from the atomic ensemble is converted, stored in the crystal and retrieved with high signal-to-noise ratio. We showed that this photon conserves its non-classical correlations with its twin write photon, which means that a single collective excitation stored in the atomic cloud is transferred to the ionic ensemble in the crystal by mean of a single telecom C-band photon. We also showed that time-bin qubits can be transferred with a conditional fidelity of 85 % between the two memories. These results are reported in Ref. [146] and in Chapter 5 of this thesis.

Finally we used the same conversion device to now convert photons from 606 nm to 1552 . Several quantum nodes emit is the visible range around 600 nm [35, 165–167] where fiber losses are important. The quantum frequency conversion from these wavelengths to the C-band was never reported, mainly because of noise processes induced. We started with the characterization of the noise and showed that heralded single photons emitted from a photon pair source preserve their non-classical properties through the conversion process. This is a step towards connecting more quantum nodes to the telecommunication band. This work is reported in Ref. [132] and described in Chapter 3.3. A similar experiment, showing the quantum frequency conversion of NV center photons was also reported in Ref. [122].

6.2   Future directions

With the motivation of having entanglement between a matter qubit and a flying qubit at the telecommunication wavelength, several experiments can be pursued. The frequency conversion of write photons emitted by the cold atomic memory can be followed by showing the entanglement between a spin-wave and a photonic qubit at the telecommunication wavelength. We could use the same approach as the recent work done by Pau Farrera [21]. This implies using time-bin qubits and building a ≈ 50 meters long telecom fiber interferometer to analyze the qubits after conversion. Similar experiments were reported recently in which polarization insensitive quantum frequency conversion were developed to demonstrate entanglement between a Rubidium ensemble [116] or a trapped-ion [118] and a telecom photon.

In the same spirit, the conversion from 606 nm to the C-band wavelength can be used to pursue the work of Kutlu Kutluer, who showed non-classical correlations between two photons emitted from the Praseodymium-doped crystal, in a similar manner as the DLCZ protocol. It uses the creation of

heralded single collective excitation in an AFC absorption structure that can later be mapped into a photonic qubit. Recently he demonstrated non-classical correlations [166] and entanglement between write and read photons.

The connection between the two heterogeneous systems opens many more possibilities. Using the same approach as Ref. [21], one could show the entanglement between the disparate memories. In that case the write photon must be converted instead on the heralded read photon. This entanglement creation would not be heralded though but it could be solved using heralded absorption techniques as recently reported [162]. One could also use the DLCZ-AFC protocol for the Praseodymium memory. The two memories would then act as emissive systems and entanglement swapping could be perform at an intermediate location using quantum frequency conversion to match the photons wavelengths or using the frequency-domain beam splitter technique. More importantly, we see this experiment as a new platform and opens the route of implementing connections between more complementary platforms. One promising connection would be to connect processing capabilities, such as single ions, with long lived and multiplexed storage devices like rare-earth crystals.

Appendix A

Theoretical model for the second-order cross correlation function

As mentioned in the main text, the second order cross-correlation function between the frequency converted write photons and the read photons, is related to the photon detection probabilities as $g_{cw,r}^{(2)} = p_{cw,r}/(p_{cw}p_r)$. During the frequency conversion process, the write photons experience two kinds of imperfections: the first one is imperfect transmission and the second one is that they are mixed with noise photons (coming mainly from residual pump light and detector dark counts). Considering these two effects, we can rewrite the photon detection probabilities as $p_{cw} = \eta_{\text{QFC}} p_w + p_N$ and $p_{cw,r} = \eta_{\text{QFC}} p_{w,r} + p_N p_r$. In these expressions η_{QFC} is the total efficiency of the quantum frequency conversion device (QFCD), p_w is the probability that a write photon arrives at the input of the QFCD and p_N is the probability to detect a noise photon. These effects can be included in the expression of the cross-correlation function.

$$g_{cw,r}^{(2)} = \frac{\eta_{\mathrm{QFC}}p_{w,r} + p_N p_r}{(\eta_{\mathrm{QFC}}p_w + p_N)p_r} = \frac{\frac{p_{w,r}}{p_w p_r} + \frac{p_N}{\eta_{\mathrm{QFC}}p_w}}{1 + \frac{p_N}{\eta_{\mathrm{QFC}}p_w}} \tag{A.1}$$

From the previous expression we can identify two terms. The first one is the cross-correlation of the fields without any frequency conversion $g_{w,r}^{(2)} = p_{w,r}/(p_w p_r)$ and the other one is the signal-to-noise-ration of the frequency converted photons $\mathrm{SNR} = (p_{cw} - p_N)/p_N = \eta_{\mathrm{QFC}}p_w/p_N$. Introducing this terms in eq. (A.1) leads to the expression of eq. (1) from the main text

$$g_{cw,r}^{(2)} = \frac{g_{w,r}^{(2)} + \mathrm{SNR}^{-1}}{1 + \mathrm{SNR}^{-1}} \tag{A.2}$$

Bibliography

[1] Michael A. Nielsen and Isaac L. Chuang. *Quantum computation and quantum information*. Cambridge University Press, 2010.

[2] Richard P Feynman. Quantum Mechanical Computers. *Optics News*, 11(2):11–20, 1985.

[3] Maciej Lewenstein, Anna Sanpera, and Verònica Ahufinger. *Ultra-cold Atoms in Optical Lattices*. Oxford University Press, mar 2012.

[4] H J Kimble. The quantum internet. *Nature*, 453(7198):1023–1030, jun 2008.

[5] Charles H Bennett and Gilles Brassard. Quantum Cryptography: Public Key Distribution, and Coin-Tossing, 1984.

[6] J. I. Cirac, A. K. Ekert, S. F. Huelga, and C. Macchiavello. Distributed quantum computation over noisy channels. *Physical Review A*, 59(6):4249–4254, jun 1999.

[7] Vittorio Giovannetti, Seth Lloyd, and Lorenzo Maccone. Quantum Enhanced Measurement: Beating the Standard Quantum Limit. *Science*, 306(November):1330–6, 2004.

[8] Benjamin Schumacher. Quantum coding. *Physical Review A*, 51(4):2738–2747, 1995.

[9] Brynle Barrett, Laura Antoni-Micollier, Laure Chichet, Baptiste Battelier, Thomas Lévèque, Arnaud Landragin, and Philippe

Bouyer. Dual matter-wave inertial sensors in weightlessness. *Nature Communications*, 7:13786, dec 2016.

[10] J. Brendel, N. Gisin, W. Tittel, and H. Zbinden. Pulsed Energy-Time Entangled Twin-Photon Source for Quantum Communication. *Physical Review Letters*, 82(12):2594–2597, mar 1999.

[11] Ivan Marcikic, Hugues de Riedmatten, Wolfgang Tittel, Valerio Scarani, Hugo Zbinden, and Nicolas Gisin. Time-bin entangled qubits for quantum communication created by femtosecond pulses. *Physical Review A*, 66(6):062308, dec 2002.

[12] H. Zbinden* & N. Gisin* I. Marcikic*†, H. de Riedmatten*†, W. Tittel*‡. Long-distance teleportation of qubits at telecommunication wavelengths. *Nature*, 421(January):509–513, 2003.

[13] Qi Chao Sun, Ya Li Mao, Yang Fan Jiang, Qi Zhao, Si Jing Chen, Wei Zhang, Wei Jun Zhang, Xiao Jiang, Teng Yun Chen, Li Xing You, Li Li, Yi Dong Huang, Xian Feng Chen, Zhen Wang, Xiongfeng Ma, Qiang Zhang, and Jian Wei Pan. Entanglement swapping with independent sources over an optical-fiber network. *Physical Review A*, 95(3):1–6, 2017.

[14] Raju Valivarthi, Marcelli Grimau Puigibert, Qiang Zhou, Gabriel H. Aguilar, Varun B. Verma, Francesco Marsili, Matthew D. Shaw, Sae Woo Nam, Daniel Oblak, and Wolfgang Tittel. Quantum teleportation across a metropolitan fibre network. *Nature Photonics*, 10(10):676–680, 2016.

[15] I. Marcikic, H. De Riedmatten, W. Tittel, H. Zbinden, M. Legré, and N. Gisin. Distribution of time-bin entangled qubits over 50 km of optical fiber. *Physical Review Letters*, 93(18):1–4, 2004.

[16] Hugues de Riedmatten, Ivan Marcikic, Hugo Zbinden, and Nicolas Gisin. Creating high dimensional time-bin entanglement using mode-locked lasers. *Quant. Inf. Comp.*, 2:425, apr 2002.

[17] Hugues de Riedmatten, Ivan Marcikic, Valerio Scarani, Wolfgang Tittel, Hugo Zbinden, and Nicolas Gisin. Tailoring photonic entanglement in high-dimensional Hilbert spaces. *Physical Review A - Atomic, Molecular, and Optical Physics*, 69(5 A):4–7, 2004.

[18] Hugues de Riedmatten, Mikael Afzelius, Matthias U Staudt, Christoph Simon, and Nicolas Gisin. A solid-state light-matter interface at the single-photon level. *Nature*, 456(7223):773–777, 2008.

[19] Mustafa Gündoğan, Patrick M Ledingham, Kutlu Kutluer, Margherita Mazzera, and Hugues de Riedmatten. Solid State Spin-Wave Quantum Memory for Time-Bin Qubits. *Physical Review Letters*, 114(23):230501, jun 2015.

[20] Harishankar Jayakumar, Ana Predojević, Thomas Kauten, Tobias Huber, Glenn S. Solomon, and Gregor Weihs. Time-bin entangled photons from a quantum dot. *Nature Communications*, 5(May), jun 2014.

[21] Pau Farrera, Georg Heinze, and Hugues de Riedmatten. Entanglement between a photonic time-bin qubit and a collective atomic spin excitation. *Physical Review Letters*, 120(10):100501, 2018.

[22] A. Einstein, B. Podolsky, and N. Rosen. Can Quantum-Mechanical Description of Physical Reality Be Considered Complete? *Physical Review*, 47(10):777–780, may 1935.

[23] J. Bell. On the Einstein-Podolsky-Rosen paradox. *Physics*, I:195, 1964.

[24] David Bohm. A suggested interpretation of the quantum theory in terms of "hidden" variables. I. *Physical Review*, 85(2):166–179, 1952.

[25] Stuart J. Freedman and John F. Clauser. Experimental Test of Local Hidden-Variable Theories. *Physical Review Letters*, 28(14):938–941, apr 1972.

[26] Alain Aspect, Philippe Grangier, and Gérard Roger. Experimental realization of Einstein-Podolsky-Rosen-Bohm Gedankenexperiment: A new violation of Bell's inequalities. *Physical Review Letters*, 49(2):91–94, 1982.

[27] W. Tittel, J. Brendel, H. Zbinden, and N. Gisin. Violation of bell inequalities by photons more than 10 km apart. *Physical Review Letters*, 81(17):3563–3566, 1998.

[28] M. A. Rowe, D. Kielpinski, V. Meyer, C. A. Sackett, W. M. Itano, C. Monroe, and D. J. Wineland. Experimental violation of a Bell's inequality with efficient detection. *Nature*, 409(6822):791–794, 2001.

[29] D. L. Moehring, P. Maunz, S. Olmschenk, K. C. Younge, D. N. Matsukevich, L.-M. Duan, and C. Monroe. Entanglement of single-atom quantum bits at a distance. *Nature*, 449(7158):68–71, 2007.

[30] Stephan Ritter, Christian Nölleke, Carolin Hahn, Andreas Reiserer, Andreas Neuzner, Manuel Uphoff, Martin Mücke, Eden Figueroa, Joerg Bochmann, and Gerhard Rempe. An elementary quantum network of single atoms in optical cavities. *Nature*, 484(7393):195–200, apr 2012.

[31] B. B. Blinov, D. L. Moehring, L.-M. Duan, and C. Monroe. Observation of entanglement between a single trapped atom and a single photon. *Nature*, 428(6979):153–157, mar 2004.

[32] D. N. Matsukevich, T. Chanelière, M. Bhattacharya, S. Y. Lan, S. D. Jenkins, T. A.B. Kennedy, and A. Kuzmich. Entanglement of a photon and a collective atomic excitation. *Physical Review Letters*, 95(4):22–25, 2005.

[33] E. Togan, Y. Chu, A. S. Trifonov, L. Jiang, J. Maze, L. Childress, M. V. G. Dutt, A. S. Sørensen, P. R. Hemmer, A. S. Zibrov, and M. D. Lukin. Quantum entanglement between an optical photon and a solid-state spin qubit. *Nature*, 466(7307):730–734, aug 2010.

[34] Christoph Clausen, Imam Usmani, Félix Bussières, Nicolas San-
gouard, Mikael Afzelius, Hugues de Riedmatten, and Nicolas Gisin.
Quantum storage of photonic entanglement in a crystal. *Nature*,
469(7331):508–11, 2011.

[35] B. Hensen, H. Bernien, A. E. Dréau, A. Reiserer, N. Kalb, M. S.
Blok, J. Ruitenberg, R. F. L. Vermeulen, R. N. Schouten, C. Abellán,
W. Amaya, V. Pruneri, M. W. Mitchell, M. Markham, D. J.
Twitchen, D. Elkouss, S. Wehner, T. H. Taminiau, and R. Hanson.
Loophole-free Bell inequality violation using electron spins separated
by 1.3 kilometres. *Nature*, 526(7575):682–686, oct 2015.

[36] Marissa Giustina, Marijn A.M. Versteegh, Sören Wengerowsky,
Johannes Handsteiner, Armin Hochrainer, Kevin Phelan, Fabian
Steinlechner, Johannes Kofler, Jan Åke Larsson, Carlos Abellán,
Waldimar Amaya, Valerio Pruneri, Morgan W. Mitchell, Jörn Beyer,
Thomas Gerrits, Adriana E. Lita, Lynden K. Shalm, Sae Woo Nam,
Thomas Scheidl, Rupert Ursin, Bernhard Wittmann, and Anton
Zeilinger. Significant-Loophole-Free Test of Bell's Theorem with En-
tangled Photons. *Physical Review Letters*, 115(25):1–7, 2015.

[37] Lynden K. Shalm, Evan Meyer-Scott, Bradley G. Christensen, Pe-
ter Bierhorst, Michael A. Wayne, Martin J. Stevens, Thomas Ger-
rits, Scott Glancy, Deny R. Hamel, Michael S. Allman, Kevin J.
Coakley, Shellee D. Dyer, Carson Hodge, Adriana E. Lita, Varun B.
Verma, Camilla Lambrocco, Edward Tortorici, Alan L. Migdall, Yan-
bao Zhang, Daniel R. Kumor, William H. Farr, Francesco Mar-
sili, Matthew D. Shaw, Jeffrey A. Stern, Carlos Abellán, Waldimar
Amaya, Valerio Pruneri, Thomas Jennewein, Morgan W. Mitchell,
Paul G. Kwiat, Joshua C. Bienfang, Richard P. Mirin, Emanuel
Knill, and Sae Woo Nam. Strong Loophole-Free Test of Local Real-
ism. *Physical Review Letters*, 115(25):1–10, 2015.

[38] Wenjamin Rosenfeld, Daniel Burchardt, Robert Garthoff, Kai Redeker, Norbert Ortegel, Markus Rau, and Harald Weinfurter. Event-Ready Bell Test Using Entangled Atoms Simultaneously Closing Detection and Locality Loopholes. *Physical Review Letters*, 119(1):1–6, 2017.

[39] Nicolas Gisin, Grégoire Ribordy, Wolfgang Tittel, and Hugo Zbinden. Quantum cryptography. *Reviews of Modern Physics*, 74(1):145–195, 2002.

[40] Charles H. Bennett, Gilles Brassard, Claude Crépeau, Richard Jozsa, Asher Peres, and William K. Wootters. Teleporting an unknown quantum state via dual classical and Einstein-Podolsky-Rosen channels. *Physical Review Letters*, 70(13):1895–1899, mar 1993.

[41] Artur K. Ekert. Quantum cryptography based on Bell's theorem. *Physical Review Letters*, 67(6):661–663, aug 1991.

[42] Juan Yin, Yuan Cao, Yu-Huai Li, Sheng-Kai Liao, Liang Zhang, Ji-Gang Ren, Wen-Qi Cai, Wei-Yue Liu, Bo Li, Hui Dai, Guang-Bing Li, Qi-Ming Lu, Yun-Hong Gong, Yu Xu, Shuang-Lin Li, Feng-Zhi Li, Ya-Yun Yin, Zi-Qing Jiang, Ming Li, Jian-Jun Jia, Ge Ren, Dong He, Yi-Lin Zhou, Xiao-Xiang Zhang, Na Wang, Xiang Chang, Zhen-Cai Zhu, Nai-Le Liu, Yu-Ao Chen, Chao-Yang Lu, Rong Shu, Cheng-Zhi Peng, Jian-Yu Wang, and Jian-Wei Pan. Satellite-based entanglement distribution over 1200 kilometers. *Science*, 356(6343):1140–1144, jun 2017.

[43] Hiroki Takesue, Shellee D. Dyer, Martin J. Stevens, Varun Verma, Richard P. Mirin, and Sae Woo Nam. Quantum teleportation over 100 km of fiber using highly efficient superconducting nanowire single-photon detectors. *Optica*, 2(10):832, 2015.

[44] Takahiro Inagaki, Nobuyuki Matsuda, Osamu Tadanaga, Masaki Asobe, and Hiroki Takesue. Entanglement distribution over 300 km of fiber. *Optics Express*, 21(20):23241, 2013.

[45] W. K. Wootters and W. H. Zurek. A single quantum cannot be cloned. *Nature*, 299(5886):802–803, oct 1982.

[46] H.-J. Briegel, W. Dür, J. I. Cirac, and P. Zoller. Quantum Repeaters: The Role of Imperfect Local Operations in Quantum Communication. *Physical Review Letters*, 81(26):5932–5935, 1998.

[47] M. Zukowski, A. Zeilinger, M. A. Horne, and A. K. Ekert. "Event-ready-detectors" Bell experiment via entanglement swapping. *Physical Review Letters*, 71(26):4287–4290, 1993.

[48] Nicolas Sangouard, Christoph Simon, Hugues De Riedmatten, and Nicolas Gisin. Quantum repeaters based on atomic ensembles and linear optics. *Reviews of Modern Physics*, 83(1):33–80, 2011.

[49] L M Duan, M D Lukin, J I Cirac, and P Zoller. Long-distance quantum communication with atomic ensembles and linear optics. *Nature*, 414(6862):413–418, 2001.

[50] Christoph Simon, Hugues De Riedmatten, Mikael Afzelius, Nicolas Sangouard, Hugo Zbinden, and Nicolas Gisin. Quantum repeaters with photon pair sources and multimode memories. *Physical Review Letters*, 98(19):1–4, 2007.

[51] Nicolas Sangouard, Christoph Simon, Jiří Minář, Hugo Zbinden, Hugues de Riedmatten, and Nicolas Gisin. Long-distance entanglement distribution with single-photon sources. *Physical Review A*, 76(5):050301, nov 2007.

[52] W. J. Munro, A. M. Stephens, S. J. Devitt, K. A. Harrison, and Kae Nemoto. Quantum communication without the necessity of quantum memories. *Nature Photonics*, 6(11):777–781, 2012.

[53] Sreraman Muralidharan, Jungsang Kim, Norbert Lütkenhaus, Mikhail D. Lukin, and Liang Jiang. Ultrafast and fault-tolerant quantum communication across long distances. *Physical Review Letters*, 112(25):1–6, 2014.

[54] D. N. Matsukevich, T. Chanelière, S. D. Jenkins, S.-Y. Lan, T. A B Kennedy, and A. Kuzmich. Deterministic Single Photons via Conditional Quantum Evolution. *Physical Review Letters*, 97(1):013601, jul 2006.

[55] Shuai Chen, Yu-Ao Chen, Thorsten Strassel, Zhen-Sheng Yuan, Bo Zhao, Jörg Schmiedmayer, and Jian-Wei Pan. Deterministic and Storable Single-Photon Source Based on a Quantum Memory. *Physical Review Letters*, 97(17):173004, oct 2006.

[56] Pieter Kok, W. J. Munro, Kae Nemoto, T. C. Ralph, Jonathan P. Dowling, and G. J. Milburn. Linear optical quantum computing with photonic qubits. *Reviews of Modern Physics*, 79(1):135–174, 2007.

[57] A. Imamoglu. High Efficiency Photon Counting Using Stored Light. *Physical Review Letters*, 89(16):163602, sep 2002.

[58] Mikael Afzelius, Nicolas Gisin, and Hugues de Riedmatten. Quantum memory for photons. *Physics Today*, 68(12):42–47, 2015.

[59] Y.-W. Cho, G. T. Campbell, J. L. Everett, J. Bernu, D. B. Higginbottom, M. T. Cao, J. Geng, N. P. Robins, P. K. Lam, and B. C. Buchler. Highly efficient optical quantum memory with long coherence time in cold atoms. *Optica*, 3(1):100, 2016.

[60] Daniel F V James, Paul G Kwiat, William J Munro, and Andrew G White. Measurement of qubits. *Physical Review A*, 64(5):052312, oct 2001.

[61] S. Massar and S. Popescu. Optimal Extraction of Information from Finite Quantum Ensembles. *Physical Review Letters*, 74(8):1259–1263, feb 1995.

[62] Georg Heinze, Christian Hubrich, and Thomas Halfmann. Stopped Light and Image Storage by Electromagnetically Induced Transparency up to the Regime of One Minute. *Physical Review Letters*, 111(3):033601, jul 2013.

[63] Sheng Jun Yang, Xu Jie Wang, Xiao Hui Bao, and Jian Wei Pan. An efficient quantum light-matter interface with sub-second lifetime. *Nature Photonics*, 10(6):381–384, 2016.

[64] Erhan Saglamyurek, Jeongwan Jin, Varun B Verma, Matthew D Shaw, Francesco Marsili, Sae Woo Nam, Daniel Oblak, and Wolfgang Tittel. Quantum storage of entangled telecom-wavelength photons in an erbium-doped optical fibre. *Nature Photonics*, 9(2):83–87, feb 2015.

[65] Félix Bussières, Christoph Clausen, Alexey Tiranov, Boris Korzh, Varun B. Verma, Sae Woo Nam, Francesco Marsili, Alban Ferrier, Philippe Goldner, Harald Herrmann, Christine Silberhorn, Wolfgang Sohler, Mikael Afzelius, and Nicolas Gisin. Quantum teleportation from a telecom-wavelength photon to a solid-state quantum memory. *Nature Photonics*, 8(10):775–778, oct 2014.

[66] Daniel Rieländer, Kutlu Kutluer, Patrick M. Ledingham, Mustafa Gündoğan, Julia Fekete, Margherita Mazzera, and Hugues de Riedmatten. Quantum storage of heralded single photons in a praseodymium-doped crystal. *Physical Review Letters*, 112(4):1–5, 2014.

[67] P. Kumar. Quantum frequency conversion. *Optics Letters*, 15(24):1476, 1990.

[68] Félix Bussières, Nicolas Sangouard, Mikael Afzelius, Hugues de Riedmatten, Christoph Simon, and Wolfgang Tittel. Prospective applications of optical quantum memories. *Journal of Modern Optics*, 60(18):1519–1537, oct 2013.

[69] Khabat Heshami, Duncan G. England, Peter C. Humphreys, Philip J. Bustard, Victor M. Acosta, Joshua Nunn, and Benjamin J. Sussman. Quantum memories: emerging applications and recent advances. *Journal of Modern Optics*, 63(20):2005–2028, 2016.

[70] Mikael Afzelius, Christoph Simon, Hugues De Riedmatten, and Nicolas Gisin. Multimode quantum memory based on atomic frequency combs. *Physical Review A - Atomic, Molecular, and Optical Physics*, 79(5):1–9, 2009.

[71] Mikael Afzelius, Imam Usmani, Atia Amari, Björn Lauritzen, Andreas Walther, Christoph Simon, Nicolas Sangouard, Jiří Minář, Hugues de Riedmatten, Nicolas Gisin, and Stefan Kröll. Demonstration of Atomic Frequency Comb Memory for Light with Spin-Wave Storage. *Physical Review Letters*, 104(4):040503, jan 2010.

[72] M Gündoğan, M. Mazzera, P. M. Ledingham, M. Cristiani, and H de Riedmatten. Coherent storage of temporally multimode light using a spin-wave atomic frequency comb memory. *New Journal of Physics*, 15(4):045012, apr 2013.

[73] Pau Farrera, Georg Heinze, Boris Albrecht, Melvyn Ho, Matías Chávez, Colin Teo, Nicolas Sangouard, and Hugues de Riedmatten. Generation of single photons with highly tunable wave shape from a cold atomic ensemble. *Nature Communications*, 7(1):13556, nov 2016.

[74] A. Kuzmich, W. P. Bowen, A. D. Boozer, A. Boca, C. W. Chou, L. M. Duan, and H. J. Kimble. Generation of nonclassical photon pairs for scalable quantum communication with atomic ensembles. *Nature*, 423(6941):731–734, 2003.

[75] C. H. van der Wal. Atomic Memory for Correlated Photon States. *Science*, 301(5630):196–200, jul 2003.

[76] C W Chou, H de Riedmatten, D Felinto, S V Polyakov, S J van Enk, and H J Kimble. Measurement-induced entanglement for excitation stored in remote atomic ensembles-Supplementary Infomation. *Nature*, 438(7069):828–32, 2005.

[77] C.-W. Chou, Julien Laurat, Hui Deng, Kyung Soo Choi, H. de Riedmatten, Daniel Felinto, and H Jeff Kimble. Functional Quantum

Nodes for Entanglement Distribution over Scalable Quantum Networks. *Science*, 316(5829):1316–1320, jun 2007.

[78] Zhen-Sheng Yuan, Yu-Ao Chen, Bo Zhao, Shuai Chen, Jörg Schmiedmayer, and Jian-Wei Pan. Experimental demonstration of a BDCZ quantum repeater node. *Nature*, 454(7208):1098–101, 2008.

[79] K. S. Choi, A. Goban, S. B. Papp, S. J. Van Enk, and H. J. Kimble. Entanglement of spin waves among four quantum memories. *Nature*, 468(7322):412–418, 2010.

[80] T. Chanelière, D. N. Matsukevich, S. D. Jenkins, S.-Y. Lan, T. A. B. Kennedy, and A. Kuzmich. Storage and retrieval of single photons transmitted between remote quantum memories. *Nature*, 438(7069):833–836, 2005.

[81] M. D. Eisaman, A. André, F. Massou, M. Fleischhauer, A. S. Zibrov, and M. D. Lukin. Electromagnetically induced transparency with tunable single-photon pulses. *Nature*, 438(7069):837–841, 2005.

[82] Imam Usmani, Christoph Clausen, Félix Bussières, Nicolas Sangouard, Mikael Afzelius, and Nicolas Gisin. Heralded quantum entanglement between two crystals. *Nature Photonics*, 6(4):234–237, 2012.

[83] Wolfgang Pfaff, B. J. Hensen, Hannes Bernien, Suzanne B. van Dam, Machiel S. Blok, Tim H. Taminiau, Marijn J. Tiggelman, Raymond N. Schouten, Matthew Markham, Daniel J. Twitchen, and Ronald Hanson. Unconditional quantum teleportation between distant solid-state quantum bits. *Science*, 345(6196):532–535, aug 2014.

[84] Aymeric Delteil, Zhe Sun, Stefan Fält, and Atac Imamoglu. Realization of a Cascaded Quantum System: Heralded Absorption of a Single Photon Qubit by a Single-Electron Charged Quantum Dot. *Physical Review Letters*, 118(17):1–5, 2017.

[85] T. E. Northup and R. Blatt. Quantum information transfer using photons. *Nature Photonics*, 8(5):356–363, 2014.

[86] Lilian Childress and Ronald Hanson. Diamond NV centers for quantum computing and quantum networks. *MRS Bulletin*, 38(2):134–138, 2013.

[87] Brahim Lounis and Michel Orrit. Single-photon sources. *Reports on Progress in Physics*, 68(5):1129–1179, may 2005.

[88] R. Hanson, L. P. Kouwenhoven, J. R. Petta, S. Tarucha, and L. M.K. Vandersypen. Spins in few-electron quantum dots. *Reviews of Modern Physics*, 79(4):1217–1265, 2007.

[89] D. Paredes-Barato and C. S. Adams. All-optical quantum information processing using rydberg gates. *Physical Review Letters*, 112(4):1–5, 2014.

[90] R. W. Boyd. Nonlinear Optics. *Academic Press, Elsevier*, 3rd editio, 2008.

[91] P. A. Franken, A. E. Hill, C. W. Peters, and G. Weinreich. Generation of Optical Harmonics. *Physical Review Letters*, 7(4):118–119, aug 1961.

[92] Jianming Huang and Prem Kumar. Observation of quantum frequency conversion. *Physical Review Letters*, 68(14):2153–2156, 1992.

[93] A. G. Radnaev, Y. O. Dudin, R. Zhao, H. H. Jen, S. D. Jenkins, A. Kuzmich, and T. a. B. Kennedy. A quantum memory with telecom-wavelength conversion. *Nature Physics*, 6(11):894–899, 2010.

[94] Philip J. Bustard, Duncan G. England, Khabat Heshami, Connor Kupchak, and Benjamin J. Sussman. Quantum frequency conversion with ultra-broadband tuning in a Raman memory. *Physical Review A*, 95(5):053816, may 2017.

[95] M.M. Fejer, G.A. Magel, D.H. Jundt, and R.L. Byer. Quasi-phase-matched second harmonic generation: tuning and tolerances. *IEEE Journal of Quantum Electronics*, 28(11):2631–2654, 1992.

[96] Carsten Langrock, Eleni Diamanti, Rostislav V Roussev, Yoshihisa Yamamoto, M M Fejer, and Hiroki Takesue. Highly efficient single-photon detection at communication wavelengths by use of upconversion in reverse-proton-exchanged periodically poled LiNbO3 waveguides. *Optics Letters*, 30(13):1725, jul 2005.

[97] S. Tanzilli, W. Tittel, M. Halder, O. Alibart, P. Baldi, N. Gisin, and H. Zbinden. A photonic quantum information interface. *Nature*, 437(September):116, 2005.

[98] J. S. Pelc, L. Ma, C. R. Phillips, Q. Zhang, C. Langrock, O. Slattery, X. Tang, and M. M. Fejer. Long-wavelength-pumped upconversion single-photon detector at 1550 nm: performance and noise analysis. *Optics Express*, 19(22):21445, 2011.

[99] Marius A. Albota and Franco N. C. Wong. Efficient single-photon counting at 155 um by means of frequency upconversion. *Optics Letters*, 29(13):1449, 2004.

[100] Aiko Samblowski, Christina E. Vollmer, Christoph Baune, Jaromír Fiurášek, and Roman Schnabel. Weak-signal conversion from 1550 to 532 nm with 84% efficiency. *Optics Letters*, 39(10):2979–2981, 2014.

[101] Qing Li, Marcelo Davanço, and Kartik Srinivasan. Efficient and low-noise single-photon-level frequency conversion interfaces using silicon nanophotonics. *Nature Photonics*, 10(6):406–414, apr 2016.

[102] Xiang Guo, Chang-Ling Zou, Hojoong Jung, and Hong X. Tang. On-Chip Strong Coupling and Efficient Frequency Conversion between Telecom and Visible Optical Modes. *Physical Review Letters*, 117(12):123902, 2016.

[103] H. J. McGuinness, M. G. Raymer, C. J. McKinstrie, and S. Radic. Quantum frequency translation of single-photon states in a photonic crystal fiber. *Physical Review Letters*, 105(9):1–4, 2010.

[104] Chaitali Joshi, Alessandro Farsi, Stéphane Clemmen, Sven Ramelow, and Alexander L. Gaeta. Frequency multiplexing for quasi-deterministic heralded single-photon sources. *Nature Communications*, 9(1):1–8, 2018.

[105] Christina E. Vollmer, Christoph Baune, Aiko Samblowski, Tobias Eberle, Vitus Händchen, Jaromír Fiurášek, and Roman Schnabel. Quantum up-conversion of squeezed vacuum states from 1550 to 532 nm. *Physical Review Letters*, 112(7):2–6, 2014.

[106] Dehuan Kong, Zongyang Li, Shaofeng Wang, Xuyang Wang, and Yongmin Li. Quantum frequency down-conversion of bright amplitude-squeezed states. *Optics Express*, 22(20):24192, 2014.

[107] Jonathan Lavoie, John M. Donohue, Logan G. Wright, Alessandro Fedrizzi, and Kevin J. Resch. Spectral compression of single photons. *Nature Photonics*, 7(5):363–366, may 2013.

[108] Markus Allgaier, Vahid Ansari, Linda Sansoni, Viktor Quiring, Raimund Ricken, Georg Harder, Benjamin Brecht, and Christine Silberhorn. Highly efficient frequency conversion with bandwidth compression of quantum light. *Nature Communications*, 8:1–6, 2016.

[109] Hiroki Takesue. Single-photon frequency down-conversion experiment. *Physical Review A*, 82(1):013833, jul 2010.

[110] Noé Curtz, Rob Thew, Christoph Simon, Nicolas Gisin, and Hugo Zbinden. Coherent frequency-down-conversion interface for quantum repeaters. *Optics Express*, 18(21):22099, oct 2010.

[111] M. T. Rakher, L. Ma, O. Slattery, X. Tang, and K. Srinivasan. Quantum transduction of telecommunications-band single photons from a

quantum dot by frequency upconversion. *Nature Photonics*, 4(October):786, 2010.

[112] Sebastian Zaske, Andreas Lenhard, Christian A. Keßler, Jan Kettler, Christian Hepp, Carsten Arend, Roland Albrecht, Wolfgang Michael Schulz, Michael Jetter, Peter Michler, and Christoph Becher. Visible-to-telecom quantum frequency conversion of light from a single quantum emitter. *Physical Review Letters*, 109(14):1–5, 2012.

[113] Boris Albrecht, Pau Farrera, Xavier Fernandez-Gonzalvo, Matteo Cristiani, and Hugues de Riedmatten. A Waveguide Frequency Converter Connecting Rubidium Based Quantum Memories to the Telecom C-Band. *Nature Communications*, 5:1–6, 2014.

[114] Rikizo Ikuta, Toshiki Kobayashi, Kenichiro Matsuki, Shigehito Miki, Taro Yamashita, Hirotaka Terai, Takashi Yamamoto, Masato Koashi, Tetsuya Mukai, and Nobuyuki Imoto. Heralded single excitation of atomic ensemble via solid-state-based telecom photon detection. *Optica*, 3(11):1279, nov 2016.

[115] Pau Farrera, Nicolas Maring, Boris Albrecht, Georg Heinze, and Hugues de Riedmatten. Nonclassical correlations between a C-band telecom photon and a stored spin-wave. *Optica*, 3(9):1019, sep 2016.

[116] Rikizo Ikuta, Toshiki Kobayashi, Tetsuo Kawakami, Shigehito Miki, Masahiro Yabuno, Taro Yamashita, Hirotaka Terai, Masato Koashi, Tetsuya Mukai, Takashi Yamamoto, and Nobuyuki Imoto. Polarization insensitive frequency conversion for an atom-photon entanglement distribution via a telecom network. *arXiv 1710.09150*, oct 2017.

[117] Nicolas Maring, Kutlu Kutluer, Joachim Cohen, Matteo Cristiani, Margherita Mazzera, Patrick M. Ledingham, and Hugues de Riedmatten. Storage of up-converted telecom photons in a doped crystal. *New Journal of Physics*, 16, 2014.

[118] Matthias Bock, Pascal Eich, Stephan Kucera, Matthias Kreis, Andreas Lenhard, Christoph Becher, and Jürgen Eschner. High-fidelity entanglement between a trapped ion and a telecom photon via quantum frequency conversion. *arXiv 1710.04866*, oct 2017.

[119] V. Krutyanskiy, M. Meraner, J. Schupp, and B. P. Lanyon. Polarisation-preserving photon frequency conversion from a trapped-ion-compatible wavelength to the telecom C-band. *Applied Physics B*, 123(9):228, sep 2017.

[120] James D. Siverns, John Hannegan, and Qudsia Quraishi. Neutral atom wavelength compatible 780 nm single photons from a trapped ion via quantum frequency conversion. *arXiv 1801.01193*, pages 1–5, 2018.

[121] Thomas A. Wright, Robert J. A. Francis-Jones, Corin B. E. Gawith, Jonas N. Becker, Patrick M. Ledingham, Peter G. R. Smith, Joshua Nunn, Peter J. Mosley, Benjamin Brecht, and Ian A. Walmsley. A two-way quantum interface for linking Sr+ transition at 422nm to the telecommunications C-band. *arXiv1802.07947*, 1(1):1–5, feb 2018.

[122] Anaïs Dréau, Anna Tcheborateva, Aboubakr El Mahdaoui, Cristian Bonato, and Ronald Hanson. Quantum frequency conversion to telecom of single photons from a nitrogen-vacancy center in diamond. *arXiv 1801.03304*, pages 1–8, jan 2018.

[123] Serkan Ates, Imad Agha, Angelo Gulinatti, Ivan Rech, Matthew T. Rakher, Antonio Badolato, and Kartik Srinivasan. Two-photon interference using background-free quantum frequency conversion of single photons emitted by an InAs quantum dot. *Physical Review Letters*, 109(14):1–5, 2012.

[124] Andreas Lenhard, José Brito, Matthias Bock, Christoph Becher, and Jürgen Eschner. Coherence and entanglement preservation of frequency-converted heralded single photons. *Optics Express*, 25(10):11187, may 2017.

[125] Xavier Fernandez-Gonzalvo, Giacomo Corrielli, Boris Albrecht, Marcel.li Grimau, Matteo Cristiani, and Hugues de Riedmatten. Quantum frequency conversion of quantum memory compatible photons to telecommunication wavelengths. *Optics Express*, 21(17):19473, 2013.

[126] J S Pelc, C Langrock, Q Zhang, and M M Fejer. Influence of domain disorder on parametric noise in quasi-phase-matched quantum frequency converters. *Optics letters*, 35(16):2804–2806, 2010.

[127] M.G. Raymer, S.J. van Enk, C.J. McKinstrie, and H.J. McGuinness. Interference of two photons of different color. *Optics Communications*, 283(5):747–752, mar 2010.

[128] Stéphane Clemmen, Alessandro Farsi, Sven Ramelow, and Alexander L. Gaeta. Ramsey Interference with Single Photons. *Physical Review Letters*, 117(22):1–6, 2016.

[129] Toshiki Kobayashi, Rikizo Ikuta, Shuto Yasui, Shigehito Miki, Taro Yamashita, Hirotaka Terai, Takashi Yamamoto, Masato Koashi, and Nobuyuki Imoto. Frequency-domain Hong–Ou–Mandel interference. *Nature Photonics*, 10(7):441–444, 2016.

[130] Jason Scott Pelc. *Frequency Conversion of Single Photons: Physics, Devices, and Applications*. PhD thesis, Standford University, 2012.

[131] M Bass, P a Franken, J. F. Ward, and G Weinreich. Optical Rectification. *Physical Review Letters*, 9(11):446–448, dec 1962.

[132] Nicolas Maring, Dario Lago-Rivera, Andreas Lenhard, Georg Heinze, and Hugues de Riedmatten. Quantum frequency conversion of memory-compatible single photons from 606 nm to the telecom C-band. *Optica*, 5(5):507, may 2018.

[133] G D Miller, R G Batchko, W M Tulloch, D R Weise, M M Fejer, and R L Byer. 42%-efficient single-pass cw second-harmonic generation

in periodically poled lithium niobate. *Optics Letters*, 22(24):1834, dec 1997.

[134] Andreas Lenhard. *Quantum Photonic Interfaces between Atomic and Telecommunication Wavelengths*. PhD thesis, Universitat des Saarlandes, 2015.

[135] Rostislav V. Roussev, Carsten Langrock, Jonathan R. Kurz, and M. M. Fejer. Periodically poled lithium niobate waveguide sum-frequency generator for efficient single-photon detection at communication wavelengths. *Optics Letters*, 29(13):1518, 2004.

[136] Helge Rütz, Kai Hong Luo, Hubertus Suche, and Christine Silberhorn. Quantum Frequency Conversion between Infrared and Ultraviolet. *Physical Review Applied*, 7(2):1–7, 2017.

[137] Sebastian Zaske, Andreas Lenhard, and Christoph Becher. Efficient frequency downconversion at the single photon level from the red spectral range to the telecommunications C-band. *Optics express*, 19(13):12825–36, jun 2011.

[138] Rikizo Ikuta, Toshiki Kobayashi, Shuto Yasui, Shigehito Miki, Taro Yamashita, Hirotaka Terai, Mikio Fujiwara, Takashi Yamamoto, Masato Koashi, Masahide Sasaki, Zhen Wang, and Nobuyuki Imoto. Frequency down-conversion of 637 nm light to the telecommunication band for non-classical light emitted from NV centers in diamond. *Optics Express*, 22(9):11205, 2014.

[139] Alessandro Seri, Andreas Lenhard, Daniel Rieländer, Mustafa Gündoğan, Patrick M. Ledingham, Margherita Mazzera, and Hugues de Riedmatten. Quantum Correlations between Single Telecom Photons and a Multimode On-Demand Solid-State Quantum Memory. *Physical Review X*, 7(2):021028, may 2017.

[140] Julia Fekete, Daniel Rieländer, Matteo Cristiani, and Hugues de Riedmatten. Ultranarrow-band photon-pair source compatible

with solid state quantum memories and telecommunication networks. *Physical Review Letters*, 110(22):1–5, 2013.

[141] Daniel Rieländer, Andreas Lenhard, Margherita Mazzera, and Hugues De Riedmatten. Cavity enhanced telecom heralded single photons for spin-wave solid state quantum memories. *New Journal of Physics*, 18(12):123013, dec 2016.

[142] Sylvain Fasel, Olivier Alibart, Sébastien Tanzilli, Pascal Baldi, Alexios Beveratos, Nicolas Gisin, and Hugo Zbinden. High-quality asynchronous heralded single-photon source at telecom wavelength. *New Journal of Physics*, 6:1–11, 2004.

[143] Y. C. Sun. Rare Earth Materiais in Optical Storage and Data Processing Applications. In *Spectroscopic Properties of Rare Earths in Optical Materials*, pages 379–429. Springer-Verlag, Berlin/Heidelberg, 2005.

[144] Mattias Nilsson, Lars Rippe, Stefan Kröll, Robert Klieber, and Dieter Suter. Hole-burning techniques for isolation and study of individual hyperfine transitions in inhomogeneously broadened solids demonstrated in Pr3+:Y2SiO5. *Physical Review B - Condensed Matter and Materials Physics*, 70(21):1–11, 2004.

[145] O. Guillot-Noël, Ph Goldner, F. Beaudoux, Y. Le Du, J. Lejay, A. Amari, A. Walther, L. Rippe, and S. Kröll. Hyperfine structure and hyperfine coherent properties of praseodymium in single-crystalline La2 (WO4) 3 by hole-burning and photon-echo techniques. *Physical Review B - Condensed Matter and Materials Physics*, 79(15):1–11, 2009.

[146] Nicolas Maring, Pau Farrera, Kutlu Kutluer, Margherita Mazzera, Georg Heinze, and Hugues de Riedmatten. Photonic quantum state transfer between a cold atomic gas and a crystal. *Nature*, 551(7681):485–488, nov 2017.

[147] P Sekatski, N Sangouard, F Bussières, C Clausen, N Gisin, and H Zbinden. Detector imperfections in photon-pair source characterization. *Journal of Physics B: Atomic, Molecular and Optical Physics*, 45(12):124016, jun 2012.

[148] Y. O. Dudin, A. G. Radnaev, R. Zhao, J. Z. Blumoff, T. A B Kennedy, and A. Kuzmich. Entanglement of light-shift compensated atomic spin waves with telecom light. *Physical Review Letters*, 105(26):1–4, 2010.

[149] Xiao Hui Bao, Andreas Reingruber, Peter Dietrich, Jun Rui, Alexander Dück, Thorsten Strassel, Li Li, Nai Le Liu, Bo Zhao, and Jian Wei Pan. Efficient and long-lived quantum memory with cold atoms inside a ring cavity. *Nature Physics*, 8(7):517–521, 2012.

[150] Sen Yang, Ya Wang, D. D. Bhaktavatsala Rao, Thai Hien Tran, Ali S. Momenzadeh, M. Markham, D. J. Twitchen, Ping Wang, Wen Yang, Rainer Stöhr, Philipp Neumann, Hideo Kosaka, and Jörg Wrachtrup. High-fidelity transfer and storage of photon states in a single nuclear spin. *Nature Photonics*, 10(8):507–511, aug 2016.

[151] Yan Jiang, Jun Rui, Xiao Hui Bao, and Jian Wei Pan. Dynamical zeroing of spin-wave momentum to suppress motional dephasing in an atomic-ensemble quantum memory. *Physical Review A*, 93(6):1–4, 2016.

[152] Ze-Liang Xiang, Sahel Ashhab, J. Q. You, and Franco Nori. Hybrid quantum circuits: Superconducting circuits interacting with other quantum systems. *Reviews of Modern Physics*, 85(2):623–653, apr 2013.

[153] T. R. Tan, J. P. Gaebler, Y. Lin, Y. Wan, R. Bowler, D. Leibfried, and D. J. Wineland. Multi-element logic gates for trapped-ion qubits. *Nature*, 528(7582):380–383, 2015.

[154] C. J. Ballance, V. M. Schäfer, J. P. Home, D. J. Szwer, S. C. Webster, D. T. C. Allcock, N. M. Linke, T. P. Harty, D. P. L. Aude Craik,

D. N. Stacey, A. M. Steane, and D. M. Lucas. Hybrid quantum logic and a test of Bell's inequality using two different atomic isotopes. *Nature*, 528(7582):384–386, 2015.

[155] N. Akopian, L. Wang, A. Rastelli, O. G. Schmidt, and V. Zwiller. Hybrid semiconductor-atomic interface: slowing down single photons from a quantum dot. *Nature Photonics*, 5(4):230–233, 2011.

[156] Petr Siyushev, Guilherme Stein, Jörg Wrachtrup, and Ilja Gerhardt. Molecular photons interfaced with alkali atoms. *Nature*, 509(7498):66–70, 2014.

[157] H. M. Meyer, R. Stockill, M. Steiner, C. Le Gall, C. Matthiesen, E. Clarke, A. Ludwig, J. Reichel, M. Atatüre, and M. Köhl. Direct photonic coupling of a semiconductor quantum dot and a trapped ion. *Physical Review Letters*, 114(12):1–5, 2015.

[158] Jian-Shun Tang, Zong-Quan Zhou, Yi-Tao Wang, Yu-Long Li, Xiao Liu, Yi-Lin Hua, Yang Zou, Shuang Wang, De-Yong He, Geng Chen, Yong-Nan Sun, Ying Yu, Mi-Feng Li, Guo-Wei Zha, Hai-Qiao Ni, Zhi-Chuan Niu, Chuan-Feng Li, and Guang-Can Guo. Storage of multiple single-photon pulses emitted from a quantum dot in a solid-state quantum memory. *Nature Communications*, 6:8652, 2015.

[159] Matthias Lettner, Martin Mücke, Stefan Riedl, Christoph Vo, Carolin Hahn, Simon Baur, Jörg Bochmann, Stephan Ritter, Stephan Dürr, and Gerhard Rempe. Remote Entanglement between a Single Atom and a Bose-Einstein Condensate. *Physical Review Letters*, 106(21):210503, may 2011.

[160] Jiří Minář, Hugues de Riedmatten, Christoph Simon, Hugo Zbinden, and Nicolas Gisin. Phase-noise measurements in long-fiber interferometers for quantum-repeater applications. *Physical Review A*, 77(5):052325, may 2008.

[161] Morgan P. Hedges, Jevon J. Longdell, Yongmin Li, and Matthew J. Sellars. Efficient quantum memory for light. *Nature*, 465(7301):1052–1056, 2010.

[162] N. Sinclair, K. Heshami, C. Deshmukh, D. Oblak, C. Simon, and W. Tittel. Proposal and proof-of-principle demonstration of non-destructive detection of photonic qubits using a Tm:LiNbO3 waveguide. *Nature Communications*, 7:13454, nov 2016.

[163] Kutlu Kutluer. *Quantum Memory Protocols for Photonic Solid-State Devices*. PhD thesis, Universitat Polytecnica de Catalunya, 2015.

[164] Pierre Jobez, Nuala Timoney, Cyril Laplane, Jean Etesse, Alban Ferrier, Philippe Goldner, Nicolas Gisin, and Mikael Afzelius. Towards highly multimode optical quantum memory for quantum repeaters. *Physical Review A*, 93(3):032327, mar 2016.

[165] Cyril Laplane, Pierre Jobez, Jean Etesse, Nicolas Gisin, and Mikael Afzelius. Multimode and Long-Lived Quantum Correlations between Photons and Spins in a Crystal. *Physical Review Letters*, 118(21):1–5, 2017.

[166] Kutlu Kutluer, Margherita Mazzera, and Hugues de Riedmatten. Solid-State Source of Nonclassical Photon Pairs with Embedded Multimode Quantum Memory. *Physical Review Letters*, 118(21):210502, may 2017.

[167] Kate R. Ferguson, Sarah E. Beavan, Jevon J. Longdell, and Matthew J. Sellars. Generation of Light with Multimode Time-Delayed Entanglement Using Storage in a Solid-State Spin-Wave Quantum Memory. *Physical Review Letters*, 117(2):1–5, 2016.